



## COST FUNCTIONS FOR TWO-METRIC QUALITY OF SERVICE ROUTING

Derya YILTAS KAPLAN

Istanbul University, Engineering Faculty, Department of Computer Engineering  
34320, Avcilar, Istanbul-TURKEY  
dyiltas(at)istanbul.edu.tr

---

**Abstract:** Different metrics are used for measuring the goodness of packet routing between the source and destination pairs in a communication network. One approach is to compute the paths from the measured metric values, which are predetermined independently according to the network resources. The combination of some metrics of different natures to get a composite cost function for the routing process is non-trivial. We consider two metrics, namely delay and packet loss rate. The first one takes values from the large numbers and the second from the small. We propose some methods for constructing composite functions of these metrics without any constraints and use them for the shortest path calculations. We give the numerical results of the proposed composite functions versus the Dijkstra's algorithm with the individual metrics. We spot out the best function according to our computer simulation results. Our composite function works for any arbitrary point-to-point networks. To the best of our knowledge, the technique is novel. Our results show an efficient way to balance the effects of the metrics in the context of many-to-many routing.

**Keywords:** Cost function, delay, network communications, packet loss rate, QoS routing.

---

### 1. Introduction

One of the most important terms during the transmission of voice or data among the networks is Quality of Service (QoS). This key subject is the basic factor specifying the QoS levels especially in multimedia applications. There are many factors having an influence on QoS of the network. One of them is the route selection or routing, which includes discovering different paths along a network. The metrics in the routing process have been mostly defined in the literature, according to their effects on the whole QoS of the network. Hanzo II and Tafazolli [1] presented a metric classification related to network, link, and physical layers of the OSI model. Some of their metrics are end-to-end delay, packet loss rate, jitter, link stability, and bit error rate. Yin, et. al. [2] gave a similar metric list for performance measurement of routing protocols.

Several researchers have studied end-to-end connection implementations that maintain the required metrics in a reasonable range. QoS renegotiation, which is the decision of the probable QoS values, must be performed between network and application layers to get the necessary performance level [3]. Application layer requires some specific QoS values from the transportation layer and then available QoS values related to the network situation are decided. In various

studies, this can be done by QoS negotiation. For example Obreja and Borcoci [4] described an approach in which each domain manager is able to establish QoS values without having the traffic information of other domains. Here, the processes of routing and QoS negotiation run independently. During offline computation, paths are chosen on a network where nodes are referred to domain manages. Therefore any scalability problem is prevented. Iqbal, et. al. [5] proposed another QoS scheme which is dependent on the negotiation between network and application layers. Here, network layer gives the information about network congestion to the application layer. Source node's applications adjust sending data rate according to the congestion level of the traffic flows. Routing is concerned in this scheme.

In the literature, Multi-Constrained Path Problem (MCP) provides to find multiple metric-constrained paths along a network. MCP is also considered as an optimality problem [6-7]. Djarallah, et. al. [6] defined the metrics as the vectors of weight parameters. So they performed the metrics as non-composite numbers and computed them discretely. After then they used these metrics to get the optimal paths for the source-destination pairs. They initialized an inter-domain route set on the way of this solution. They obtained several feasible paths which satisfy the predetermined metrics and then eliminated some of them which have larger weights. On the last set, they performed an objective function to select the optimal path.

In another multiple metric method [8], the user requests different QoS values and then each service provider tries to find a suitable domain link based on these requested values. Bertrand, et. al. [9] benefited from some additive metrics and computed the total metric values of the links in a relaxation step. They compared these values with each other with the goal of finding multiple paths and obtaining Virtual Shortest Path Tree which includes the path with the minimum cost.

Masip-Bruin, et. al. [10] benefited from Enhanced QoS Border Gateway Protocol to provide the paths. In this scheme, a metric for a path segment is chosen and then an assembling function is used to combine all segment values as the whole path value. After the computations, a decision step is applied through a Degree of Preference function for getting the best path related to the metric values, and also all available paths are stored. In a different multi-constrained routing solution, Shin, et. al. [11] initialized the process with some subpaths and then performed their extensions to reach the whole paths. In this scheme, the number of subpaths is limited during the computations, but then raised to find the rest of the paths in a probabilistic way. Xue and Ganz [12] actuated the routing process depending on the metrics of bandwidth and delay consecutively. Similarly, Yuan and Liu [13] considered  $k$  different metrics independently. The main drawback of this method is that the authors should store all optimal paths and provide the QoS requirements by using the constraint of each metric.

In the literature, the path weights are commonly computed based on different metrics independently and then a comparison is made between all metrics to get the best path. The challenging problem of combining various metrics to analyze path optimality has been studied within several algorithms as given briefly in [14].

In this paper, we provide an easy computation to find the path of optimal trade-off between two metrics at the same time. These two metrics fall on different number ranges, one is from very small real numbers, and the other from large integers. We give the structures of some composite functions, and use experiments to find the most effective one. Our work differs from the other works in the literature in the way that the metrics are not necessarily in similar natures. For example, Van Mieghem, et. al. [15] implemented their algorithm with all constraints uniformly distributed on  $[0, 1]$ .

The rest of this paper is designed as follows. Section 2 gives some necessary definitions. In Section 3, we define two basic composite functions and construct a new composite function, of which we select the terms carefully. Then, it is followed by experimental results. Finally, we give the conclusion and future work of this study in Section 4. In this paper, we put aside the unpredictable practical network environmental issues such as user request, admission control, and security.

## 2. Definitions and Notation

The network, or graph,  $G=(V,E)$  in question is a connected, and undirected, static point-to-point arbitrary graph, where  $V =\{1,2,\dots,n\}$  is the set of nodes and  $E$  the edge set. Each edge  $e$  has a two-dimensional cost  $(-, -)$ , and the two metrics inside are delay ( $D$ ) and packet loss rate ( $PL$ ). The delay of  $e$  can be considered as the average time for a message to wait in the outgoing buffer (queue) of  $e$  before departure. The packet loss rate of  $e$  is the probability of a message being lost during transmission through  $e$ . We assume two conditions on these two metrics such as general assumptions in the most QoS studies.

1. *The delay and packet loss rate are static for each edge.*
2. *The delay and packet loss rate of an edge are not directly proportional to each other.*

We argue for assumption 1. Obviously, this assumption may not be accurate as the metrics are affected by the interference between messages. However, their dynamic values are difficult to trace in real time, and even sophisticated methods can only give approximation. More importantly, there is no algorithmic difference between using their actual values and using the approximated ones. In practice, the system can use the latest known values and construct the composite function after a certain period of time.

We now argue for assumption 2. For unreliable protocol like UDP, a lost packet will not be transmitted again, and therefore, there will not cause any longer delay. For reliable protocol like TCP, or the Data Link layer protocol, a lost packet will be re-transmitted; however, such re-transmission will not necessarily be placed back to the waiting queue as a new coming packet. Hence, longer delay will be experienced but it may not take the same amount of time as before.

The values of delays are chosen from the positive integer set, and those of packet loss rates from the positive real numbers much smaller than 1. Followed from traditions, the delay of a routing path  $p$  is the sum of all delays over all edges along  $p$ . (Using product or sum depends solely on the nature of the metric because they are mathematically convertible to each other.) The definition of the packet loss rate of  $p$  is similar, because we assume that the product of the packet loss rates of any two edges is negligible. This assumption allows us to simply minimize the sum of packet loss rates in a path. Now, we argue that even without this assumption, we can still translate the packet loss rate into some other quantity and use this additive property again. For every edge with packet loss rate  $PL$ , define the packet transfer rate to be  $1-PL$ , and the packet transfer rate of a path to be the product of all packet transfer rates of the edges along the path. Since each packet transfer rate is at most one, it can be rewritten as a non-positive power of 2 (or  $e=2.716$ ). Higher packet transfer rate can be achieved by pushing up the sum of all the powers along the path. This can be done by lowering the sum of the absolute values of the powers. The argument is complete. In short, for packet loss rate  $PL$  of an edge, we translate it into  $|\log(1-PL)|$ . For the simplicity of discussion, we leave this transformation to

the engineers, and consider the sum of the packet loss rates along a path as a parameter for optimization.

### 3. Constructing Composite Functions

We divide this section into three subsections: Basic composite functions, a new composite function, and practicing the composite functions without constraints.

#### 3.1. Basic Composite Functions

We now study the cost function of a routing path. If either the delay or packet loss rate is considered, we can directly apply Dijkstra's algorithm for finding the shortest path. However, mathematically, it is impossible to achieve optimality for two metrics simultaneously representing the delay and packet loss rate of each edge. Figure 1 is an example, which shows different paths from the source to destination based on different metrics. In other words, we can only find trade-offs between them.

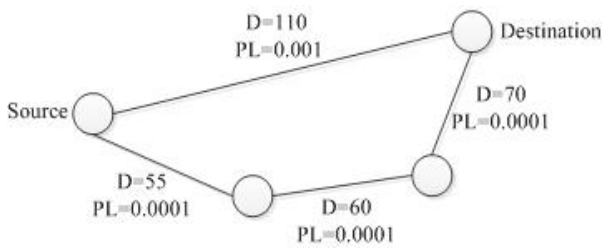


**Figure 1.** The edges with two metrics between the source and destination nodes

A composite function of two metrics, namely  $x$  and  $y$ , can be defined as either an ordered pair  $(x,y)$  or a single value of a function of  $x$  and  $y$ . There are different advantages for each of these approaches. For using  $(x,y)$ , each metric will be considered symmetrically, and the main difficulty of the research work will focus on the relationship between dimensionality and path optimality. Such work is rather algorithmic than practical, and extending the algorithm for more metrics is by no mean trivial. In this paper, we use a single-value composite function, and therefore, the path optimality can be simply done by many existing algorithms, while the research will emphasize on how to construct the function with two metrics of different characteristics. Another advantage of using one single value is the feasibility of allowing more metrics for future research. The goodness of a composite function is measured by the ratio of the resulting cost to the optimal cost, for each metric.

For the construction of a composite function, there are more to consider. First, when one metric is zero (or weighted zero), the format of the composite function must be linear and homogeneous to the cost of a routing path based on the other metric. Second, the weighting of the two metrics can be adjusted. There are two basic formats for the composite function ( $CF$ ):

$$CF = C_D D + C_{PL} PL \quad (1)$$

$$CF = C_T D * PL + C_D D + C_{PL} PL, \quad (2)$$

where  $C_T$ ,  $C_D$ , and  $C_{PL}$  are constants and designed by system designers. The notation  $CF(p)$  is used for the sum of all  $CF$  values of the edges along  $p$ . In using either equation, we need to minimize  $CF(p)$ . From the point of constructing the function, we need to design two constants,  $C_D/C_T$  and  $C_{PL}/C_T$ , in Eqn (2), if  $C_T \neq 0$ ; however, only the fraction  $C_{PL}/C_D$  is needed in Eqn (1), if  $C_D \neq 0$ . Therefore, using Eqn (1) is more convenient. For simplicity, we shall refer  $CF$  in Eqn (1) as  $CF1$  and that in Eqn (2) as  $CF2$ .

A similar function of  $CF1$  was proposed by Jaffe [16] to meet different constraints in MCPP. According to his approximation, the minimization of that function may also give an optimal path that does not satisfy the constraints.  $CF1$  differs in the bound of  $D$ , which is not in the range  $[0, 1]$ .

#### 3.2. A New Composite Function

We propose a new composite function with considering the Assumptions 1 and 2. With the assignment of the initial values to the delay and packet loss rate of each edge on a sample network, we introduce our composite function, which covers both metrics together. The aggregation of the two metrics from distinct ranges is the bottleneck in the literature. To solve this problem, a common range for the metrics is figured out to get a composite function as the edge cost function for the routing process. This common range is obtained by using ranking on the original metrics. However, it is still not a universal technique for data analysis due to its uncertain performance.

Ranking has been used for removing noises on the original data, and has been verified successfully in many cases. However, it can also remove some important features of a parameter. To the extreme, we cannot judge the goodness of a ranking function; however, we believe that, in many cases, we can apply some statistical techniques to construct a better composite function.

Suppose that we are given sets of data for different parameters, and a good basic composite function  $B$  which uses original data. We rank the data and study the relationship between the original values and their ranks. Since the ranking is a strict increasing bijective function of the original data, the inverse function can also be used for describing the relationship. We approximate this inverse function by some simple functions like polynomial and exponential functions. This approximate function is used for substituting the original parameter in function  $B$ . We do this for all parameters, and the resulting function is then rank-based.

Now, the burden falls on experimental work for finding the approximate inverse function.

Based on the above explanation of the ranking process, the new composite function basically covers the rank, which will be symbolized as  $R$ , for each metric value. In this subsection, we focus on delay and packet loss rate. Let  $D_e$  and  $PL_e$  be the values of delay and packet loss rate, and

they have ranks  $R_{D_e}$  and  $R_{PL_e}$ , respectively, for edge  $e$ . In this method we consider same ranks for the same values in each order. For example, if the delay sequence is 5, 10, 15, 15, 47 for five edges, then the delay ranks become 1, 2, 3, 3, 4, respectively. Mathematically, for each metric, our ranking is a bijective function  $Rank(\cdot)$  from the set of values of all edges to an integer set  $\{1, 2, \dots, L\}$ , for some positive  $L$  (where  $L$  is the number of different values in the domain), and  $Rank(D_e) < Rank(D_{e'})$  if and only if  $D_e < D_{e'}$ . After this ranking step, we do not need any other optimization technique for the metric ratings between the edges.

After the computations of the ranks, we construct the composite function of two metrics from distinct ranges as

$$CF_e = Coef * R_{D_e} + Base^{R_{PL_e}} \quad (3)$$

where  $CF_e$  is the numerical value of the composite function for  $e$ . For simplicity, we refer the function in Eqn (3) as CF3. According to the values of the packet loss rates which we use in the domain, each increment is a factor of 10. Ranking can then be considered as a base-10 logarithmic function of the original values. As optimality is measured by the sum of the original values along the routing paths, we use an exponential function of the ranks in the composite function, instead of the ranks themselves. For this reason, the *Base* value in CF3 is selected as 10 according to this relation between the packet loss rate and ranking. Experiments show that with this modification of ranking technique, we can adjust the weighting of delay and packet loss rate efficiently in order to seek for a balance of their performance. Note that *Coef* in CF3 is selected after some practical results, which will be mentioned in Section 3.3.

CF3 gives the cost function of  $e$  to be used in the selection of the optimal path over a network by Dijkstra's algorithm. The cost function of a path  $p$  with  $|E|$  edges can be calculated as

$$CF(p) = \sum_{e=1}^{|E|} CF_e \quad (4)$$

### 3.3. Practicing the Composite Functions

In this subsection, first we get CF1 and CF2 as the cost functions of an edge and then use Dijkstra's algorithm to observe the best paths according to these functions. We refer these methods as Dijkstra(CF1) and Dijkstra(CF2) respectively. After finishing this step, we skip to CF3 practices and select the best *Coef* value to complete CF3 by referring this method as Dijkstra(CF3). Then we extend CF3 to get another function.

In this paper, we computed all experimental results over the network represented in Figure 2. This network is a sample of mesh network and appropriate for the

selections of the paths with the specified hop numbers in the comparisons. It covers 75 nodes and 100 full-duplex edges.

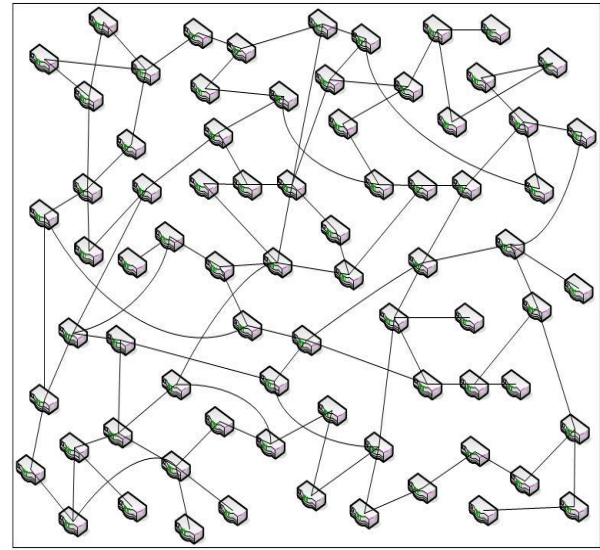


Figure 2. The sample network

Each edge  $e$  in the network was provided with numerical values of delay and packet loss rate. Delay values are between [1, 150] and the packet loss rates should be one of the values 0.000001, 0.00001, 0.0001, and 0.001. We assign the metric values of the whole network as behaving towards the normal distribution.

We selected five source-destination node pairs for each hop number  $h$ , where  $h = 2, 4, 6, 8, 10$ .  $h$  represents the minimum edge number obtained manually along a path, which starts from the predetermined source node and ends in the destination. All functions try to find several paths between two end nodes without considering their edge numbers. We executed the application 400 times for each node pair of each hop number. So we used 400 different metric validations of the edges in the network. We computed the average values of delay and packet loss rate of the 2000 different best paths for each hop number.

For fine-tuning the performance, for convenience, we start with  $C_{PL} / C_D = 1$  in Eqn (1). If the worst case ratio of delay is greater than that of packet loss rate, we decrease  $C_{PL} / C_D$ ; otherwise, increase it. The worst case ratio of a parameter is referred to the maximum (over all values of  $h$ ) experimental performance ratio averaged over all experiments. The same experiment is also done for the terms in Eqn (2). To speed up, binary search can be used. The binary search can stop if the worst case ratios are less than a threshold, say 5%, apart from each other. We finally chose  $C_{PL} / C_D = 185000$  for Dijkstra(CF1),  $C_D / C_T = 1/10$  and  $C_{PL} / C_T = 185000$  for Dijkstra(CF2) to get the computational results in this subsection.

The worst case ratios of delay and packet loss rate for Dijkstra(CF1) and Dijkstra(CF2) obtained for each hop number are stated as in Table 1. The worst case ratios occur around hop number 6 for both of the delay and packet loss

rate values. Both of the functions are in balance according to two metrics.

**Table 1.** Worst case ratios

Hop Number	Delay		Packet Loss Rate	
	CF1	CF2	CF1	CF2
2	1,101004	1,101004	1,628099	1,628099
4	1,103260	1,103289	1,600887	1,600887
<b>6</b>	<b>1,150929</b>	<b>1,151819</b>	<b>1,731111</b>	<b>1,728889</b>
8	1,136208	1,136468	1,520000	1,520000
10	1,145566	1,145517	1,713450	1,713450

We now skip to find the *Coef* value in CF3. Through the use of Eqn (4) as the path cost function in Dijkstra(CF3), the correlated CF3 appears concretely after implementing different *Coef* values and choosing the most effective one, which concludes the paths with the best aggregation of delays and packet loss rates. Figure 3 and Figure 4 show the last delays and packet loss rates provided by using different *Coefs* in CF3 with the constant *Base* value of 10. We practiced several *Coefs* between 100 and 200 in Dijkstra(CF3) and determined that the best values are around 120 and 125 according to the both of the metrics. The metric values measured with the *Coefs* between 120 and 125 are represented in Table 2 for Hop Number=6. We chose this hop number because that the main difference between the *Coefs* can be seen clearly at that point. It can be easily extracted from Table 2 that *Coef*=120 is the best selection for CF3.

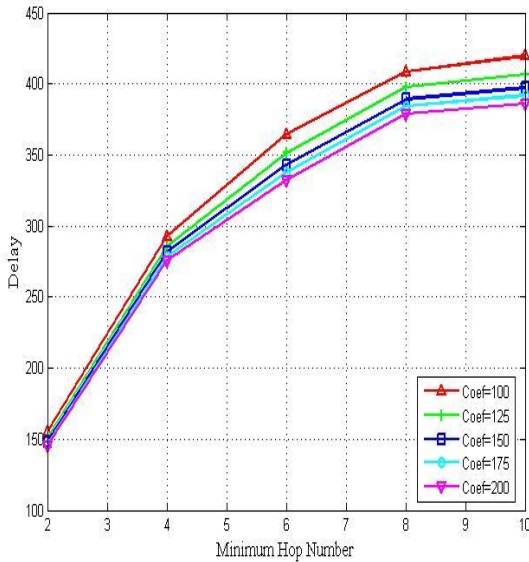


**Figure 3.** Delays for different Coefs in CF3

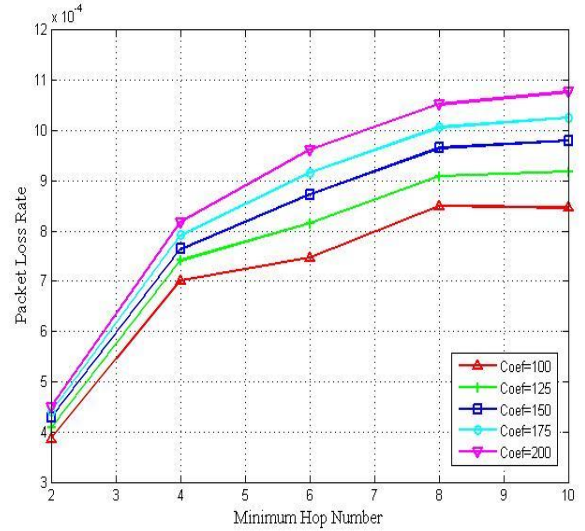


**Figure 4.** Packet loss rates for different Coefs in CF3

**Table 2.** The metric values with *Coef* between [120, 125]

Coef	Delay	Packet Loss Rate
120	353,5145	0,000805
121	353,3715	0,000806
122	353,1195	0,000807
123	352,2650	0,000811
124	352,0160	0,000813
125	351,5465	0,000816

Consequently, we converted CF3 for each *e* with the selected *Coef* and *Base* values into

$$CF3 = 120 * R_{D_e} + 10^{R_{PL_e}} \tag{5}$$

We now change only  $R_{PL_e}$  computation to find another

function. We match the packet loss rate values of the set {0.000001, 0.00001, 0.0001, 0.001} to an integer set {2<sup>0</sup>, 2<sup>1</sup>, 2<sup>2</sup>, 2<sup>3</sup>} sequentially. We used the same *Base* 10 as in Eqn (5) and obtained

$$CF4 = Coef * R_{D_e} + 10^{R_{PL_e}} \tag{6}$$

where CF4 is a new cost function of an edge to be used in Dijkstra's algorithm as Dijkstra(CF4). We practiced several *Coefs* between 10<sup>4</sup> and 10<sup>8</sup> in Dijkstra(CF4) and determined that the best value is 10<sup>6</sup> according to the both of the metrics. After this result, we converted Eqn (6) into

$$CF4 = 10^6 * R_{D_e} + 10^{R_{PL_e}} \tag{7}$$

For any CF<sub>x</sub> (x=1,2,3 or 4), we use the pseudocode of Dijkstra(CF<sub>x</sub>) as illustrated in Figure 5.



```

MAIN FUNCTION Dijkstra(CFx)
for hop_number=2:2:10
    for SourceDest_pair=1:5
        for r=1:runs %runs=400
            Get both metric validations of all edges from the source file.
            Compute  $R_{D_e}$  and  $R_{PL_e}$  for each edge.
            Compute  $CF_e$  value of each edge.
            Apply Dijkstra's Algorithm based on the normalized  $CF_e$  values to find the shortest path
            over the network.
        end
    end
end
Calculate average delay values of the shortest paths with the current hop_number.
Calculate average packet loss rates of the shortest paths with the current hop_number.
end
    
```

Figure 5. Pseudocode of Dijkstra(CFx)

A comparison between Dijkstra(CF1), Dijkstra(CF2), Dijkstra(CF3), and Dijkstra(CF4) is given in Figure 6 and Figure 7 against the related values of each single metric version as Dijkstra(D) or Dijkstra(PL). Dijkstra(CF1) and Dijkstra(CF2) overlap in Figure 6 and Figure 7. The results of Dijkstra(CF1), Dijkstra(CF2), and Dijkstra(CF3) are close to each other. Dijkstra(CF4) improves the PL results. This is very important for any network, especially for multimedia networks.

The worst case ratios of the delay values for CF3 and CF4 are both 1.1x. On the other hand, the worst case ratios of the packet loss rates are 1.7x and 1.6x respectively. It tells that CF4 is better than CF1, CF2, and CF3 according to the balance of two independent parameters.

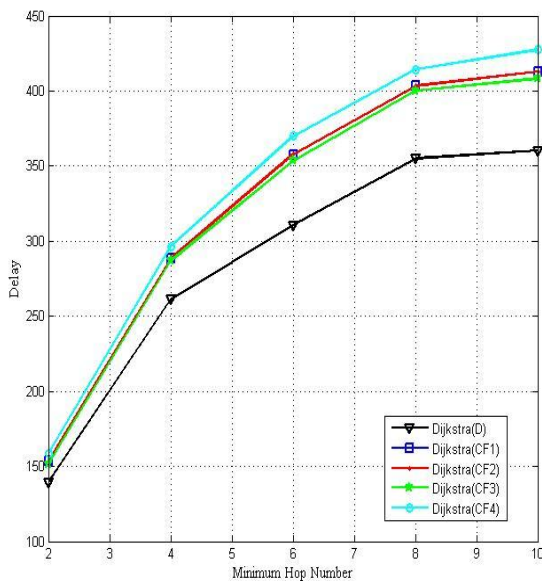


Figure 6. Delays for all functions

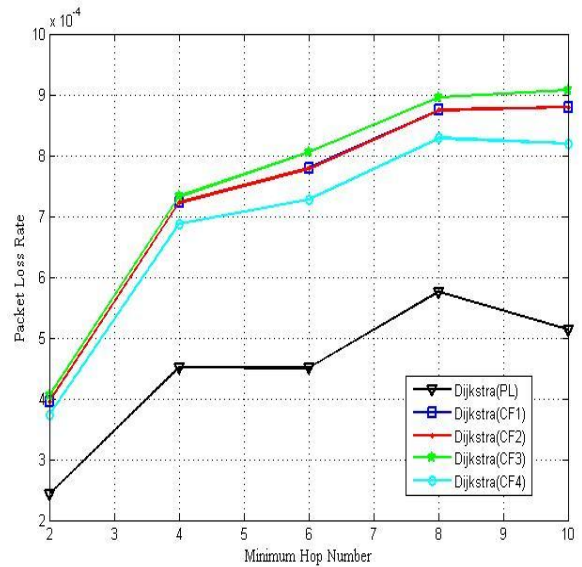


Figure 7. Packet loss rates for all functions

### 4. Conclusion

In this study, we proposed some effective composite cost functions correlating two different metrics, namely delay and packet loss rate, and represented the way and rationale of their construction. We obtained the composite functions to find the best path according to the metrics on any arbitrary networks without any constraints. We compared the composite functions against Dijkstra's algorithm with the individual metrics. The numerical results show that our composite functions are good when considering the balance between both metrics. The worst case ratios between two metrics in our functions are well balanced. The functions can also be extended to include more than two metrics. They may also cover bandwidth or jitter with supporting additional operations such as

exponentials used in several studies related with network traffic distributions.

## 5. Acknowledgments

The author would like to sincerely thank Savio S.H. Tse for sharing his comments during the preparation of this study.

This work was supported by Scientific Research Projects Coordination Unit of Istanbul University. Project number: 10590.

## 6. References

- [1] Hanzo II, L. and Tafazolli, R., "A Survey of QoS Routing Solutions for Mobile Ad Hoc Networks". *IEEE Communications Surveys & Tutorials*, Vol: 9, No: 2, pp. 50-70, 2007.
- [2] Yin, C.S., Chaw, L.T., and Yaacob, M., "Hop-by-Hop QoS Routing Using Statistical Distribution-Free Approach". *Malaysian Journal of Computer Science*, Vol: 18 No: 2, pp. 28-37, December 2005.
- [3] Brunsting, R.J., "Quality of Service Issues in Wireless Networks", in *An essay presented to the University of Waterloo*, Ontario, Canada, 1995.
- [4] Obreja, Ş.G. and Borcoci, E., "Interdomain QoS paths finding based on overlay topology and QoS negotiation approach". *Trends in Telecommunications Technologies*, InTech Publisher, pp. 345-365, 2010.
- [5] Iqbal, M., Wang, X., Li, S., and Ellis, T., "QoS scheme for multimedia multicast communications over wireless mesh networks". *IET Communications*, Vol: 4, No: 11, pp. 1312-1324, 2010.
- [6] Djarallah, N.B., Sauze, N.L., Pouyllau, H., Lahoud, S., and Cousin, B., "Distributed E2E QoS-Based Path Computation Algorithm Over Multiple Inter-Domain Route", *Int. Conf. on P2P, Parallel, Grid, Cloud and Internet Computing (3PGCIC)*, Barcelona, pp. 169-176, 2011.
- [7] Ali, N.B., Molnár, M., and Belghith, A., "Multi-constrained QoS Multicast Routing Optimization", *inria-00271795, version 2 - 10*, 2008.
- [8] Yampolskiy, M., Hommel, W., Lichtinger, B., Fritz, W., and Hamm, M.K., "Multi-Domain End-to-End (E2E) Routing with multiple QoS Parameters-Considering Real World User Requirements and Service Provider Constraints", *Second International Conference on Evolving Internet (INTERNET)*, Valencia, pp. 9-18, 2010.
- [9] Bertrand, G., Lahoud, S., Texier, G., and Molnár, M., "Computation of Multi-Constrained Paths in Multi-Domain MPLS-TE Networks", *Next Generation Internet Networks*, Aveiro, pp.1-8, 2009.
- [10] Masip-Bruin, X., Yannuzzi, M., Serral-Gràcia, R., Domingo-Pascual, J., Enriquez-Gabeiras, J., Callejo, M.Á., Diaz, M., Racaru, F., Stea, G., Mingozzi, E., Beben, A., Burakowski, W., Monteiro, E., and Cordeiro, L., "The EuQoS System: A Solution for QoS Routing in Heterogeneous Networks". *IEEE Communications Magazine*, pp. 96-103, 2007.
- [11] Shin, D.-w., Chong, E.K.P., and Siegel, H.J., "Multi-postpath-based lookahead multiconstraint QoS Routing". *Journal of the Franklin Institute*, Vol: 349, No: 3, pp. 1106-1124, 2012.
- [12] Xue, Q. and Ganz, A., "Ad hoc QoS on-demand routing (AQOR) in mobile ad hoc networks". *Journal of Parallel and Distributed Computing*, Vol: 63, pp. 154-165, 2003.
- [13] Yuan, X. and Liu, X., "Heuristic Algorithms for Multi-Constrained Quality of Service Routing", *IEEE INFOCOM*, Vol: 2, pp. 844-853, 2001.
- [14] Yiltas, D. and Perros, H., "Quality of service-based multi-domain routing under multiple quality of service metrics". *IET Communications*, Vol: 5, No: 3, pp. 327-336, 2011.
- [15] Van Mieghem, P., De Neve, H. and Kuipers, F., "Hop-by-hop quality of service routing". *Computer Networks*, Vol: 37, pp. 407-423, 2001.
- [16] Jaffe, J.M., "Algorithms for finding paths with multiple constraints". *Networks*, Vol: 14, pp. 95-116, 1984.

## Biography

**Derya Yiltas-Kaplan** received the B.Sc., M.Sc. and Ph.D. degrees in computer engineering from Istanbul University, Istanbul, Turkey, in 2001, 2003 and 2007 respectively. She studied as a post-doctorate researcher at North Carolina State University in USA between 2008 and 2009 for one year. She was granted with scholarships by The Scientific and Technological Research Council of Turkey during her Ph.D. and post-doctorate studies. Now, she is an Assistant Professor in Department of Computer Engineering, at Istanbul University. Her research interests include wireless communications and networking.







# ELIMINATING NEGATIVE EFFECT OF INVERTER-BASED DGs ON FUSE-RECLOSER COORDINATION IN DISTRIBUTION SYSTEMS

M.R.SHAKARAMI<sup>1</sup>, F. NAMDARI<sup>2</sup> and M. SALEHI<sup>3</sup>

<sup>1,2,3</sup> Lorestan University, Faculty of Electrical Engineering, Khorramabad, Iran  
, namdari.f@lu.ac.ir, [salehi.mo@fe.lu.ac.ir](mailto:salehi.mo@fe.lu.ac.ir), [shakarami.mr@lu.ac.ir](mailto:shakarami.mr@lu.ac.ir)

**Abstract:** Despite many advantages of distributed generation (DG) sources, they may have a negative effect on the protection of distribution systems. In a distribution system, fuse-recloser protection scheme is designed such that the recloser could operate faster than the fuse to prevent fuse burning; but, the presence of DGs in fault conditions may lead to increased fuse current and thus faster performance of the fuse than the recloser and lack of coordination. In this paper, effect of DGs on fuse-recloser coordination was studied using analytical relations and simulation. A useful control method was presented for reducing the effect of DG on fuse-recloser coordination. Accordingly, direction of DG current was changed by controlling DG reactive power at the fault time, which reduced the fuse current. Results of the simulation on IEEE 13-bus system showed that the proposed control method was able to remove the negative effect of DG on fuse-recloser coordination.

**Keywords:** Distributed generation (DG), distribution system, fuse-recloser coordination.

## 1. Introduction

Distributed generation (DG) systems such as microturbines, solar cells, and photovoltaic systems are constantly increasing their penetration into electrical power networks [1]. Also, DGs have a suitable effect on different network aspects through meeting load demand increase without any need for developing transmission system, transmission losses, voltage regulation, reactive power compensation, and active power injection [2, 3]. However, despite many advantages of DGs for networks, they may have negative effects on the protection of distribution systems. For example, DGs can damage elements of the network in the case of islanding and cause problems for utilities [4].

DGs can have a negative effect on fuse-recloser coordination. Fuse-recloser protection scheme is designed such that the recloser acts faster than the fuse to prevent fuse burning; but, the presence of DGs in fault conditions may lead to increased fuse current, which causes faster performance of the fuse than recloser and thus lack of coordination [5-7]. To reduce effect of DG on the protection scheme, different methods have been proposed. In [8-10], attempts have been made to specify the maximum capacity by limiting DG capacity to reduce effect of DG on the protection system. In some references such as [11,12], the protection system has been modified and the grid is restructured using additional reclosers and breakers or directional and distance relays. Indeed, this method is

less common in distribution systems. In [13-15], fault current limiters (FCLs) have been used to reduce the effect of DG on the protection coordination of the distribution system. FCLs are the tools which show negligible impedance grid in conventional performance; but, their impedance rapidly increases in fault conditions. In [16], DG current size was limited based on fault intensity at the fault time.

In this paper, effect of DG on fuse-recloser coordination was first studied. Then, a new control method was presented for eliminating the effect of DG on fuse-recloser coordination. Accordingly, DG current direction was changed by changing the reactive power injected by DG into the grid at the fault time, which reduced the fuse current; as a result, the fuse did not operate before the recloser and coordination was maintained. Results of the simulation on the standard IEEE 13-bus system showed accuracy and usefulness of the proposed method.

## 2. Effect of DG on fuse – recloser coordination

Studies have shown that most of the faults in air distribution systems are temporary, and will be cleared during fast reclosing actions [10]. Figure (1) shows a sample of radial distribution feeder along with DG and protective equipment, i.e. fuse and recloser. When a fault occurs in the specified part, first, recloser R rapidly operates on the fast current-time curve for one or more times. If the fault exists after the first performance of the recloser, it should be removed by the fuse; in case the fuse cannot interrupt the fault current, then the recloser with

slow current–time curve removes the fault. For suitable coordination, current-time curve of the fuse and recloser is selected and regulated so that their fault current can be specified for all possible faults according to Figure 2. In the absence of DG, when a fault occurs with the fault current of  $I_{\text{fault}}$  within the range between  $I_{\text{min}}$  and  $I_{\text{max}}$ , fault currents are equal in the protective equipment; i.e.:

$$I_{\text{fault}} = I_R = I_F \tag{1}$$

Where  $I_R$  is the fault current seen by the recloser and  $I_F$  is the fault current seen by the fuse. In such a case, according to Figure (2), it is evident that the recloser acts faster than the fuse and the fuse-recloser coordination is always established. However, in the presence of DG in fault current, other currents of fuse and recloser are not equal and the current of the fuse is higher than that of the recloser. In this state, the fuse is more likely to act faster than the recloser against temporary faults and thus balance is lost according to Figure (3):

$$I_F = I_R + I_{\text{Margin}} \tag{2}$$

In which  $I_{\text{Margin}}$  is the difference between the currents of recloser and fuse for establishing fuse-recloser balance.

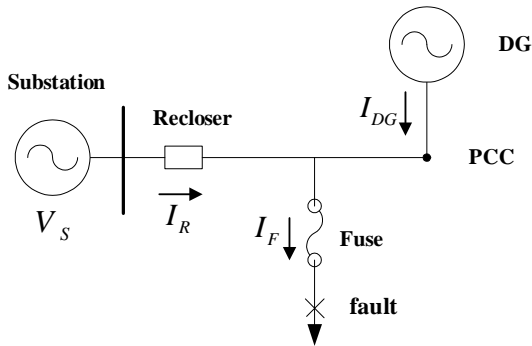


Figure 1. Sample typical distribution system.

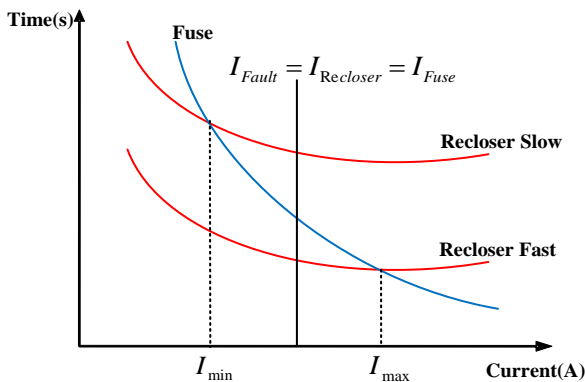


Figure 2. Sample coordination between recloser and fuse

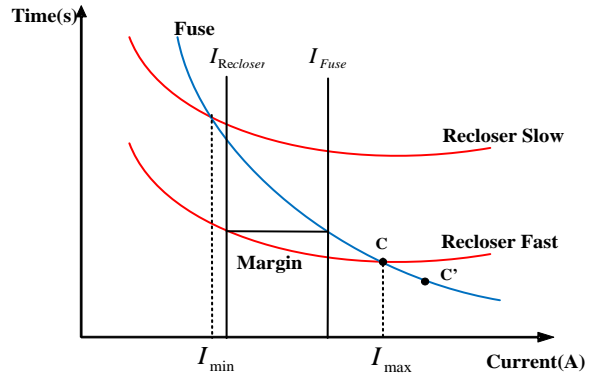


Figure 3. Fuse-recloser protection scheme in distribution feeder

On the other hand, according to Figure (1):

$$I_F = I_R + I_{DG} \frac{Z_{eq}}{Z_{eq} + Z_f} \tag{3}$$

Where  $I_{DG}$  is fault current of DG.  $Z_{eq}$  is equivalent impedance of substation and  $Z_f$  is fault impedance. Thus, to ensure the fuse-recloser coordination, it is necessary to:

$$I_{DG} < I_{\text{Margin}} \tag{4}$$

When DG capacity is higher or reactive power is injected into the network while fault impedance is low [16], equation (3) is not established and the current of the fuse increases and exceeds the coordination limit. According to Figure 3, point C is moved toward the right side, i.e. point C' and fuse-recloser coordination is lost. Thus, it is necessary to properly control DG current at fault moment in order to maintain the fuse-recloser coordination.

Another point is that, according to voltage and current vector diagram in Fig. 4, when DG supplies reactive power of the grid, a more negative effect is made on the fuse-recloser coordination than the case when DG injects active power into the grid. Based on Fig. 5, in the injection case of active power by DG, DG current ( $I_{DG}$ ) is in phase with the PCC voltage ( $V_{PCC}$ ) and almost 90 degrees of phase difference are observed between recloser current ( $I_R$ ) and  $V_{PCC}$ . Therefore, the relationship in (5) can be obtained:

$$I_R + I_{DG} < I_R + I_{DG} \tag{5}$$

In the injection case of reactive power by DG, 90 degrees of phase difference are observed between DG current ( $I_{DG}$ ) and the PCC voltage; also, the following equation is obtained:

$$I_R + I_{DG} \approx I_R + I_{DG} \tag{6}$$

These equations demonstrate that the fuse current is larger in the injection case of reactive power by DG, representing that DG in reactive power supply has a higher effect on fuse - recloser coordination than that in the active power supply.

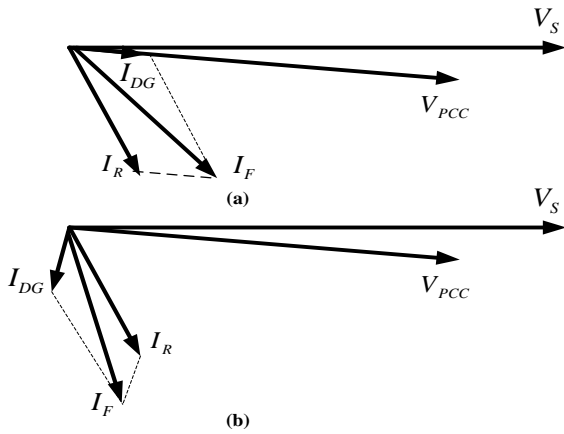


Figure 4. Voltage and current vector diagram (a) DG generates active power, (b) DG generates reactive power

### 3. The proposed method for reducing DG effect on fuse-recloser coordination

The proposed method for reducing DG effect on fuse-recloser coordination in this paper was based on the point that, change in the DG current direction leads to reduced fuse current. In fact, this task was performed by changing the direction of the reactive power injected by DG at the fault time. In the case of fault with low impedance ( $Z_f \ll Z_{eq}$ ), the following equation can be written according to (3):

$$I_F = I_R + I_{DG} \tag{7}$$

Considering the above equation, the fuse current can be reduced by changing the direction of DG current; but, the way  $I_{DG}$  changes at the fault time for inducing coordination should be considered. If  $I_{DG}$  changes at the fault time into  $I'_{DG}$  so that the fuse current and recloser becomes equal ( $I_F = I_R$ ), then, fuse-recloser coordination will be definitely maintained within the current limit between  $I_{min}$  and  $I_{max}$  as demonstrated in Fig 2. Therefore, equation (9) is obtained by placing  $I_F = I_R$  in the equation (8):

$$I_F^2 = I_R^2 + I'_{DG}{}^2 + 2 I_R I'_{DG} \cos \alpha \tag{8}$$

$$\cos \alpha = -\frac{I'_{DG}}{2 I_R} \tag{9}$$

This equation states that  $\alpha$  (the angle between two vectors  $I'_{DG}$  and  $I_R$ ) should be more than 90 degrees; i.e. DG absorbs reactive power from the grid at the fault time, which can be done in different states according to Fig. 5. In other words, it is performed for different DG currents ( $I_{DG1}, I_{DG2}, I_{DG3}, \dots$ ) and  $\theta_i$  angles ( $\theta_1, \theta_2, \theta_3, \dots$ ); in all of these states, fuse current

should be equal to recloser current and placed on the radii of the circle centered at O. Considering that  $\alpha_i = \theta_i + 90$ :

$$\sin \theta_i = \frac{I_{DG_i}}{2 I_R} \quad i=1,2,3,\dots \tag{10}$$

Assuming that  $I_d$  and  $I_q$  are active and reactive components of DG current and  $I_{DG}$  and  $I'_{DG}$  are DG short-circuit currents before and after applying the control, then, DG reactive current component is obtained using (11) according to Fig. 6:

$$I'_q = \frac{\tan \theta'}{\tan \theta} I_q \tag{11}$$

In this equation, angle  $\theta$  indicates the reactive power which DG injects into the grid before applying the control and angle  $\theta'$  shows the reactive power which DG absorbs after applying the control at the fault time from the grid. As discussed above, angle  $\theta'$  can have different values. In a special case, if DG current is changed so that its active component remains constant and only its reactive component changes and  $\theta = \theta'$ ; then, DG control structure will be simplified; i.e. only the direction of DG reference current component changes at the fault time. The above state was simulated in this paper. On the other hand, components of the reference DG active and reactive currents could be obtained based on the reference DG active and reactive power as follows [2]:

$$P_{ref} = V_d I_{dref} \tag{12}$$

$$Q_{ref} = -V_d I_{qref} \tag{13}$$

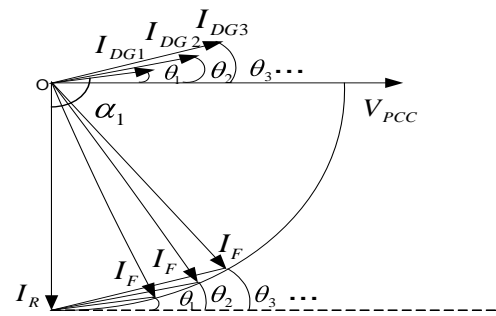


Figure 5. Vector diagram of fuse, recloser, and DG current in different states

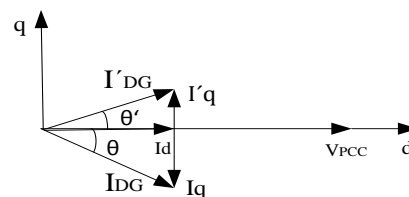


Figure 6. Vector diagram of DG current in the proposed control method

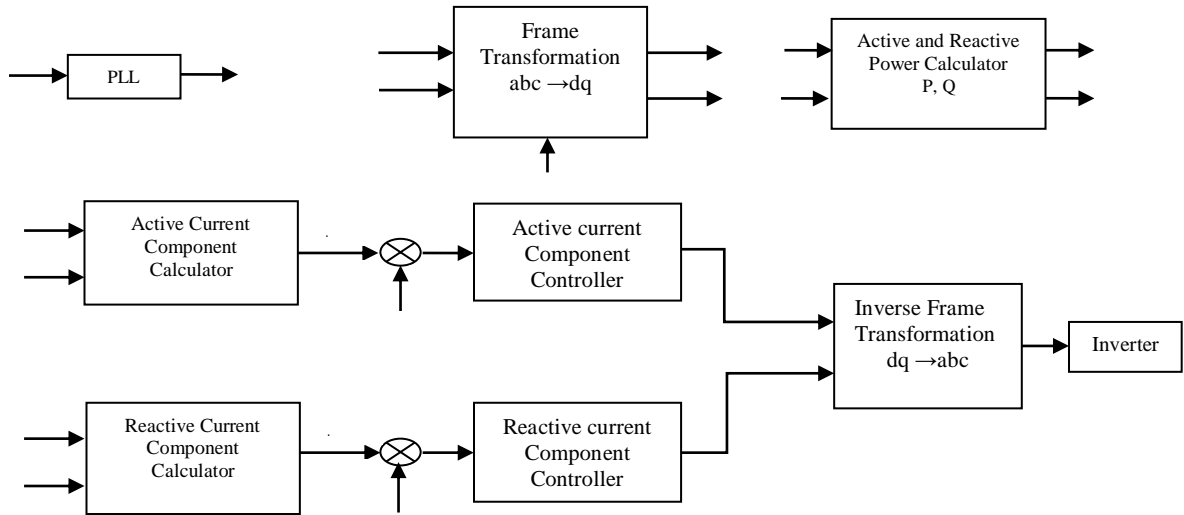


Figure 7. DG control structure based on current-controlled inverter

In (12) and (13),  $V_d$  is voltage component of  $V_{PCC}$  on axis d. Therefore, DG control structure is expressed as Fig. 7. Based on standard IEEE.1547 [17], when  $V_{PCC} < 0.88 pu$ , the grid is in an abnormal state. Accordingly, DG detects the fault and the proposed control method can be applied. The proposed algorithm for controlling DG current to establish fuse-recloser coordination is shown in Fig. 8.

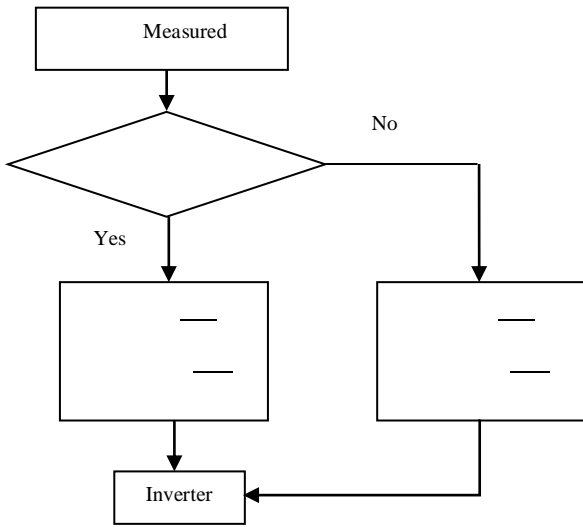


Figure 8. The proposed algorithm for determining DG reference current

4. Simulation results

To evaluate the proposed method, IEEE 13-bus distribution system [18] (Fig. 9) was simulated in MATLAB software and an inverter-based DG [11] with the control structure shown in Fig. 7 was connected at

node 645. To study fuse-recloser coordination a three-phase fault was applied to bus 646. Characteristic current-time curve of the fuse and recloser which was used in this simulation is shown in Fig. 10. In this simulation, before the presence of DG, point A occurs for fault resistance of  $11\Omega$ , and point B occurs for fault resistance of  $0.01\Omega$ . In other words, the recloser and fuse operate correctly for fault resistances between 0.01 to  $11.5\Omega$ . Fig. 11 shows the consequence of adding DG at low and high penetration levels (penetration level =  $P_{DG} P \times 100$ ) on the fuse and recloser current when a  $0.01\Omega$  fault occurs. As Figure 11 reveals, after adding DG at two penetration levels, recloser current remained almost constant; but, fuse current increased. Fig. 12 demonstrates the difference between fuse and recloser fast operation times after adding DG at different penetration levels for a  $0.01\Omega$  fault.

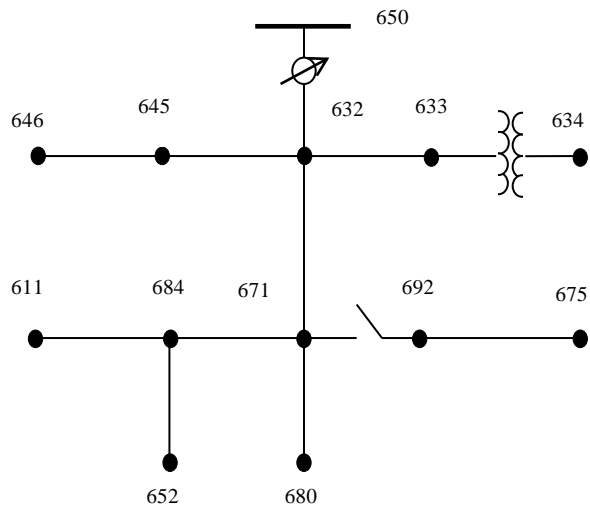


Figure 9. IEEE 13-node test feeder system

Fig. 12 represents that, in the presence of DG, the fuse would operate faster than the recloser and the coordination would be removed. The fuse current was higher when DG injected reactive power than the case in which active power was injected. Difference in operation time between fuse and recloser in this case is shown in Fig. 13.

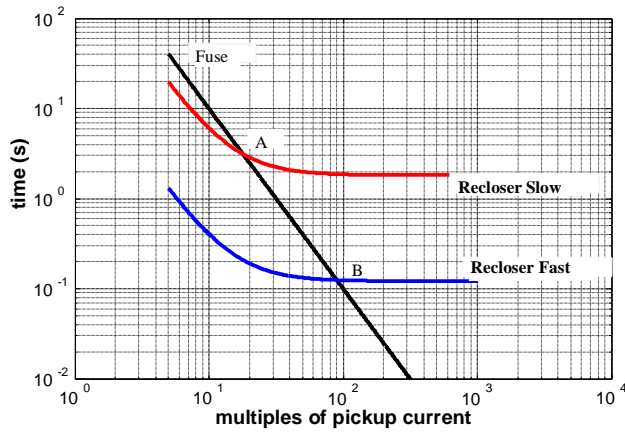


Figure 10. Fuse-recloser coordination in the simulated system

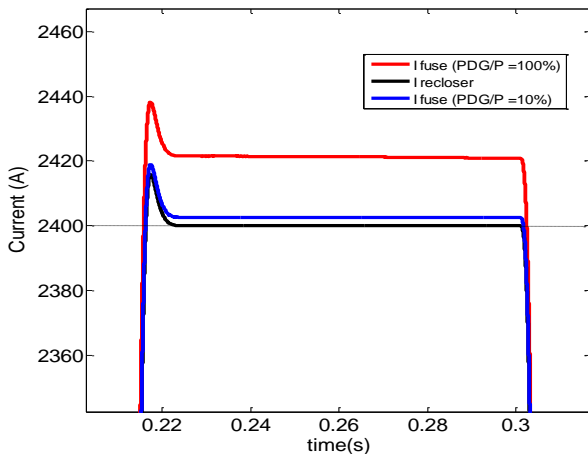


Figure 11. recloser and fuse currents in the presence of DG

By comparing Figs. 12 and 13, the negative effect of DG on fuse-recloser coordination was revealed to be higher than the injection case of the reactive power by DG. Fig. 14 demonstrates that the presence of DG had a lower effect on coordination at high fault impedance (0.1 ohm); this effect was more evident when DG supplied more power of the grid. Fig. 15 shows fuse current with and without using the proposed control method in a fault with 0.1Ω resistance. It is clear that, as a result of applying the proposed control method, the fuse current was considerably reduced from the coordination limit.

Fig. 16 shows that, after applying the control method, direction of DG output reactive current component was reversed compared to its previous current at the fault time ( $t= 0.2$  s). In other words, direction of the DG reactive power was changed in

order to reduce the fuse current and maintain the fuse-recloser coordination.

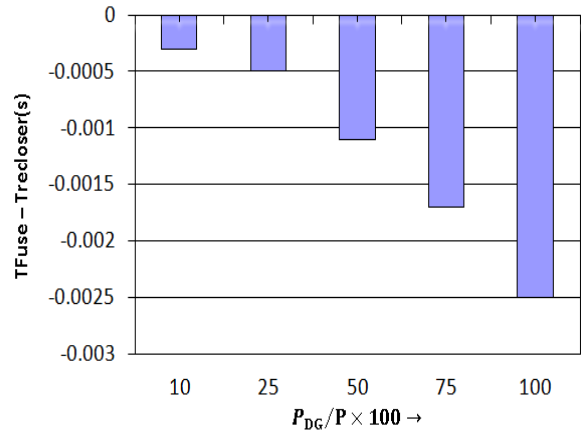


Figure 12. Difference between fuse and recloser operation time after adding DG for 0.01Ω fault (injection of active power)

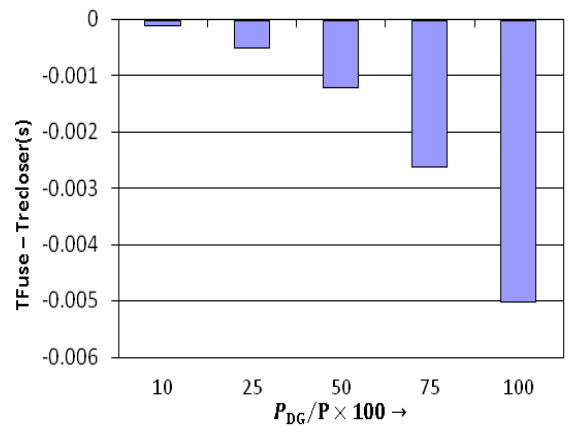


Figure 13. Difference between fuse and recloser operation time after adding DG for 0.01Ω fault (injection of reactive power)

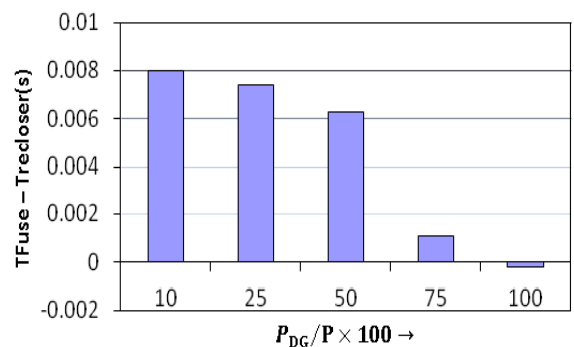
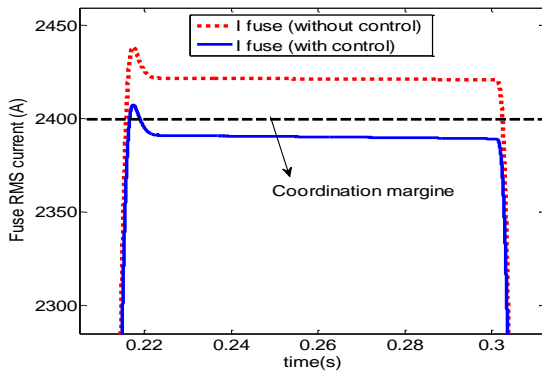
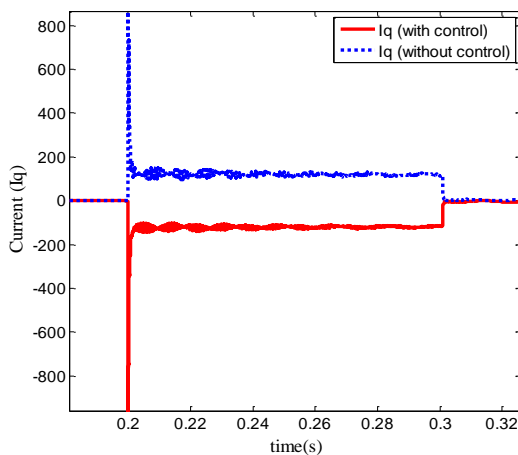


Figure 14. Difference between fuse and recloser operation time after adding DG for 0.1Ω fault



**Figure 15.** Fuse current with and without applying the control method at the fault impedance of 0.1 ohm in the presence of DG



**Figure 16.** DG reactive current component before and after applying the control method

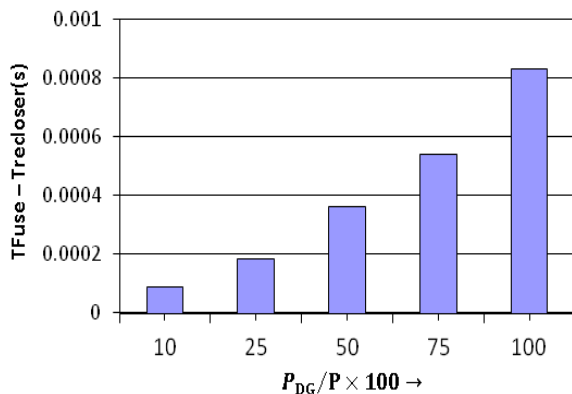


**Figure 17.** Difference between fuse and recloser operation time for 0.01 ohm fault by applying the control method

Fig. 17 shows effect of the proposed control method on the coordination. Accordingly, it is clear that the control method properly removed mis-coordination resulting from the presence of DG at low fault impedance.

### 5. Conclusion

In this paper, effect of DG on fuse-recloser protection coordination was shown using analytical relations and simulation. In fact, DG at low fault impedance can remove fuse-recloser coordination. It could also increase the current passing through the fuse at the fault time and cause faster performance of the fuse than recloser; this effect increased at the injection time of reactive power by DG. To overcome this problem, a simple and useful control method was presented, based on which the direction of DG current changed at the fault time in proportion to the fault intensity. Simulation results on an IEEE 13-bus distribution system showed that this method could properly reduce the negative effect of DG on fuse-recloser coordination. In addition to its simplicity, other advantages of the proposed method were that it could be applied on the DG side and did not need any changes in the main adjustments of the protection system.

### 6. References

- [1] J.M. Guerrero, F. Blaabjerg, T. Zhelev, K. Hemmes, E. Manmasson, S.Jemei, M. P. Comech, R. Granadino, and J. I. Frau, "Distributed generation: Toward a new energy paradigm," *IEEE Ind. Electron. Mag.*, vol. 4, no. 1, pp. 52–64, Mar. 2010.
- [2] J. He, Y.W. Li, and S.Munir, "A flexible harmonic control approach through voltage controlled DG-grid interfacing converters," *IEEE Trans. Ind. Electron.*, vol. 59, no. 1, pp. 444–455, Jan. 2012.
- [3] A. Piccolo and P. Siano, "Evaluating the impact of network investment deferral on distributed generation expansion," *IEEE Trans. Power Syst.*, vol. 24, no. 3, pp. 1559–1567, Aug. 2009.
- [4] X. Wang, W. Freitas, and W. Xu, "Dynamic non-detection zones of positive feedback anti-islanding methods for inverter-based distributed generators," *IEEE Trans. Power Del.*, vol. 26, no. 2, pp. 1145–1155, Apr. 2011.
- [5] R. A. Walling, R. Saint, R. C. Dugan, J. Burke, and L. A. Kojovic, "Summary of distributed resources impact on power delivery system," *IEEE Trans. Power Del.*, vol. 23, no. 3, pp. 1636–1644, Jul. 2008.
- [6] M. H. Kim, S. H. Lim, J. F. Moon, and J. C. Ki, "Method of recloserfuse coordination in a power distribution system with superconducting fault current limiter," *IEEE Trans. Appl. Supercond.*, vol. 20, no. 3, pp. 1164–1167, Jun. 2010.
- [7] H. Cheung, A. Hamlyn, L. Wang, C. Yang, and R. Cheung, "Investigations of impacts of distributed generation on feeder protection," in *Proc. IEEE Power Energy Soc. Gen. Meet.*, 2009, pp. 1–7.
- [8] T. Seegers et al., "Impact of distributed resources on distribution relay protection," Rep. to Line Protection Subcommittee, Power System Relay Committee, Power Engineering Society, IEEE, 2004.
- [9] J. Chen, R. Fan, X. Duan, and J. Cao, "Penetration level optimization for DG considering reliable action of relay protection device constrains," in *Proc. Int. Conf. Sustainable Power Gener. Supply*, 2009, pp. 1–5.
- [10] S. Chaitusaney and A. Yokoyama, "Prevention of reliability degradation from recloser-fuse miscoordination due to distributed generatio," *IEEE Trans. Power Del.*, vol. 23, no. 4, pp. 2545–2554, Oct. 2008.



- [11] T. K. Abdel-Galil, A. E. B. Abu-Elnien, E. F. El-saadany, A. Girgis, Y. A.-R. I. Mohamed, M. M. A. Salma, and H. H.M. Zeineldin, "Protection coordination planning with distributed generation," Canmet Energy Technology Centre, Varennes, QC, Canada, 2007.
- [12] H. B. Funmilayo and K. L. Buylar-Purry, "An approach to mitigate the impact of distributed generation on the overcurrent protection scheme for radial feeders," in *Proc. IEEE Power Syst. Conf. Expo.*, 2009, pp. 1–11.
- [13] W. El-Khattam and T. S. Sidhu, "Restoration of directional utilizing fault current limiter," *IEEE Trans. Power Del.*, vol. 23, no. 2, pp. 576–585, Apr. 2008.
- [14] H. Yamaguchi and T. Kataoka, "Current limiting characteristics of transformer type superconducting fault current limiter with shunt impedance and inductive load," *IEEE Trans. Power Del.*, vol. 23, no. 4, pp. 2545–2554, Oct. 2008.
- [15] Y. Zhang and R. A. Dougal, "Novel dual-FCL connection for adding distributed generation to a power distribution utility," *IEEE Trans. Appl. Supercond.*, vol. 21, no. 3, pp. 2179–2183, Jun. 2011.
- [16] H. Yazdanpanahi, Y. W. Liand W. Xu, "A New Control Strategy to Mitigate the Impact of Inverter-Based DGs on Protection System," *IEEE Trans. Smart Grid.*, vol. 3, no. 3, pp. 1427–1436, sep. 2012.
- [17] IEEE 1547-2003, IEEE Standard for Interconnecting Distributed Resources with Electric Power System, , 2003.
- [18] W. H. Kersting, "Radial distribution test feeders," in *Proc. IEEE Power Eng. Soc. Winter Meet.*, 2001, pp. 908–912.



**Mahmoud Reza Shakarami** received the B.S. degree from Shahid Chamran University of Ahvaz, Khuzestan, Iran, in 2004 and the M.S. degree in electric power engineering and the Ph.D. degree from University of Science and Technology, Tehran, Iran in 2006 and 2010, respectively. He is now an Assistant Professor in Lorestan University,

Lorestan, Iran. His research interests are primarily in power system dynamics and stability and flexible AC transmission system (FACTS).



**Farhad Namdari** was born in 1972 in Khorram Abad, Iran. He received his BSc in 1995 at the Iran University of Science and Technology (IUST), MSc in 1998 at the Tarbiat Modarres University (TMU), Iran, and PhD in 2006 at the IUST all in Electrical Power Engineering. From 2003 he worked with Queen's University, Belfast as Research Associate for a period of 11 months. From 2009 he joined Lorestan University (LU), Iran as Lecturer. He also has 14 years of experience as consultant with Cement Industries. From 2014 Dr Namdari is an IEEE member. His fields of interests are power system protection, smart grids, power system transients, power system operation and control and Artificial Intelligent (AI) techniques in power systems.



**Moslem Salehi** was born in Alashtar, Iran, in 1980. He received his M.Sc. degree from Shahid Rajae Teacher Training University in Tehran, Iran in 2011. he is currently pursuing the Ph.D. degree at Lorestan University, Khorramabad, Iran. His research interests include power system protection, smart grids, power system transients and fault location for transmission lines.





## MODELING OF GRAVITY ANOMALIES DUE TO 2D GEOLOGICAL STRUCTURES USING GENETIC ALGORITHM

Onur OSMAN<sup>1</sup> and A. Muhittin ALBORA<sup>2</sup>

<sup>1</sup>Istanbul Arel University Department of Electrical and Electronics Eng. 34537 Büyükçekmece/Istanbul Turkey

<sup>2</sup>Istanbul University, Engineering Faculty, Geophysical Department, 34320, Avcilar, Istanbul, Turkey

e-mail: [onur.osman@gmail.com](mailto:onur.osman@gmail.com), [muhittin@istanbul.edu.tr](mailto:muhittin@istanbul.edu.tr)

---

**Abstract:** In this paper, a new modeling technique is introduced using Genetic Algorithm (GA). In this method, Genetic algorithm (GA) is modified and used as an optimization method in geophysics applications. The problem at hand is to find the best model for the cross-section, which its anomalies fit the observed ones. Optimization methods are generally used in inversion problems to find some parameters, which describe underground structures. The model shape is limited with the chosen parameters. In our modeling technique, firstly, cross section is divided into prismatic pieces. Then, genetic algorithm finds models in each generation, which have geometries constitute of prismatic structures, and obtains the best model that fits its anomaly to the observed one. In this process, the density differences of each prismatic piece are assumed to be constant. Therefore, the model obtained by using GA, the structure is shape independent. Moreover, any kind of structure can be modeled with the proposed method using constant density difference for underground structure. We give two synthetic examples; the first one is U type and the other one is a basin model. Based on the anomalies with acceptable errors, GA finds the models satisfactory. Mean Errors (MEs) of these two synthetic modes are 0.087 mGal and 0.073 mGal respectively. Then, Godavari Valley models of [1], [2] are considered to compare our proposed modeling technique. Our model is found to be similar to these models. After demonstrate the reliability of the technique, proposed method is applied to Sivas-Gurun basin and the anomaly of the model has only 0.17 mGal ME.

**Keywords:** Genetic Algorithm (GA), Gravity anomaly modeling, Geophysics.

---

### 1. Introduction

The problem in modeling is to find the closest model for the cross-section, which its anomalies fit the observed ones. A new modeling technique in geophysics is introduced using Genetic Algorithm (GA). In this method, Genetic algorithm (GA) is used as an optimization method in geophysics applications. One of the most popular and conventional method to determine geometrical shape and physical properties of subsurface geological anomalies is the inversion technique. The parameters of the model such as surface length, depth, and side angles according to the surface are decided before the inversion and therefore, the shape of the model, which is obtained after inversion, is limited with the chosen parameters. Therefore, inversion method is shape dependent.

Modeling the structure and finding its parameters according to the anomaly are vital in geophysics. In GA

modeling technique, the cross section is first divided into prismatic pieces (Figure 1). Then, genetic algorithm finds models in each computation iteration, which have geometries constitute of prismatic structures, and obtains the best model whose anomaly fits observed one. In this process, the density differences of each prismatic piece are assumed to be constant, which means the average density difference calculated from the anomaly map is used for entire region of the model. Therefore, the model obtained by using GA is shape independent in contradistinction to inversion method. Thus, information about the dimensions of the structure can be obtained.

Starting with a set of initial solutions, acceptable result is achieved by modifying the solution set by mimicking the evolutionary behavior of biological systems. Therefore, Genetic Algorithm (GA) is used to find the parameters of the structure causing the observed anomaly. Genetic

algorithms are a searching method especially for the global optimization of irregular, multi-modal functions, which have lots of maxima and minima..

$g_{1,1}^f$	$g_{1,2}^f$	.....	$g_{1,n_c}^f$
$g_{1,n_c+1}^f$	$g_{1,n_c+2}^f$	.....	$g_{1,2n_c}^f$
.	.	.....	.
.	.	.....	.
.	.	.....	.
$g_{1,(n_r-1) \times (n_c+1)}^f$	$g_{1,(n_r-1) \times (n_c+2)}^f$	.....	$g_{1,n_r \times n_c}^f$

Figure 1. Mapping the first individual to cross-section.

Genetic Algorithm technique (GA) is parameter-optimization method especially applied for modeling complex geophysical anomalies. The GA technique is an inverse modeling technique, which works on finding the geological anomaly by the well-known method of minimizing the error between the observed and computed anomalies. With this statistical approach, the obtained results are not exact in nature, but give a model having an anomaly which is as close as possible to the observed anomaly.

### 2. Historical Note

It could be said that Genetic Algorithm was started by [3], and GA has been developed by [4], [5], [6], and [7].

In geophysics gravity anomalies of the sedimentary basin is interpreted by [2], then they proposed a model for Godavari Vally. [1], applied asymmetrical trapezoidal modeling for Godavari Vally and obtains close results. it is also used the same region, Godavari Vally, to show the truth of this modeling technique. A standard strategy in genetic algorithm inversion is discussed in [8]. [9] use Genetic Algorithm in plane-wave inversion method in seismograms. [10] apply GA to background velocity inversion problems. [11] use GA to find Hypocenter location. [12] use GA in inversion of seismic refraction data. [13] and [14] use GA in inversion problems. Genetic Cellular Neural Networks (GCNN) is applied to geophysics by [15]. Real-valued Genetic Algorithm (GA) was designed and implemented to minimize the reflectivity and/or transmissivity of an arbitrary number of homogeneous, lossy dielectric or magnetic layers by [16]. But here, it can be modified GA to find the model of the anomaly without using any parameter about the shape of the model, which needs to be minimized, as other studies.

### 3. Theoretical Background of Genetic Algorithm

In the proposed algorithm, cross-section is divided into prismatic pieces. The width and the height of the pieces could be any value and determine the details of the model. The value of each pieces can be 0 or  $\Delta\rho$  (average density

difference). Prismatic pieces, which have  $\Delta\rho$  values, form the model. Genetic Algorithm (GA) searches the best prismatic pieces to set their values to  $\Delta\rho$ . At the end of the GA process, the best model, which its anomaly fits to the desired one, is obtained.

In GA, all individuals are created in random manner in the first generation. Each individual is assumed as a different model. Therefore in the first generation or iteration of GA there are lots of random models and the number of individuals is known as population of GA. These individuals are mapped to the cross-section and, weight function of each individual is calculated. The weight function to be minimized is the mean square error of the anomaly of individual according to the desired anomaly. Then, errors are found for each individual. Worst individuals have large errors and best individuals have small errors. Worst individuals are dismissed and the best ones are taken. To complete the total number of individuals in the current generation according to the population, best ones are automatically repeated by the software themselves. Different from the conventional GA, mutation is applied before crossover. Every two individuals are designated as parents and some mutations appeared in their genes. In crossover, these specified two individuals create two different child individuals and their genes are the combinations of the previous two. After that, these individuals are mapped to the cross-section and genes without any neighbor -individual are dismissed. Hence, new generation is created and all the steps of the algorithm are repeated until the error is minimized sufficiently. If needed or if there are some drill information, some prismatic pieces of the cross-section is assumed to be the part of the model in each individual in all generations of GA.

In general, average density difference is known or can be computed for that cross-section. In this modeling technique, GA can be run for different  $\Delta\rho$  values, hence, the best  $\Delta\rho$  and the best model which its anomaly fits the desired one are obtained.

### 4. Modeling in Geophysics: Concept of Genetic Algorithm

In order to apply genetic algorithm to find the model of the cross-section, which the most similar anomaly, the proposed cross-section needs to be divided into rows and columns. Each prismatic particle in cross-section is called unit. Thus, cross-section can be represented as units with a known depths and lengths. There are  $n_r$  rows and  $n_c$  columns. The number of units is  $n_r \times n_c$ . In genetic algorithm, each gene in an individual indicates each unit in a cross-section. The value of the gene can be zero or density difference of the model  $\Delta\rho$ . Therefore, individuals in the cross-section can be represented as,

$$\mathbf{I}^t = \begin{bmatrix} \mathbf{g}_1^t \\ \mathbf{g}_2^t \\ \vdots \\ \mathbf{g}_m^t \end{bmatrix} = \begin{bmatrix} g_{1,1}^t & g_{1,2}^t & g_{1,3}^t & \cdots & \cdots & g_{1,n}^t \\ g_{2,1}^t & g_{2,2}^t & g_{2,3}^t & \cdots & \cdots & g_{2,n}^t \\ \vdots & \vdots & \vdots & \ddots & & \vdots \\ \vdots & \vdots & \vdots & & \ddots & \vdots \\ g_{m,1}^t & g_{m,2}^t & g_{m,3}^t & \cdots & \cdots & g_{m,n}^t \end{bmatrix} \quad (1)$$

In this formula ,  $\mathbf{I}^t$  is the vector of the  $t^{\text{th}}$  generation.  $\mathbf{g}$  is an individual which consists of genes  $g$ .  $m$  is the number of individuals in every generation and can be chosen arbitrarily but must be even. If  $m$  is not large enough, error cannot be minimized sufficiently.  $n$  is the number of genes and can be computed as  $n = n_r \times n_c$ .

In the first generation, values of the genes are randomly chosen as zero or  $\Delta\rho$ . Then, each individual is mapped to cross-section as in Figure 1.

The anomaly of the cross-section for the first individual at position  $z$  on the ground is computed as below considering prismatic anomaly model [17],

$$A(z) = \sum_{x=0}^{n_c-1} \sum_{h=0}^{n_r-1} 2 \times 6.67 \times 10^{-8} \times D \rho \times \{ (x \times wdt - z \times wdt) \ln \left( \frac{(h \times dpt + dpt)^2 + (x \times wdt - z \times wdt)^2}{(h^* dpt)^2 + (x \times wdt - z \times wdt)^2} \right) - ((x \times wdt - z \times wdt) - wdt) \ln \left( \frac{(h \times dpt + dpt)^2 + ((x \times wdt - z \times wdt) - wdt)^2}{(h \times dpt)^2 + ((x \times wdt - z \times wdt) - wdt)^2} \right) + (h \times dpt + dpt) (\arctan \left( \frac{x \times wdt - z \times wdt}{h^* dpt + dpt} \right) - \arctan \left( \frac{x \times wdt - z \times wdt - wdt}{h^* dpt + dpt} \right)) - h \times dpt (\arctan \left( \frac{x \times wdt - z \times wdt}{h^* dpt} \right) - \arctan \left( \frac{x \times wdt - z \times wdt - wdt}{h^* dpt} \right)) \} \quad (2)$$

All the anomalies of points  $z$  from 0 to  $n_c-1$ ,  $A(z)$ , are computed and compared with the original anomaly.  $wdt$  and  $dpt$  are width and depth of each unit.  $x$  and  $h$  are column and row indexes of the units in cross-section. Mean Error (ME) of the individual is designated as the weight function. Ascending sort is applied to all individuals according to their MEs and some of them at the bottom are dismissed after this sort. The number of worst individuals is determined by a rule of keeping the value below the half of the number of individuals. The worst individuals are replaced with the best ones, which are at the top of the list. These individuals, which are obtained after this step, are called chosen individuals.

Before creating the new generation, mutation is applied to the chosen individuals. In this process, some genes are changed with probability of mutation. The value of these genes is turned to  $\Delta\rho$  (*the contrast of the model*) if it is 0 or turned to 0 if it is  $\Delta\rho$ . Thus, generations can pass local minimums and continues for global minimum of weight function.

To avoid having the same individuals for next generations, location of the individuals in (1) are changed, which is called interleaving. Then, new generation is obtained by using crossover technique. Every two sequential individuals are separated into two parts and the

separation point is chosen randomly for each pair as shown in below for the first pair.

$$\mathbf{g}_1^t = g_{1,1}^t \ g_{1,2}^t \ g_{1,3}^t \ g_{1,4}^t \bullet g_{1,5}^t \ g_{1,6}^t \cdots \cdots g_{1,n}^t \quad (3)$$

$$\mathbf{g}_2^t = g_{2,1}^t \ g_{2,2}^t \ g_{2,3}^t \ g_{2,4}^t \bullet g_{2,5}^t \ g_{2,6}^t \cdots \cdots g_{2,n}^t \quad (4)$$

Then these two individuals are crossed-over as shown in (5) and (6).

$$\mathbf{g}_1^t = g_{1,1}^t \ g_{1,2}^t \ g_{1,3}^t \ g_{1,4}^t \ g_{2,5}^t \ g_{2,6}^t \cdots \cdots g_{2,n}^t \quad (5)$$

$$\mathbf{g}_2^t = g_{2,1}^t \ g_{2,2}^t \ g_{2,3}^t \ g_{2,4}^t \ g_{1,5}^t \ g_{1,6}^t \cdots \cdots g_{1,n}^t \quad (6)$$

After these steps, cross-sections of the individuals indicated may not have a block structure. Thus, units with a density difference  $\Delta\rho$  in the cross-section, which don't have any neighbor units with a density difference  $\Delta\rho$ , are set to zero. Then, whole process is repeated until the global minimum or sufficient error minimization is reached. It is given two synthetic examples; the first one is U type and the other one is a basin model. Based on the anomalies with acceptable errors, GA finds the models satisfactory. Mean Errors (MEs) of these two synthetic modes are 0.087 mGal and 0.073 mGal respectively.

## 5. Method Application and Results

### 5.1. Synthetic Data 1

In the first synthetic data, it is used U type model, which is shown in Figure 2. The width and the depth of each unit is 100m and the density difference  $\Delta\rho$  is 1 gr/cm<sup>3</sup>. The anomaly of this model is calculated with the prismatic model formulation, which is given in equation 2. Figure 2 shows the anomaly curve of the model.

In genetic algorithm, the purpose is to find a model, in which its anomaly closes to the observed anomaly, given in Figure 2. The first parameter of the genetic algorithm is the number of individuals in one generation and it is chosen as 160. There are 210 genes in each individual. This value is the number of units in the cross-section. The second parameter is the number of individuals, which have worst errors, and it is chosen as 16. These individuals are replaced with the best 16 ones. The last parameter is the ratio of mutation. In our experiments 0.3% seems to be the best value for mutation.

At the end of the 125<sup>th</sup> generation, it is interrupted the process, because the error of the system has become quite constant. The best individual is shown in Figure 2 with dashed lines. Its anomaly and observed anomaly are given in Figure 2. It is not easy to distinguish these two anomalies, because the anomaly of the model, obtained from genetic algorithm, fits the target anomaly exactly. Mean error is only 0.087 mGal.

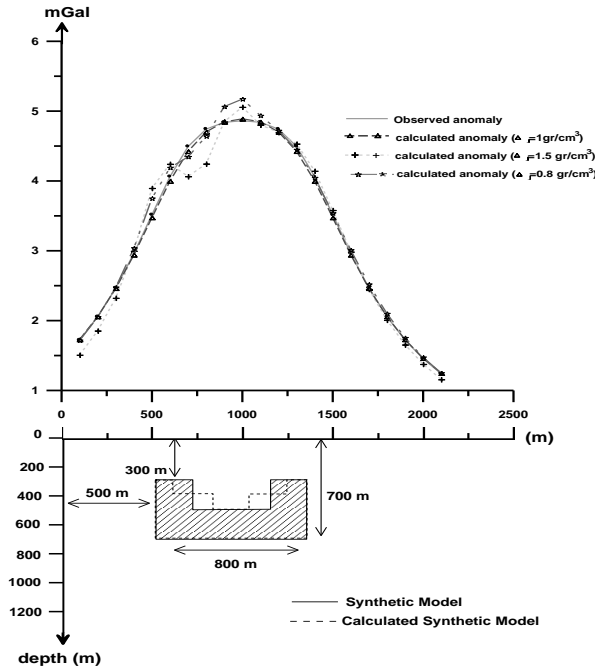


**Figure 2.** First synthetic model: Observed and calculated cross sections (width and depth of each unit is 100 meters and  $\Delta\rho = 1 \text{ gr/cm}^3$ ) and their related underground models. Observed cross-section is indicated with solid line and its structure is given with hatched area. For  $\Delta\rho = 1.5 \text{ gr/cm}^3$ , calculated cross section is shown with (+) symbol. For  $\Delta\rho = 0.8 \text{ gr/cm}^3$ , calculated cross section is shown with ( $\star$ ) symbol. For  $\Delta\rho = 1 \text{ gr/cm}^3$ , calculated cross section is shown with ( $\Delta$ ) symbol and its model is given with dashed lines in cross-section.

**5.2. Synthetic Data 2**

In the second synthetic data, we consider a basin model, which is given in Figure 3. The width and the depth of each unit is 100m and the density difference  $\Delta\rho$  is  $2 \text{ gr/cm}^3$ . The anomaly of this model is calculated with the prismatic model formulation, which is given in equation 2. Figure 3 shows the observed anomaly curve of the basin model. There are 320 individuals in each generation and 210 genes in each individual. The number of worst individuals, which are replaced with the best ones, is chosen as 32. Lastly, ratio of mutation is kept constant at 0.3%.

At the end of the 182<sup>th</sup> generation, the model with dashed lines in Figure 3 is reached. Its anomaly and observed anomaly are shown in Figure 3. It can be said that these are exactly the same, because mean error is 0.073 mGal. Synthetic model and calculated model are very close to each other. There are only two different units, which are at the bottom of the model.

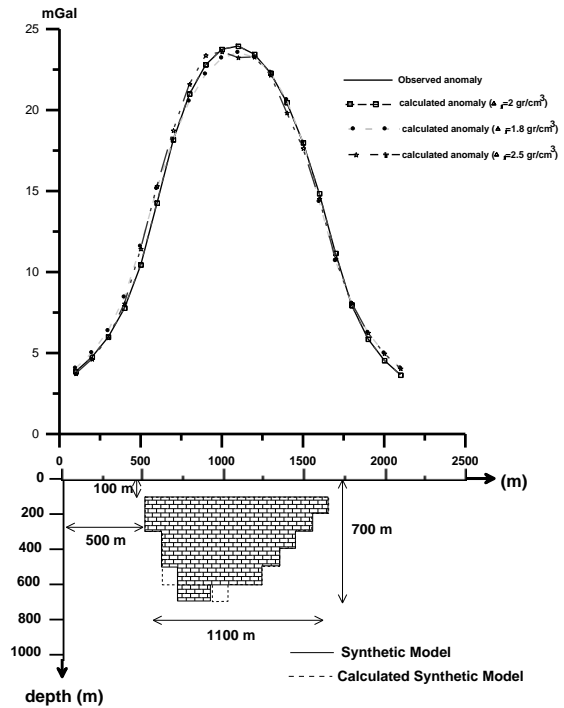


**Figure 3.** Second Synthetic Model: Observed and calculated (Segmented Genetic Algorithm) cross sections (width and depth of each unit is 100 meters and  $\Delta\rho = 2 \text{ gr/cm}^3$ ) and their related underground models. Observed anomaly is given with solid line and its structure is given with hatched area in the cross-section. For  $\Delta\rho = 2.5 \text{ gr/cm}^3$ , calculated anomaly is shown with ( $\star$ ) symbol. For  $\Delta\rho = 1.8 \text{ gr/cm}^3$ , calculated anomaly is shown with ( $\bullet$ ) symbol. For  $\Delta\rho = 2 \text{ gr/cm}^3$ , calculated anomaly is shown with ( $\square$ ) symbol and its structure is given with dashed line in the cross-section.

**5.3. Real Data 1**

In Figure 4. Godavari Vally, which is used in [1] and [2], is modeled using GA. Depth and the widths of each prismatic piece are 250m and 2.5km respectively. In [1] and [2]  $\Delta\rho$  is used as  $-0.4\text{g/cm}^3$ . Therefore, it is also used the same value for  $\Delta\rho$  to compare the models. The anomaly of the model is very close to the observed one and ME is 0.43 mGal. The lower depth of the model is 1.75 km. The average upper and lower widths are 32.5km and 12.5km respectively.



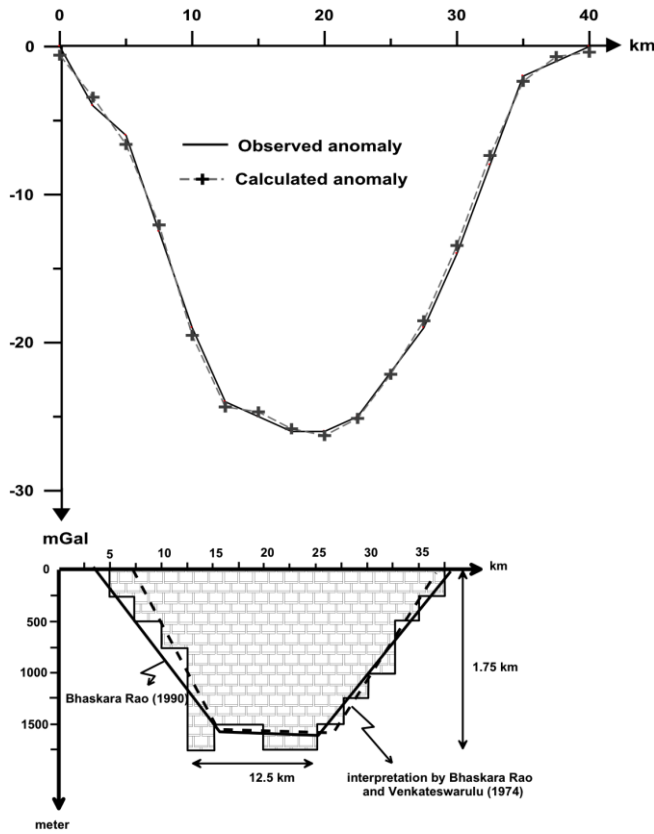


**Figure 4.** Gravity anomaly profile over the lower Godavari Vally and its models. Observed anomaly is shown with solid line. Calculated anomaly using SGA is shown with (+) symbol (width is 2.5km and depth is 250m and  $\Delta\rho = -0.4 \text{ gr/cm}^3$ ). SGA model is given with hatched area. Bhaskara Rao and Venkateswarulu (1974) model is given with dashed lines in cross-section. Bhaskara Rao (1990) model is given with solid line in cross-section.

**5.4. Real Data 2**

As an application field, anomaly map placed at the Northwest side of the mine ore in Sivas-Gürün in Turkey is chosen (Figure 5). It is assumed that the reason of the anomaly can be the basin, which has  $-0.5 \text{ gr/cm}^3$  density difference according to the crystallized limestone. At the end of the studies on this field, it is found out that the oldest units are the limestone the age of Upper Cretaceous Cenomanien. Upper side of this part, Conglomerate at the age of Neogene, red clay and sandstone are placed as a discordant. The region has faults with direction of NE-SW [17].

After two synthetic examples, real data is selected on the Bouguer anomaly map of Sivas basin, which is shown in Figure 6. Anomalies are measured every 50m and  $\Delta\rho$  is known as  $-0.5 \text{ gr/cm}^3$  because of the geology. Low pass filter with a 0.02 cutoff frequency is applied to the anomaly map and this residual anomaly map is shown in Figure 7. Profile A1-A2 in residual anomaly map is considered for modeling with genetic algorithm. The width of the units is 50m. To find more precise result by genetic algorithm, the depth of each unit is taken as 25m. There are 832

individuals in each generation and 416 genes in each individual. The number of worst individuals is chosen as 41 and the ratio of mutation is chosen as 0.3% again.

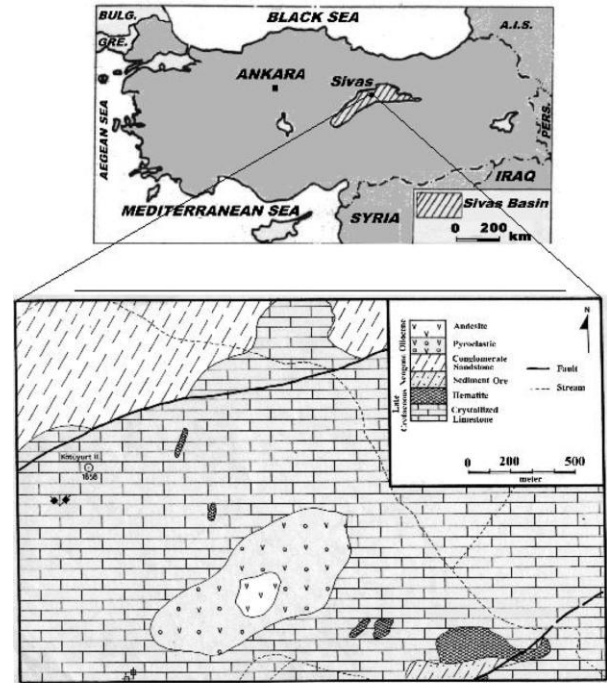


**Figure 5.** Modified geology map of our working region [18].

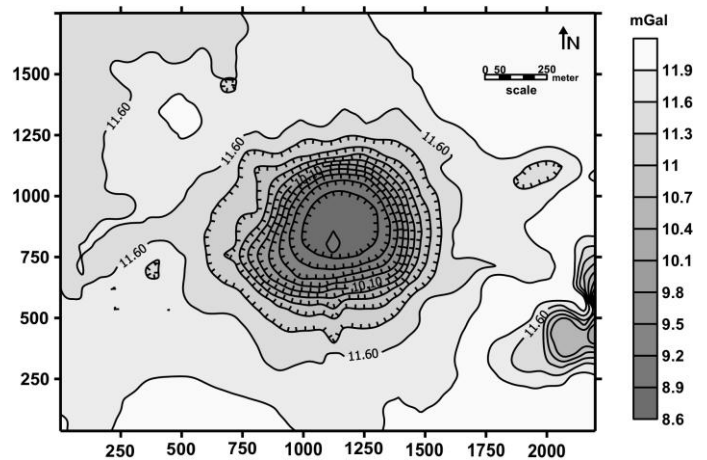


**Figure 6.** Bouguer anomaly map of Sivas-Turkey (interval contour is 0.3 mGal).

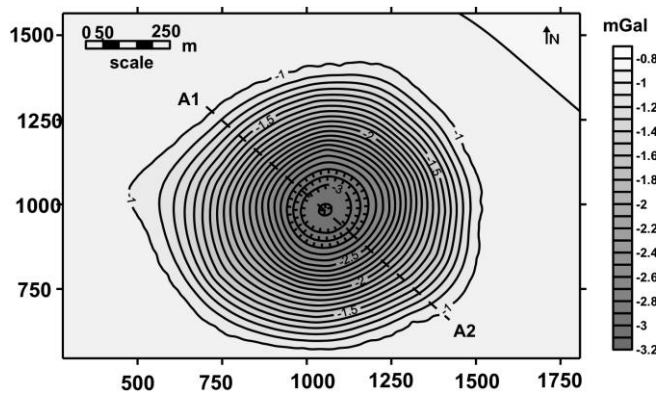


Figure 7. Residual anomaly map (interval contour is 0.1 mGal).

At the end of the 1000<sup>th</sup> generation, the model in Figure 8 is reached and, Its anomaly and observed anomaly are shown. The anomaly of our model and the original anomaly are very close to each other. Mean error of the anomaly of our model is only 0.17 mGal and it fits the original one.

## 6. Conclusion

A new modeling technique using a modified genetic algorithm is very common. This method is quite different and flexible than conventional inversion method. The proposed modeling technique is applied to real anomaly data after having good results with synthetic ones. As a field application, firstly, gravity anomaly of Godavari Vally is used and the model is compared to the references. Secondly, gravity anomaly of carsick basin near Sivas-Gürün in Turkey is considered. Difference of anomaly in the field is computed as  $-0.5 \text{ gr/cm}^3$ . Cross-section, which is taken from A1-A2 profile in Figure 7 Bouguer anomaly map, is indicated with a solid line in Figure 8.

The anomaly of the model, which is created by GA, is shown in Figure 8 with dotted line. Both two anomalies are fit satisfactorily. This modeling technique is so powerful that it can be applied to any type of structure without any prior information.

## 7. Steps of the methods

1. Dividing the cross-section into  $n_r \times n_c$  units
2. Generating an initial population for GA
3. Mapping each individual in the population to the cross-section
4. Setting units to zero whose neighbors are all zero
5. Computing the weight function
6. If the anomaly of any individual is close enough to the desired one then STOP THE PROCESS
7. Sorting individuals (worst individuals are replaced with the best ones)
8. Applying mutation
9. Interleaving the individuals (scrambling)
10. Creating the next generation using crossover technique and GO TO STEP 3.

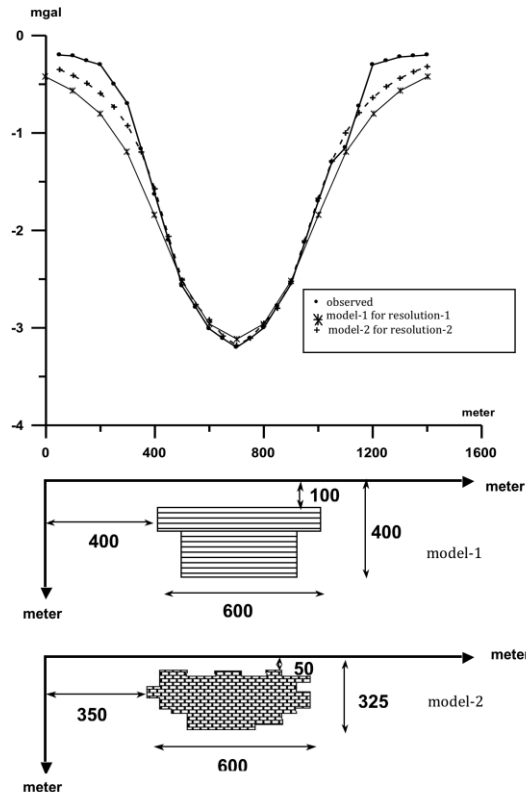


Figure 8. Observed and calculated anomalies and the models. Observed anomaly is shown in (.) and calculated anomalies are shown in (\*) and (+) signs.

## 8. Acknowledgement

This research was supported by Research Institute of Istanbul University (The Project Number: 35156) The authors wish to thank MTA for providing of potential field data for this study.

## 9. References

- [1] Bhaskara Rao, D. (1990), *Analysis Of Gravity Anomalies Of Sedimentary Basins By An Asymmetrical Trapezoidal Model With Quadratic Density Function*. *Geophysics* 55, 226-231.
- [2] Bhaskara Rao, V. And Venkateswarulu, P.D. (1974), *A Simple Method Of Interpreting Gravity Anomalies Over Sedimentary Basins*. [Geophysical Research Letters](#) 12, 177-182.
- [3] Cavicchio, D.J. (1970), *Adaptive Search Using Simulated Evolution*. Ph.D. University Of Michigan.
- [4] Davis, L. (1987), *Genetic Algorithms And Simulated Annealing*. Morgan Kaufmann Publishers, Inc.
- [5] Davis, L. (1991), *Handbook On Genetic Algorithms*. Van Nostrand Reinhold, New York.
- [6] Goldberg, D.E. (1989), *Genetic Algorithms In Search, Optimization, And Machine Learning*. Addison-Wesley Publish Co., Inc.
- [7] Buckles, B.P. And Petry, F.E. (1992), *Genetic Algorithms*. Ieee Computer Society Press Technical Series.
- [8] Wright, A.H. 1991. *Genetic Algorithms For Real Parameteer Optimization*, Presented At The Foundation of Genetic

Algorithms.

- [9] Stoffa, P.L. And Sen, M.K. 1991. *Nonlinear Multiparameter Optimization Using Genetic Algorithms. Inversion Of Plane-Wave Seismograms*, Geophysics 56, 1794-1810.
- [10] Jin, S. And Madariaga, R. (1993), *Background Velocity Inversion With A Genetic Algorithm*. [Geophysical Research Letters](#), 20, 93-969.
- [11] Billing, S., Kennett, B. And Sambridge, M. (1994), *Hypocentre Location: Genetic Algorithms Incorporating Problem Specific Information*, Geophysical Journal International 118, 693-706.
- [12] Boschetti, F., Dentith, M. And List, R. (1995), *A Staged Genetic Algorithm For Tomographic Inversion Of Seismic Refraction Data*, Exploration Geophysics 25, 173-178.
- [13] Boschetti, F. (1995), *Application Of Genetic Algorithms To The Inversion Of Geophysical Data*, Ph.D. Thesis In Mathematical Geophysics, University Of Western Australia.
- [14] Boschetti, F., Dentith, M. And List, R. (1996), *Inversion Of Seismic Refraction Data Using Genetic Algorithms*, Geophysics 61, 1715-1727.
- [15] Ucan, O.N., Bilgili, E. And Albora, A.M. 2002. *Magnetic Anomaly Separation Using Genetic Cellular Neural Networks*, [Journal Of The Balkan Geophysical Society](#) 3, 65-70.
- [16] Hall, J.M. (2004), *Anovel, Real-Valued Genetic Algorithm For Optimizing Radar Absorbing Materials*, Nasa Project No: Nasa/Cr-2004-212669.
- [17] Telford, W.M., Geldart, L.P., Sheriff, R.E. And Keys, D.A. 1981. *Applied Geophysics*. Cambridge University Press, Cambridge.
- [18] Albora, A.M. (1992), *Study Of Gravity Effect Of Different Geometrical Structure With Nomograms*. Istanbul University, Institute Of Science And Technology, Msc. Thesis.



**Onur Osman** was born in Istanbul, Turkey on September, 1973. He graduated from Electrical Engineering Department of Istanbul Technical University in 1994. Then he received M.Sc. degree from Electrical Engineering in 1998. He received Ph.D. degree from Electrical & Electronics Engineering Department of Istanbul University. He is with Istanbul Arel University in Electrical and Electronics Engineering as Assoc. Prof. His research area is channel coding, modulation, MIMO systems, signal processing on EEG and EMG applications, image processing on MR and CT applications, feature extraction and selection, machine learning, classification and clustering.



**Ali Muhittin ALBORA** received the BS, MS and PhD degrees in geophysics engineering from Istanbul University in Istanbul, Turkey, in 1985, 1992 and 1998. He was appointed and assistant professor in 20001, and an associate professor in 2003. since 2003, he has been with Istanbul University, Engineering Faculty department of the Applied Geophysics. His research interests include the the use of potential field methods in the solution of regional and crustal geological problems, and the applications of computer techniques in geophysics.



## TRANSIENT STABILITY SIMULATION OF MULTI-MACHINE POWER SYSTEMS USING SIMULINK

Serdar EKINCI<sup>1</sup> and Aysen DEMIROREN<sup>2</sup>

<sup>1,2</sup>Electrical Engineering Department, Istanbul Technical University, Istanbul, Turkey  
ekinciser@yahoo.com, demiroren@itu.edu.tr

---

**Abstract:** This paper describes a generalized dynamic model of multi-machine power systems for transient stability analysis and its computer simulation using MATLAB/SIMULINK. The generalized model of the power systems can be used for teaching the power system transient phenomena, as well as for research works particularly to improve generator controllers with advanced technologies. Constructional details of various sub-models for the whole power systems are given and their implementation in SIMULINK environment is outlined. The developed simulation model is tested on 3-machine 9-bus power system and 10-machine 39-bus New England power system under different large disturbances. For the studied cases, the critical clearing times (CCT) are calculated and the simulation results are presented and discussed. Nonlinear time-domain simulation results obtained from several case studies validate the effectiveness of proposed model for transient stability analysis. The proposed dynamic model has been employed to support and develop power engineering education at both the undergraduate and graduate levels. Likewise, for academic and educational use, all component sub-models are transparent and can simply be modified or extended.

**Keywords:** Transient stability, multi-machine power systems, MATLAB/SIMULINK, power system modeling, power system simulation..

---

### 1. Introduction

The term "transient stability," in the power system stability studies, mostly denotes the capacity of synchronous machines for remaining in synchronism for the short period of time subsequent to large disturbances, including a fault on transmission facilities, loss of a large load and sudden loss of generation. The system response to such disturbances contains generator rotor angles' large excursions power flows, bus voltages and other system variables. It is worth mentioning that, while steady-state stability is a function only of operating conditions, transient stability is a function of both the operating conditions and the disturbances [1]. This entangles the transient stability analysis noticeably. System nonlinearities, in large disturbances, have a significant role.

To control transient stability or instability subsequent to a large disturbance, or a number of disturbances, time-domain simulation analysis is commonly used to solve the nonlinear equations set explaining the dynamic behavior of system. In that case, conclusion pertaining to stability or instability can be obtained from an inspection of the solution [2-3]. Fault clearing time (FCT) and critical clearing time (CCT) are significant parameters so as to preserve power systems transient stability. The FCT is the time upon which the fault is cleared following the fault occurrence, while the CCT is the fault clearing time

upon which the system is at the critically stable level. If the actual fault clearing time in a system is below the CCT level, the system will be stable [4].

Simulation programs for power system stability analysis can be divided into two classes of tools: commercial software packages and education/research-aimed software packages. Various commercial software packages, such as Power System Simulator for Engineering (PSS/E), Power System Simulator (Simpow), DigSilent, EuroStag, NEPLAN and PowerWorld, are on sale. These programs allow users to access comprehensive component/system, models and computationally efficient algorithms for the analysis. Nevertheless, these programs are not appropriate for educational and research fields because they generally do not provide modification or incorporation of novel component models and algorithms. In education and research fields, flexibility and potential for simple prototyping are much more crucial aspects than its computational efficiency.

This paper discusses the use of SIMULINK software of MATLAB in the dynamic modelling of multi-machine power systems for transient stability simulation. SIMULINK is a software package developed by MathWorks Inc., which is one of the most widely used software in academia and industry for modeling, analysis and simulating dynamical systems. It can be used for modeling linear and nonlinear systems, either in continuous time frame or sampled time frame of even a hybrid of the two. It provides a very easy drag-drop type graphical user



interface to build the models in block diagram form. It has many built-in block library components that you can use to model complex systems. If these built-in models are not enough for you, SIMULINK allows you to have user defined blocks as well. Over the last decade, the topic of power system simulation in MATLAB/SIMULINK has been provided in [5-12]. The use of the MATLAB/SIMULINK for the enhancement of power system component can allow users to take full advantage of dealing with control blocks and power system elements, corroborating new component through comparison of the simulation results for numerous events, and understanding of the basic concepts of power system modeling and simulation.

In this paper, we have developed SIMULINK-based generalized dynamic model and an efficient approach so as to examine the transient stability performance of practical power systems, with SIMULINK as a tool. The aim of the generalized dynamic model is to provide an environment within which students can quickly get started and provides enough modeling flexibility to allow modification or addition of new generator, load, and control system models. Whereas ease of use is mostly important for coursework, the modeling flexibility is useful mostly for research applications. All component sub-models are transparent and can easily be modified or extended. Emphasis has been given to keeping the component sub-models transparent and simple. All component sub-models are designed for use by undergraduate and graduate students in the learning of power system transient stability and for rapid testing of research ideas. The proposed model for transient stability simulation has been applied to different examples of multi-machine power systems such as IEEE 9-bus and IEEE 39-bus power systems. The nonlinear simulation results have been carried out to assess the effectiveness of the developed transient stability simulation model under various large disturbances. We hope that this attempt will add some more practical information in this important and unexhausted domain.

## 2. Multi-machine Power System Model Constructed Using SIMULINK

Regarding transient electromechanical phenomena analysis of a power system, power flow algebraic equations for the transmission network and for the stator windings of the synchronous machines, together with the differential equations for the rotor of the synchronous machines are commonly used. For that reason, the power system mathematical model can be formulated by a set of differential and algebraic equations (DAEs) [13]. In this study, the flux-decay model with static exciter is employed to discuss the synchronous machines.

The whole system is given with regard to SIMULINK blocks in three main single sub-models. One of the most significant characteristics of a model in SIMULINK is its remarkable interactive ability. In

other words, it allows the display of a signal at any point readily available; all one has to do is to add a Scope block or, alternatively, an output port. What's more, giving a feedback signal is as easy as drawing a line. A parameter within any block can be regulated from MATLAB command line or through an *m-file* program. This is a predominantly helpful for multi-machine power system transient stability study because the power system configurations change before, during and after a fault. Loading conditions and control measures can be employed correspondingly.

### 2.1. Differential Equations

The differential equations of the machine and exciter for the  $m$  machine,  $n$  bus system are expressed as follows [13]:

$$\frac{d\delta_i}{dt} = \omega_s \omega_i - 1 \quad i = 1, 2, \dots, m \quad (1)$$

$$\frac{d\omega_i}{dt} = \frac{P_{mi}}{M_i} - \frac{P_{ei}}{M_i} - \frac{D_i(\omega_i - 1)}{M_i} \quad i = 1, 2, \dots, m \quad (2)$$

$$\frac{dE'_{qi}}{dt} = -\frac{E'_{qi}}{T'_{doi}} - \frac{(x'_{di} - x'_{di})i_{di}}{T'_{doi}} + \frac{E_{fdi}}{T'_{doi}} \quad i = 1, 2, \dots, m \quad (3)$$

$$\frac{dE_{fdi}}{dt} = -\frac{E_{fdi}}{T_{Ai}} + \frac{K_{Ai}}{T_{Ai}} V_{refi} - V_i \quad i = 1, 2, \dots, m \quad (4)$$

### 2.2. Stator Algebraic Equations

The stator algebraic equations describe the electrical variables pertaining to the stator windings. The stator algebraic equations are expressed as

$$V_i \sin(\delta_i - \theta_i) - x_{qi} i_{qi} = 0 \quad i = 1, 2, \dots, m \quad (5)$$

$$E'_{qi} - V_i \cos(\delta_i - \theta_i) - x'_{di} i_{di} = 0 \quad i = 1, 2, \dots, m \quad (6)$$

### 2.3. Network Equations

The network equations can be expressed in power-balance or current-balance form. In this study, the current-balance form is employed and the loads are assumed to be of the constant impedance type. In power system with  $m$  generators, the nodal equation can be formulized as:

$$\begin{bmatrix} \bar{I}_1 \\ \vdots \\ \bar{I}_m \\ 0 \\ \vdots \\ 0 \end{bmatrix} = [\bar{Y}'] \begin{bmatrix} \bar{V}_1 \\ \vdots \\ \bar{V}_n \end{bmatrix} \quad (7)$$

$$\bar{I}_i = i_{di} + j i_{qi} e^{j \delta_i - \pi/2} \quad i = 1, 2, \dots, m \quad (8)$$

where  $\bar{I}_1, \dots, \bar{I}_m$  are the complex injected generator currents at the generator buses. Assume that the modified  $\bar{Y}_{bus}$  represented as  $\bar{Y}'$  be divided as

$$[\bar{Y}'] = \begin{matrix} m & n-m \\ \bar{Y}_1 & \bar{Y}_2 \\ n-m & \bar{Y}_3 & \bar{Y}_4 \end{matrix} \quad (9)$$

Inasmuch as there are no injections at buses  $m+1, \dots, n$ , we can leave them out in order to obtain

$$\begin{bmatrix} \bar{I}_1 \\ \vdots \\ \bar{I}_m \end{bmatrix} = \begin{bmatrix} \bar{Y}_R \\ \vdots \\ \bar{V}_m \end{bmatrix} \quad (10)$$

where  $\bar{Y}_R = \bar{Y}_1 - \bar{Y}_2 \bar{Y}_4^{-1} \bar{Y}_3$  is the desired reduced matrix. The reduced matrices for every network condition (before, during and after fault) are computed on account of the power system under study.

### 3. SIMULINK Models

The complete multi-machine power system embodied with regard to SIMULINK blocks in a single integral model by using Eqs. (1)-(10) for transient stability study. The complete system consists of three main sub-models: differential equations sub-model, stator algebraic equations sub-model, and network equations sub-model. The SIMULINK-based general sub-models for computing of differential equations and stator algebraic equations are modeled and are given for all generators in Figure 1 and Figure 2 respectively. We can see in the complete sub-model of Figure 1 that **Scope 1** and **Scope 2** display the individual generator angles and the angular velocities of the all machines, respectively. In Figure 2, **Scope 5** and **Scope 6** monitor electrical power outputs and machine terminal voltages responses respectively, for all generators. It is worth mentioning that in Figure 1 and Figure 2;  $\delta$ ,  $\omega$ ,  $M$ ,  $D$ ,  $E'_q$ ,  $E'_{fd}$ ,  $K_A$ ,  $T_A$ ,  $V$ ,  $V_{ref}$ ,  $P_m$  and  $P_e$  are vector signals having as many rows as the number of generators.

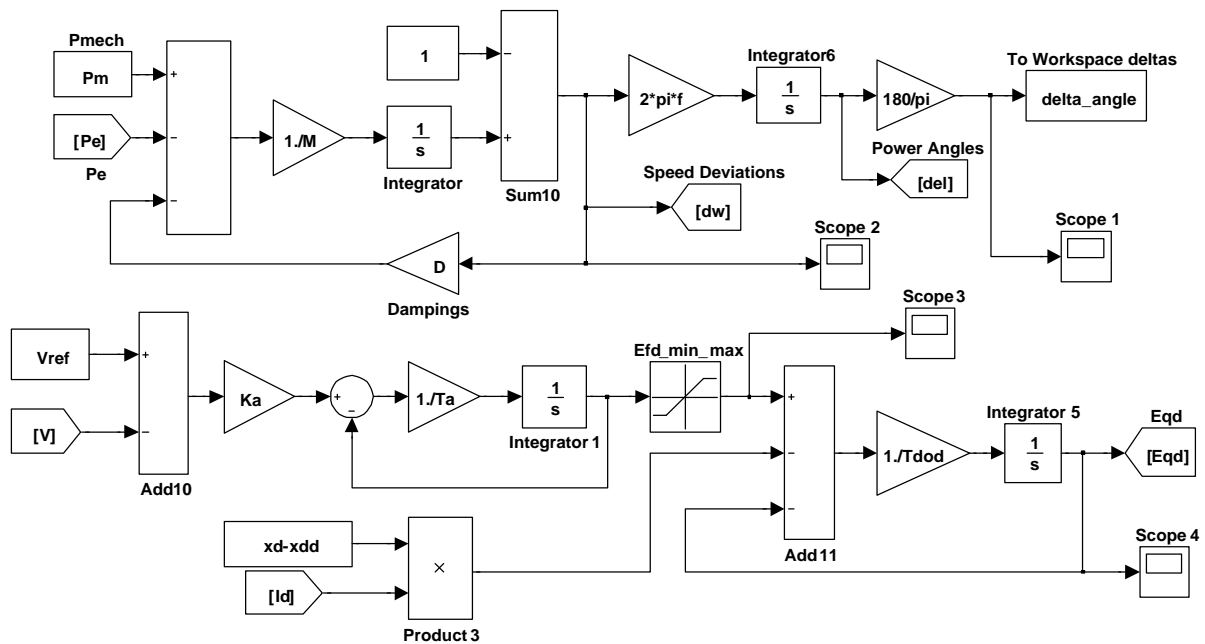


Figure 1. Differential equations sub-model for transient stability simulation

Figure 3 illustrates the complete block diagram of network equations for all generators in SIMULINK environment. The **SUBSYSTEM** in Figure 3 is expressed to calculate the value of electrical current outputs for different generators and internal view of the **SUBSYSTEM** is given in Figure 4. In Figure 4 it includes a block to specify network admittance matrices required for numerous conditions of the power transmission network: before, during and after a specified fault. These admittance matrices are calculated by using an associated MATLAB program prior to starting transient stability simulations of multi-machine power systems, and fault location can be randomly specified.

Likewise, prior to starting transient stability simulations, it is mandatory to specify the initial conditions of a number of quantities for all machines, consequently, a power flow calculation is performed by using the same associated MATLAB program, in which the pre-fault and the fault clearing time are specified. The main SIMULINK-based sub-models are simply modified for multi-machine power systems with different number of generators and also different network configurations. In addition, the generalized dynamic model of multi-machine power systems in SIMULINK environment also facilitates the choice of simulation parameters, including start and stop times, types of solver, step sizes, tolerance and output options.



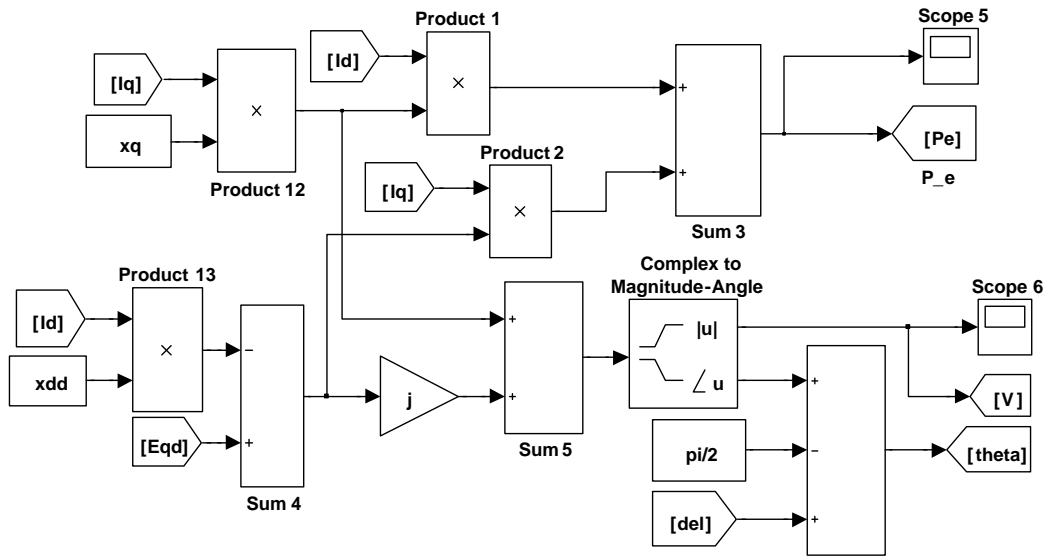


Figure 2. Stator algebraic equations sub-model for transient stability simulation

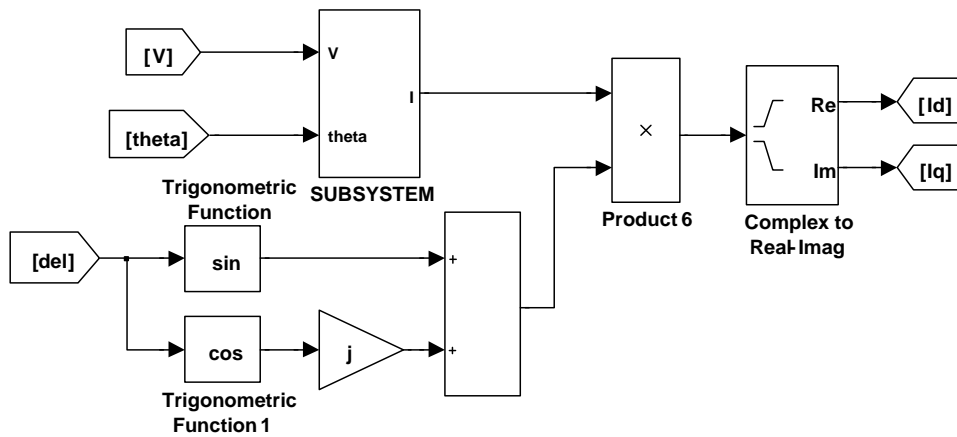


Figure 3. Network equations sub-model for transient stability simulation

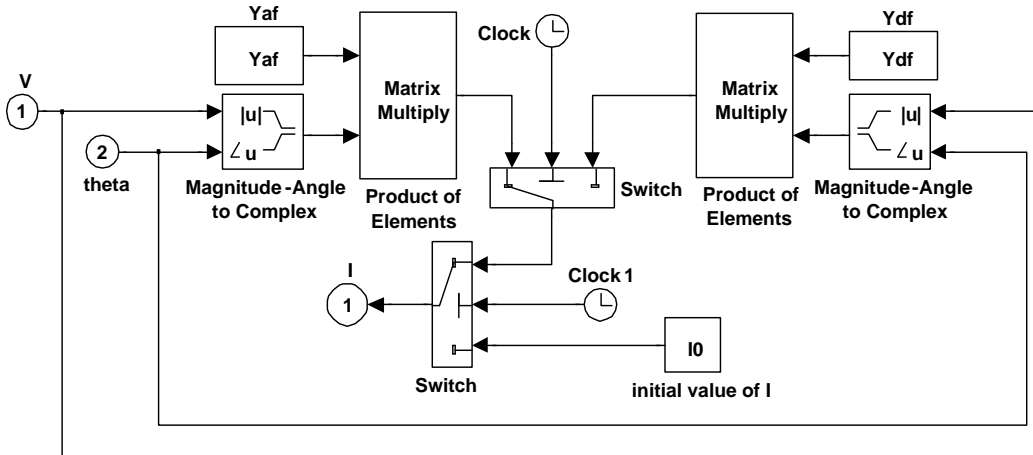


Figure 4. Internal view of the *SUBSYSTEM*.

## 4. Results of Transient Stability Simulations and Discussions

In this section, we illustrate the DAE model discussed in the previous section and to validate SIMULINK-based generalized model, the simulations are carried out on a 3-machine 9-bus and 10-machine 39-bus New England power systems. To assess the effectiveness of the proposed dynamic model, nonlinear time-domain simulation studies are implemented on different severe fault conditions. In transient stability simulation of multi-machine power systems, Runge-Kutta 4 technique is used for

numerical integration of the differential equations and step of integration is chosen as 0.005 s. All calculations were done on a personal computer with 2.10 GHz Intel Core Processor and 2.00 GB of RAM running MATLAB/SIMULINK 7.11.0.

### 4.1. Illustrative System example 1: Nine-bus three-machine power system

In this example, we have considered the popular Western System Coordinated Council (WSCC) 3-machine, 9-bus power system shown in Figure 5. This is also the system appearing in [13-14] and widely used in literature.

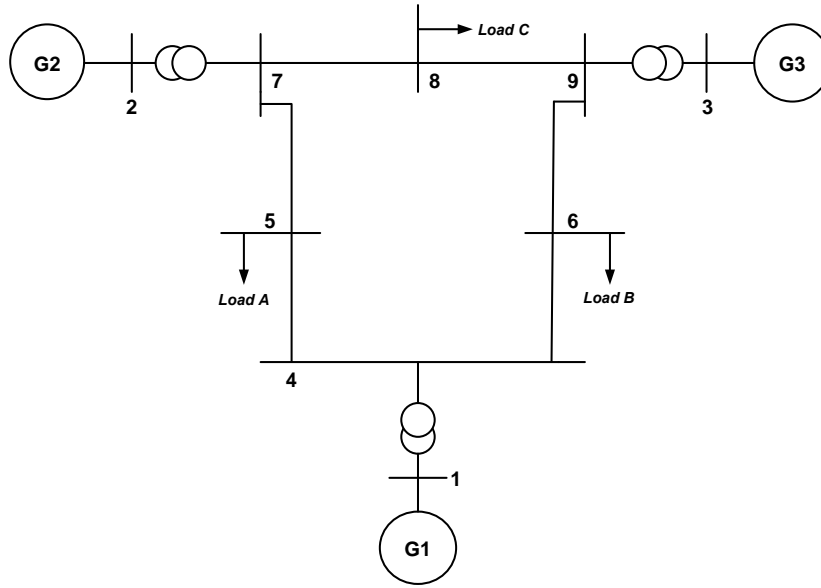


Figure 5. WSCC 3-generator 9-bus test system

We can see in the complete sub-model of Figure 1 that **Scope 1** display the values of the 3-machine angles in vector  $\delta = \delta_1 \ \delta_2 \ \delta_3^T$  and **Scope 2** display the values of the 3-machine angular speeds in vector  $\omega = \omega_1 \ \omega_2 \ \omega_3^T$ . It is worth mentioning that the computation time for 3-machine 9-bus power system 3.28 s for 12 s of simulated real time. For time-domain simulations, different three-phase faults have been applied to demonstrate the effectiveness of the proposed dynamic model as follows:

The performance of the proposed dynamic model under transient conditions is substantiated by applying a three-phase fault at  $t = 1$  s, on bus 9 at the end of line 8-9 is considered. The fault is then cleared by opening the line 8-9. The CCT for this scenario was found to be  $t_{cr} = 0.192$  s by using a trial-and-error approach. The system responses are given for different values of fault clearing time (FCT).

**Case (a):** FCT < CCT, the fault occurs at 1 s and is cleared at 1.15 s (FCT = 0.15 s).

**Case (b):** FCT > CCT, the fault occurs at 1 s and is cleared at 1.20 s (FCT = 0.20 s).

Figures 6-7 show the difference angles ( $\delta_{21} = \delta_2 - \delta_1$  and  $\delta_{31} = \delta_3 - \delta_1$ ) and the relative rotor angular speed deviations ( $\omega_{21} = \omega_2 - \omega_1$  and  $\omega_{31} = \omega_3 - \omega_1$ ), respectively, for the system with FCT = 0.15 s. It is obvious from Figures 6-7 that the power system is stable in Case (a). Figures 8-9 show the system response for FCT = 0.20 s. From the results, we see that the system is unstable in Case (b) because all machines will lose synchronism.

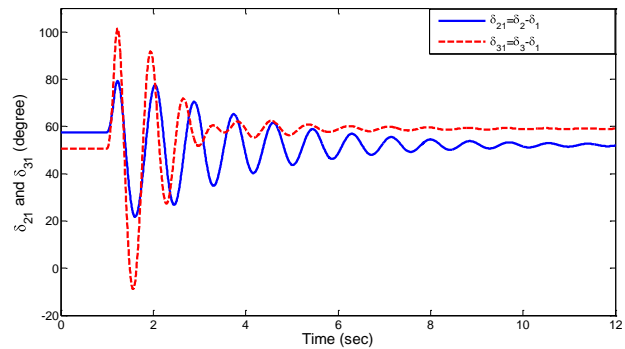
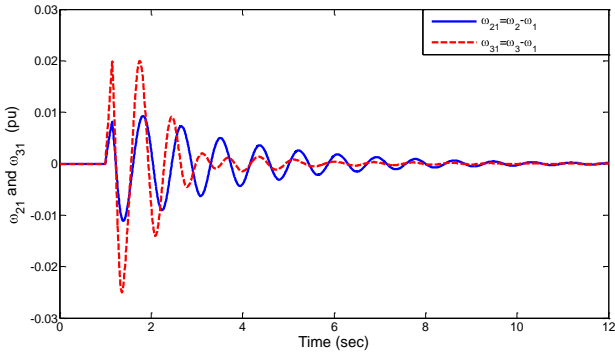
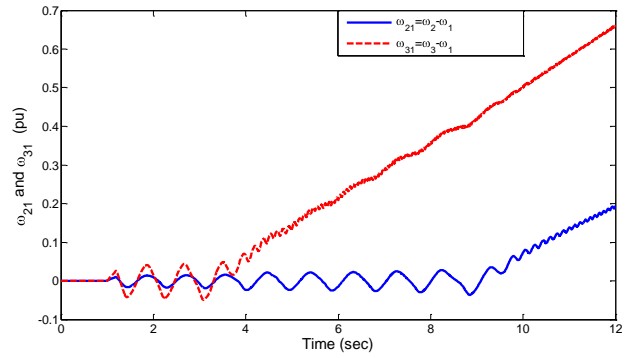


Figure 6. System response of  $\delta_{21} = \delta_2 - \delta_1$  and  $\delta_{31} = \delta_3 - \delta_1$  for FCT = 0.15 s



**Figure 7.** System response of  $\omega_{21} = \omega_2 - \omega_1$  and  $\omega_{31} = \omega_3 - \omega_1$  for FCT = 0.15 s



**Figure 9.** System response of  $\omega_{21} = \omega_2 - \omega_1$  and  $\omega_{31} = \omega_3 - \omega_1$  for FCT = 0.20 s

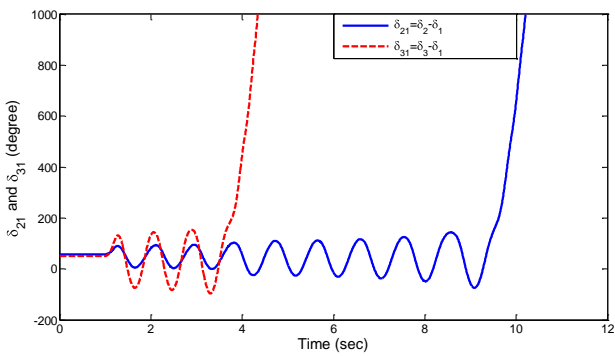


**Figure 8.** System response of  $\delta_{21} = \delta_2 - \delta_1$  and  $\delta_{31} = \delta_3 - \delta_1$  for FCT = 0.20 s

**4.2. Illustrative system example 2: Thirty nine-bus ten-machine power system**

In this part of the study, the 10-machine 39-bus New England power system shown in Figure 10 is considered further demonstrate the versatility of the suggested dynamic model. This is also the system appearing in [15-16] and widely used in the literature.

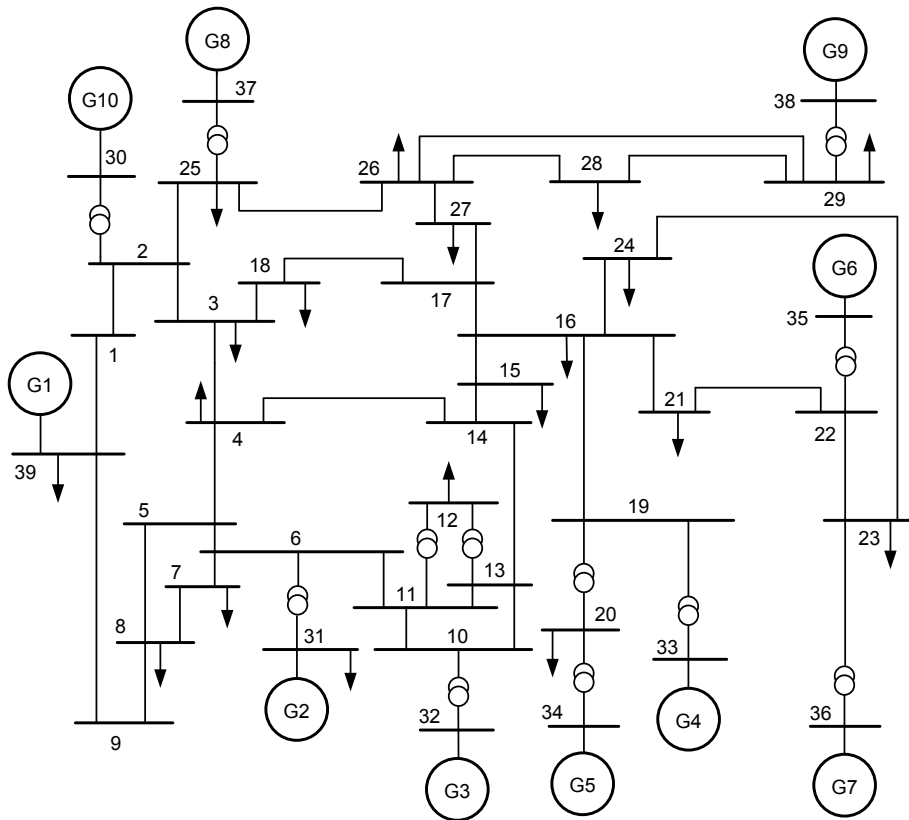


**Figure 10.** 10-machine, 39-bus New England test system

We can see in the complete sub-model of Figure 1 that **Scope 1** display the values of the 10-machine angles in vector  $\delta = \delta_1 \ \delta_2 \ \delta_3 \ \delta_4 \ \delta_5 \ \delta_6 \ \delta_7 \ \delta_8 \ \delta_9 \ \delta_{10}^T$  and **Scope 2** display the values of the 10-machine angular speeds in vector  $\omega = \omega_1 \ \omega_2 \ \omega_3 \ \omega_4 \ \omega_5 \ \omega_6 \ \omega_7 \ \omega_8 \ \omega_9 \ \omega_{10}^T$ . The simulation was performed for 12 s and the computation time for this large power system 13.56 s. To assess the effectiveness of the proposed dynamic model, nonlinear time-domain simulation studies are implemented on different severe fault conditions. The following cases are taken into consideration:

A three-phase fault is applied on bus 29 (near generator 9) at the end of line 29-26 at  $t = 1$  s. The fault cleared without line tripping and the original system is restored upon the clearance of the fault. The CCT for this scenario was found to be  $t_{cr} = 0.125$  s by using a trial-and-error approach. The system responses are given for Case (a) and Case (b).

**Case (a):**  $FCT < CCT$ , the fault was initiated at 1 s and cleared at 1.10 s ( $FCT = 0.10$  s).

**Case (b):**  $FCT > CCT$ , the fault was initiated at 1 s and cleared at 1.13 s ( $FCT = 0.13$  s).

In this scenario,  $G_8$  and  $G_9$  are nearest generators to the fault location and therefore system responses are given for only these machines. For Case (a) and Case (b), the power system angle responses of  $G_8$  and  $G_9$  with respect to  $G_1$ , ( $\delta_{81} = \delta_8 - \delta_1$  and  $\delta_{91} = \delta_9 - \delta_1$ ), are shown in Figure 11 and Figure 13, and the variations of the relative speed deviation of  $G_8$  and  $G_9$  with respect to  $G_1$ , ( $\omega_{81} = \omega_8 - \omega_1$  and  $\omega_{91} = \omega_9 - \omega_1$ ), are shown in Figure 12 and Figure 14. In Figures 11-12, the FCT is set at 0.10 s while in Figures 13-14 the FCT is set at 0.13 s. Figure 11 shows that the relative rotor angles of the *Generator 8* and *Generator 9* oscillate and the system is said to be stable whereas Figure 13 shows that the relative rotor angle of the *Generator 9* go out of step after a fault is cleared and the systems becomes unstable.

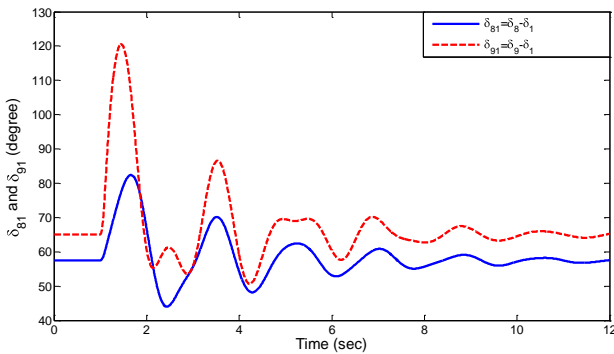


**Figure 11.** System response of  $\delta_{81} = \delta_8 - \delta_1$  and  $\delta_{91} = \delta_9 - \delta_1$  for  $FCT = 0.10$  s

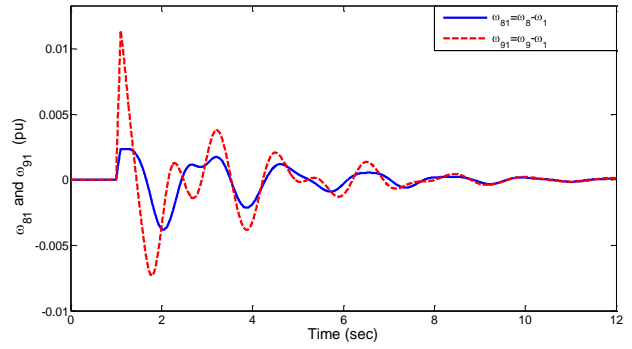


**Figure 12.** System response of  $\omega_{81} = \omega_8 - \omega_1$  and  $\omega_{91} = \omega_9 - \omega_1$  for  $FCT = 0.10$  s

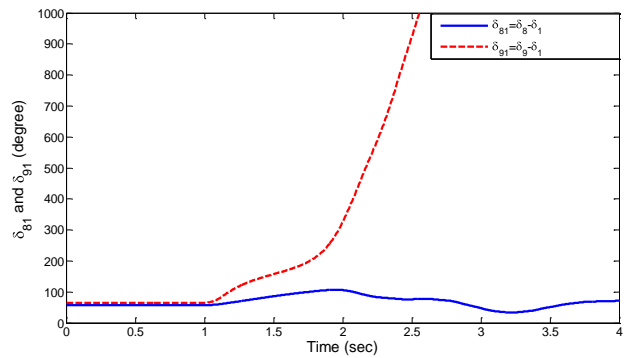


**Figure 13.** System response of  $\delta_{81} = \delta_8 - \delta_1$  and  $\delta_{91} = \delta_9 - \delta_1$  for  $FCT = 0.13$  s

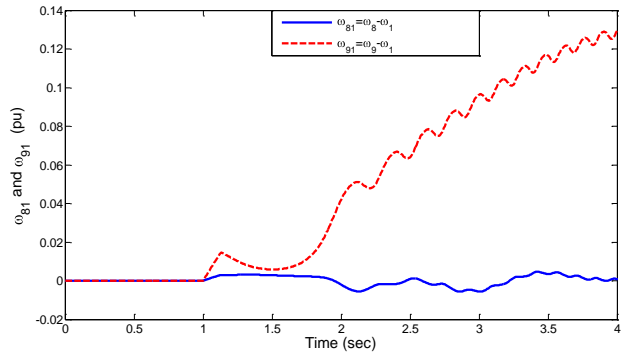


**Figure 14.** System response of  $\omega_{81} = \omega_8 - \omega_1$  and  $\omega_{91} = \omega_9 - \omega_1$  for  $FCT = 0.13$  s

The effectiveness of the suggested dynamic model in multi-machine power systems is verified through the nonlinear simulation results. In addition, it can be deduced from Figures 6-9 and Figures 11-14 that the FCT setting is a significant factor to determine the power systems transient stability. If the FCT is set at a longer time than the CCT of the faulted line, the system will be unstable; otherwise the system will be stable.

### 5. Conclusion

SIMULINK is a powerful software package for the study of dynamic and nonlinear systems. Using SIMULINK, the simulation model can be built up

systematically starting from simple sub-models. A self-sufficient generalized dynamic model for transient stability simulation of multi-machine power systems has been given with full details, which can work as a basic structure for advanced and detailed studies. The models built in this way are easy to be understood by students and engineers. The proposed dynamic model has an open structure and all sub-models can be modified or extended using various SIMULINK constructs. The efficiency of the proposed MATLAB/SIMULINK-based transient simulation model has been tested and demonstrated through the transient stability simulations under various disturbance conditions and different fault clearing times, by using the three and ten machine study systems. Several cases have been also carried out to determine the effect of the clearing time of a fault on the transient stability of multi-machine power systems.

The proposed dynamic model shows to be a powerful didactic and research tool, able to provide important information about various aspects of transient stability phenomena. This educational model is also used for illustration purposes during lectures, as well as by students preparing personal assignments and design projects. The authors believe that SIMULINK will soon become an indispensable tool for the teaching and research of power systems.

## 6. References

- [1] Kundur P., Power system stability and control, New York, USA: Mc Graw-Hill, 1994.
- [2] Bettiol A. L., Souza A., Todesco J. L., Tesch JR Jr., "Estimation of critical clearing times using neural networks", In: IEEE Power Tech Conference Proceedings; 23-26 June 2003; Bologna, Italy: IEEE. pp. 1-6.
- [3] Karami A., Esmaili S.Z., "Transient stability assessment of power systems described with detailed models using neural networks", *Int J Electr Power Energy Syst*, Vol. 45, No. 1, pp. 279-29, 2013.
- [4] Ahmed M.A. Haidar, M.W. Mustafa, Faisal A.F. Ibrahim, Ibrahim A. Ahmed., "Transient stability evaluation of electrical power system using generalized regression neural networks", *Applied Soft Computing*, Vol. 11, No. 4, pp. 3558-3570, 2011.
- [5] Ong C., Dynamic Simulation of Electric Machinery Using MATLAB/SIMULINK. Upper Saddle River, NJ: Prentice Hall, 1998.
- [6] Allen E., White N.L., Yoon Y., Chapman J., Ilic M., "Interactive object-oriented simulation of interconnected power systems using SIMULINK", *IEEE Trans. Educ*, Vol. 44, No. 1, pp. 87-94, 2001.
- [7] Patel R., Bhatti T.S., Kothari D.P., "MATLAB/Simulink-based transient stability analysis of a multi-machine power system", *Int J Elec Eng Educ*, Vol. 39, No. 4, pp. 320-336, 2002.
- [8] Demiroren A., Zeynelgil H.L., "Modelling and Simulation of synchronous machine transient analysis using SIMULINK", *Int J Elec Eng Educ*, Vol. 39, No. 4, pp. 337-346, 2002.
- [9] Cho Y.S., Park J., Jang G., "A novel tool for transient stability analysis of large-scale power systems: Its application to the KEPCO system", *Simul Model Pract Th*, Vol. 15, No. 7, pp. 786-800, 2007.
- [10] Panda S., "Differential evolutionary algorithm for TCSC-based controller design", *Simul Model Pract Th*, Vol. 17, No. 10, pp. 1618-1634, 2009.
- [11] Gelen A., Yalcinoz T., "An educational software package for Thyristor Switched Reactive Power Compensators using Matlab/Simulink", *Simul Model Pract Th*, Vol. 18, No. 3, pp. 366-377, 2010.
- [12] Nguimfack-Ndongmo J.D.D., Kenné G., Kuate-Fochie R., Cheukem A., Fotsin H.B., Lamnabhi-Lagarrigue F., "A simplified nonlinear controller for transient stability enhancement of multi-machine power systems using SSSC device", *Int J Electr Power Energy Syst*, Vol. 54, pp. 650-657, 2014.
- [13] Sauer P.W., Pai M.A., Power system Dynamics and Stability. Prentice Hall, 1998.
- [14] Anderson P.M., Fouad A.A., Power System Control and Stability. Ames, IA: Iowa State Univ. Press, 1977.
- [15] Pai M.A., Energy function analysis for power system stability. USA: Kluwer Academic publishers, 1989.
- [16] Padiyar K.R., Power System Dynamics: Stability and Control. Hyderabad, India: B.S. Publications, 2002.



control technology and the applications of heuristic optimization to power system control.



and alternative power sources, and applications of AI techniques in power systems.

**Serdar Ekinci** received B.Sc. degree from Istanbul Technical University (ITU) Control Engineering Department in 2007. He earned his M.Sc. degree in Electrical Engineering from the same university in 2010. He is currently a Ph.D. student in Istanbul Technical University. His areas of interest are electrical power system, stability, control technology and the applications of heuristic optimization to power system control.

**Aysen Demiroren** received her B.Sc., M.Sc. and Ph.D. degrees from Istanbul Technical University in Electrical Engineering in 1982, 1985 and 1994, respectively. Currently, she is a full professor in Electrical Engineering Department of Istanbul Technical University. Her research interests are power system dynamics, stability and control, power generation and alternative power sources, and applications of AI techniques in power systems.



# COMPACT TRIPLE-BAND BANDPASS FILTER USING MULTI-MODE RESONATOR (MMR) WITH MULTIPLE TRANSMISSION ZEROS

Xuebin TANG and Shuping JIN

Changzhou Institute of Mechatronic Technology, Changzhou, 213164, China.

tang\_xue\_bin@163.com, jinshuping@126.com

**Abstract:** In this article, a compact triple-band microstrip bandpass filter (BPF) with tunable centre frequencies and bandwidths as well as multiple transmission zeros (TZs) is presented. The proposed filter is designed based on a novel multi-mode resonator (MMR), and the even-/odd-mode analysis method is employed to investigate its resonant characteristics. By changing the lengths of two loaded coupled open stubs and coupling space between them, two resonant modes can be tuned and the bandwidth can be controlled. Also, two additional TZs are generated due to the dual-finger feed structure. Moreover, these two TZs can be controlled by the lengths of two fingers, and high passband selectivity and band-to-band isolation level are achieved with ten TZs. The three centre frequencies of the proposed triple-band BPF are located at 1.9, 3.55, and 7.33 GHz, respectively. In addition, the overall circuit size of the fabricated filter is much smaller in comparison with previous works. For demonstration, a prototype filter is fabricated and measured, and good agreements are obtained between the measured results and electromagnetic (EM) simulated ones.

**Keywords:** Bandpass filter (BPF), multi-mode resonator (MMR), transmission zeros, triple-band filter.

## 1. Introduction

In modern wireless communication systems, multi-service technology has been widely and aggressively developed. Thus, as an important circuit block, multi-band planar bandpass filters (BPFs) have gained a lot of attention over past few years. Extensive efforts have been made to design multi-band BPFs, and various literatures about multi-band filters have been reported [1-19]. Quarter-wavelength resonators [1-3] have been employed to construct dual-band or tri-band BPFs. In [4], and [5], tri-section stepped-impedance resonators (SIRs) are utilized to design triple-band filters. However, the insertion losses need to be improved and the circuit sizes are comparatively large. Shorted-ended SIRs [6], [7] have been used to realize dual- and triple-band BPFs, whereas asymmetric SIRs are introduced to design triple-band BPFs with compact size in literatures [8], and [9]. Stub-loaded resonators (SLRs) [10-12] and square ring loaded resonators (SRLRs) [13], [14] are also proved to be capable of designing triple-band filters. Recently, the design method to achieve high performance multi-band BPFs utilizing multi-mode resonators (MMRs) has been attracting much more attention [15-19]. However, there is still much research work to do to design filters with compact circuit size and high skirt selectivity and

band-to-band isolation level with multiple transmission zeros (TZs).

This paper presents a compact triple-band BPF using a novel MMR. The proposed MMR is symmetric in structure, and the even-/odd-mode analysis method is employed to investigate its resonant characteristics. By properly tuning the design parameters, the resonant frequencies can be freely chosen. In addition, by changing the lengths of two loaded coupled open stubs and coupling space between them, two resonant modes can be tuned and the bandwidths can be controlled. Also, two additional TZs are generated due to the dual-finger feed structure and can be controlled by the lengths of two fingers. Thus, high passband selectivity and band-to-band isolation level are obtained with nine TZs. In order to validate the design method, a triple-band filter centred at 1.9/3.55/7.33 GHz with 3-dB fractional bandwidths (FBWs) of 14.2/7.9/11.6% is simulated and fabricated. The simulation works of the prototype filter are performed by using a commercial electromagnetic (EM) simulator IE3D, and the measured results show good agreement with the simulated ones.

## 2. Analysis of the Proposed MMR

Fig. 1(a) shows the specific geometrical schematic of the proposed MMR. It is mainly constructed by a meandered square-loop loaded with a pair of coupled open



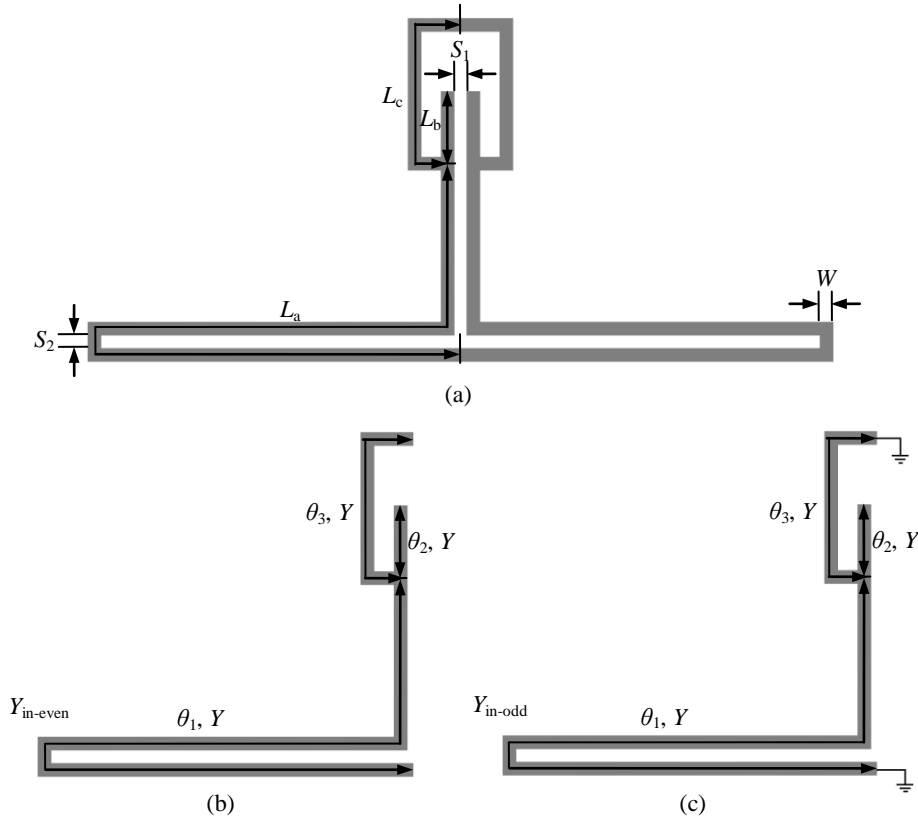


**Fig. 1.** (a) Specific geometrical schematic of the proposed MMR. (b) Even- and (c) odd-mode equivalent circuits.

stubs. Since the proposed MMR is symmetrical in structure, the even-/odd-mode analysis method can be adopted to analyze its resonant characteristics. Its even- and odd-mode equivalent circuits are illustrated in Figs. 1(b) and (c), respectively. The microstrip lines with electrical lengths of  $\theta_1$ ,  $\theta_2$ , and  $\theta_3$  have the same admittance of  $Y$ . Thus, the input admittances of the even- and odd-mode equivalent circuits can be found as follows

$$Y_{in-even} = jY \frac{\tan \theta_1 + \tan \theta_2 + \tan \theta_3}{1 - \tan \theta_1 (\tan \theta_2 + \tan \theta_3)} \quad (1)$$

$$Y_{in-odd} = -jY \frac{\tan \theta_1 + \tan \theta_2 - \cot \theta_3}{\tan \theta_1 (\tan \theta_2 - \cot \theta_3) - 1} \quad (2)$$

The even-mode resonance occurs under the condition of  $Y_{in-even} = 0$ , and the odd-mode resonance occurs when  $Y_{in-odd} = 0$ , that is

$$\tan \theta_1 + \tan \theta_2 + \tan \theta_3 = 0 \quad \text{for even mode} \quad (3)$$

$$\tan \theta_1 + \tan \theta_2 - \cot \theta_3 = 0 \quad \text{for odd mode} \quad (4)$$

From Figs. 1(b), and (c), one can clearly observe that there are four different resonant sections of the proposed MMR, i.e., the sections with lengths of  $L_a + L_b$  and  $L_a + L_c$  in even- and odd-mode equivalent circuits. Therefore, the even- and odd-mode resonant frequencies,  $f_{even1}, f_{even2}, f_{odd1}$ , and  $f_{odd2}$ , generated by the

four resonant sections can be approximately estimated by equations (5) - (8) [8] as

$$f_{even1} \approx \frac{nc}{2(L_a + L_b)\sqrt{\epsilon_{eff}}} \quad n = 1, 2, 3, \dots \quad (5)$$

$$f_{even2} \approx \frac{nc}{2(L_a + L_c)\sqrt{\epsilon_{eff}}} \quad n = 1, 2, 3, \dots \quad (6)$$

$$f_{odd1} \approx \frac{nc}{4(L_a + L_b)\sqrt{\epsilon_{eff}}} \quad n = 1, 3, 5, \dots \quad (7)$$

$$f_{odd2} = f_{even2} \quad (8)$$

where  $f_{even1}$  and  $f_{odd1}$  are the even- and odd-mode resonant frequencies generated by the resonant section with length of  $L_a + L_b$ , and  $f_{even2}$  and  $f_{odd2}$  are the even- and odd-mode resonant frequencies created by the  $L_a + L_c$  section, respectively. The number  $n$  denotes the  $n$ th spurious resonant frequency and

$$\epsilon_{eff} = \frac{\epsilon_r + 1}{2} + \frac{\epsilon_r - 1}{2} \left[ \left( 1 + 12 \frac{h}{w} \right)^{-0.5} + 0.04 \left( 1 - \frac{w}{h} \right)^2 \right] \quad (9)$$

is the effective dielectric constant, where  $\epsilon_r$  and  $h$  denote the relative dielectric constant and thickness of the substrate, respectively. Thus, desired resonant frequencies can be obtained by properly selecting the design parameters according to equations (5) - (8).

Figs. 2(a) and 2(b) depicts the resonant characteristics of the proposed MMR under weak coupling with varied  $L_b$  and  $S_1$ . Fig. 2(a) reveals that  $f_{odd1}$  and  $f_{odd2}$  decrease with the increase of  $L_b$ , whereas  $f_{even1}$ ,  $f_{even2}$ , and  $f_{even3}$  remain constant. This conclusion can also be observed from equations (5) - (8). Moreover, it can be observed from these

two plots that, the second passband formed by  $f_{\text{odd}1}$  and  $f_{\text{even}2}$  can be easily tuned by controlling the coupling strength between the two loaded coupled open stubs which is determined by the value of  $L_b$  and  $S_1$ .

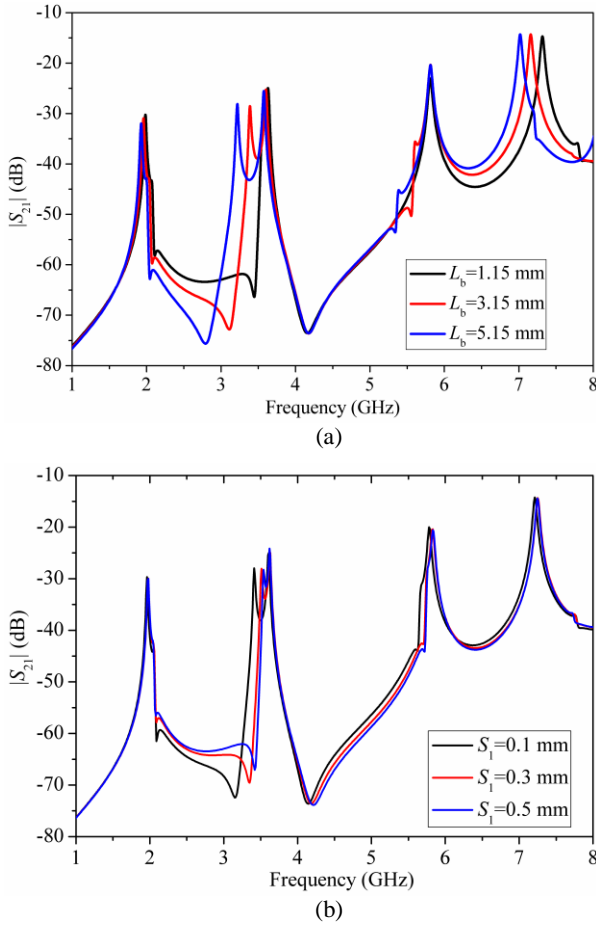


Fig. 2. Simulated  $|S_{21}|$  of the proposed MMR under weak coupling with varied (a)  $L_b$ , and (b)  $S_1$ .

### 3. Analysis of Transmission Zeros

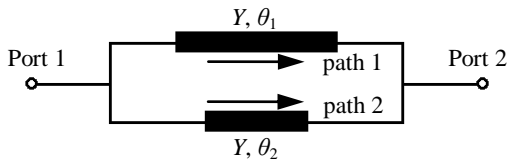


Fig. 3. Transversal signal interference model of the proposed BPF.

As shown in Fig. 5, ten TZs are created in the frequency responses which improve the passband selectivity significantly. Among these TZs,  $TZ_1$  and  $TZ_9$  are inherent TZs of the proposed MMR as can be seen from Fig. 2.  $TZ_4$  and  $TZ_6$  are generated due to the loaded coupled lines. By changing the coupling length and gap between the two open stubs, i.e., the coupling strength between them, these two TZs can be tuned. As demonstrated in Figs. 2(a) and 2(b),  $TZ_4$  and  $TZ_6$  decrease with the increase of  $L_b$  and the decrease of  $S_1$ , i.e., these two TZs decrease with the increase of coupling strength between the two loaded coupled open

stubs. In addition,  $TZ_2$ ,  $TZ_3$ ,  $TZ_7$ , and  $TZ_8$  are introduced by the dual-finger feed scheme. These four TZs decrease with the increase of lengths of the two fingers.

Among these ten TZs,  $TZ_5$  is generated by the transversal signal interference effect [20]. As can be observed from Fig. 4, there are two different transmission paths for signals to transmit from port 1 to port 2, i.e., the upper path 1 and the lower path 2. Its transversal signal interference model is shown in Fig. 3. The characteristic admittance of the two transmission paths are the same as  $Y$ , and electrical lengths of  $\theta_1$  and  $\theta_2$ , respectively. The transmission zeros occur under the following condition:

$$\theta_1 - \theta_2 = (2n + 1) \cdot \pi \quad \text{at } f_{\text{TZ}} \quad n = 0, 1, 2, \dots \quad (10)$$

where  $f_{\text{TZ}}$  denotes the transmission zero frequency. That means the difference between the electrical lengths of two transmission paths equals odd multiple of  $\pi$ . Thus, the phases of the two signals transmit from port 1 to port 2 through path 1 and path 2 are inverted at port 2, which results in out-of-phase cancellation and TZs are generated. In this work,  $TZ_5$  is the case of  $n = 0$ .

### 4. Design Procedure

After the resonant characteristics of the proposed MMR is clear, the triple-band BPF can be designed accordingly. The specific configuration of the proposed triple-band BPF is shown in Fig. 4. This filter is mainly constructed by the proposed MMR discussed in the last section. By meandering the  $L_a$  section in Fig. 1(a) and using a dual-finger feed structure with source-load coupling, the triple-band filter is obtained.

Fig. 5 demonstrates the simulated insertion losses of the proposed triple-band filter with the variation of  $L_9$ . One can clearly observe that the value of  $L_9$  affects coupling strength of the third passband without influencing the first and second passbands. The parameter  $L_9$  is selected as 8.1 mm after EM simulation and optimization (IE3D in this work) to obtained the desired coupling strength of the third passband. Also, the spurious frequencies at about 5.65 and 5.81 GHz are suppressed due to the decrease of the TZ introduced by the finger  $L_8 + L_9$ .

Thus, the design procedure is listed as the following steps. Firstly, the length  $L_a + L_c$  is determined by the centre frequency of the first passband ( $f_1$ ), and its value can be calculated from equation (6). Secondly, the initial length of  $L_b$  can be obtained with reference to equation (7). Then, tune the value of  $L_b$  and  $S_1$  to achieve the desired bandwidth of the second passband. At last, the lengths of two fingers of the dual-finger feed structure, i.e.,  $L_8 + L_9$  and  $L_{10} + L_{11}$ , are tuned to obtain desired coupling strength to form the three passbands, and to generate two TZs at desired frequencies. These two TZs introduced by the two fingers are located at the frequencies where the physical lengths of the corresponding finger is equal to quarter-wavelength.

### 5. Results

In order to demonstrate the validity of the above-mentioned design method, the proposed triple-band BPF is designed and fabricated on a Rogers Duroid 4003 substrate with a thickness of 0.508 mm, a dielectric

constant  $\epsilon_r$  of 3.55, and a loss tangent of 0.0027. The layout of designed filter is shown in Fig. 3. The

simulation works are carried out by the full-wave EM

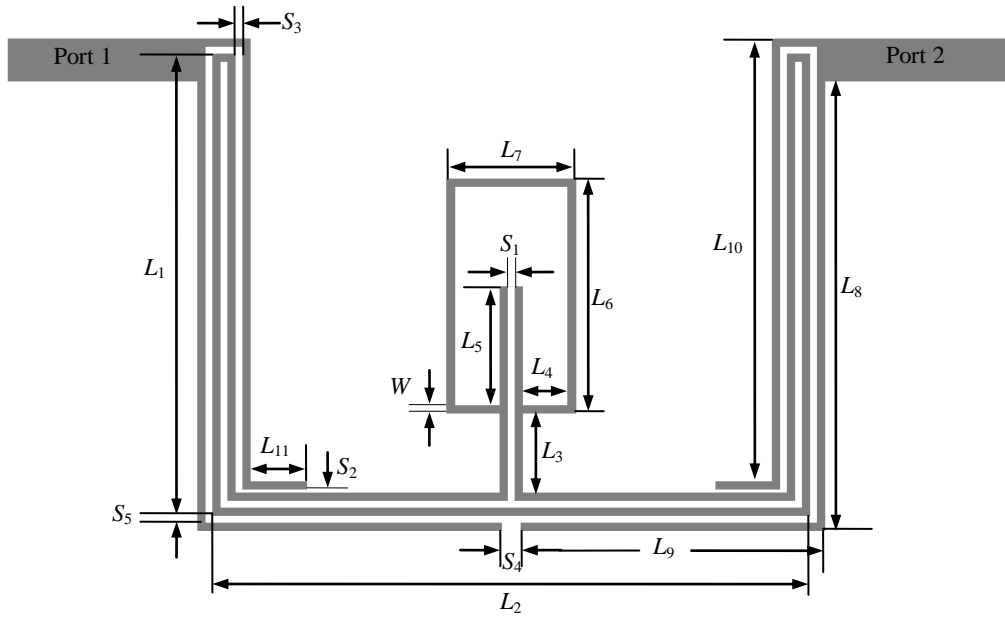


**Fig. 4.** Specific configuration of the proposed triple-band BPF. ( $W = 0.2$  mm,  $L_1 = 12.2$  mm,  $L_2 = 15.8$  mm,  $L_3 = 2.1$  mm,  $L_4 = 1.2$  mm,  $L_5 = 2.1$  mm,  $L_6 = 6.2$  mm,  $L_7 = 3.4$  mm,  $L_8 = 11.89$  mm,  $L_9 = 8.1$  mm,  $L_{10} = 11.7$  mm,  $L_{11} = 1.5$  mm,  $S_1 = S_2 = S_5 = 0.1$  mm,  $S_3 = 0.2$  mm,  $S_4 = 0.5$  mm).

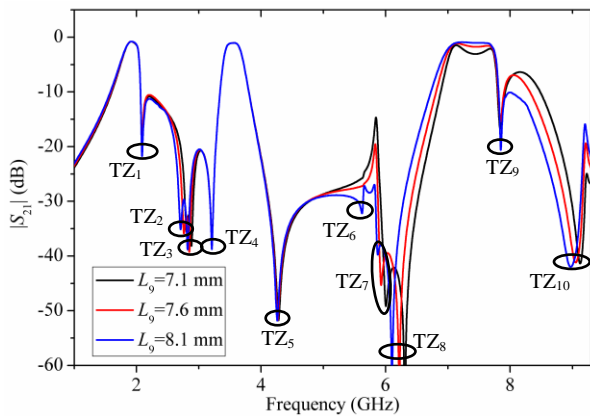


**Fig. 5.** Simulated  $|S_{21}|$  of the proposed triple-band BPF with varied  $L_9$ .

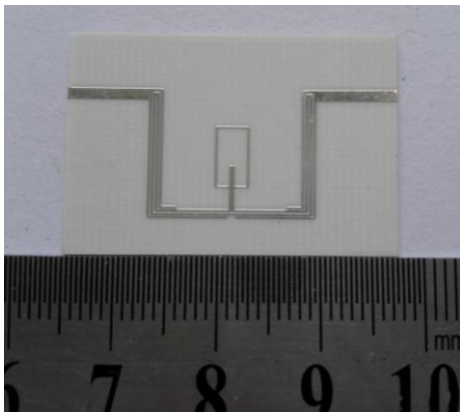


**Fig. 6.** Photograph of the fabricated triple-band filter.

simulator IE3D, and the measurements are performed with an Agilent's N5244A network analyzer.

Based on the design method described above, the structural parameters are obtained as follows:  $W = 0.2$  mm,  $L_1 = 12.2$  mm,  $L_2 = 15.8$  mm,  $L_3 = 2.1$  mm,  $L_4 =$

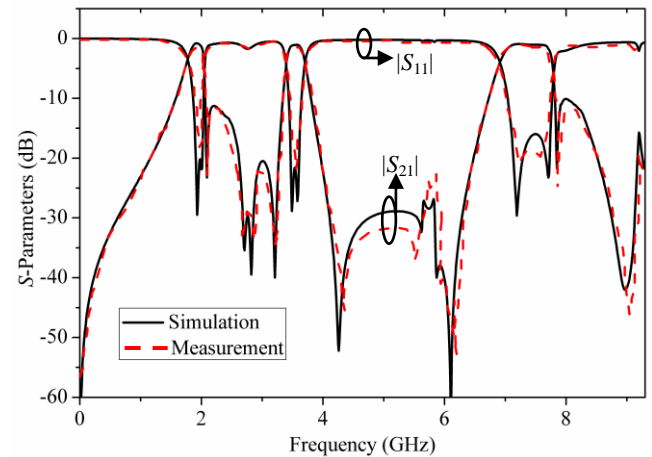


**Fig. 7.** Simulated and measured results of the designed triple-band filter.

$1.2$  mm,  $L_5 = 2.1$  mm,  $L_6 = 6.2$  mm,  $L_7 = 3.4$  mm,  $L_8 = 11.89$  mm,  $L_9 = 8.1$  mm,  $L_{10} = 11.7$  mm,  $L_{11} = 1.5$  mm,  $S_1 = S_2 = S_5 = 0.1$  mm,  $S_3 = 0.2$  mm,  $S_4 = 0.5$  mm. The overall circuit size occupies only  $12.2$  mm  $\times$   $15.8$  mm, i.e., approximately  $0.123 \lambda_g \times 0.159 \lambda_g$ , where  $\lambda_g$  is the guided wavelength at the center frequency of the first passband (1.9 GHz). Obviously, the proposed triple-band BPF is very compact in size.

The photograph of the fabricated prototype triple-band filter is shown in Fig. 6, and Fig. 7 plots the simulated and measured results of fabricated prototype filter. From Fig. 7, it can be observed that the measured and simulated results are in good agreement with each other. The measured center frequencies (CFs) of the fabricated triple-band filter

are 1.9/3.55/7.33 GHz, with the measured 3-dB FBWs of 14.2/7.9/11.6%, the minimum insertion losses (IL:  $|S_{21}|$ ) of 0.86/1.1/1.23 dB and the return losses (RL:  $|S_{11}|$ )

better than 18/20/17 dB, respectively. It is worth mentioning that, ten TZs are generated at about 2.1, 2.63, 2.85, 3.2, 4.4, 5.51,

**Table 1.** Comparison of the proposed filter with other reported triple-band filters.

Refs.	CFs (GHz)	IL (dB)	RL (dB)	FBW (%)	TZ	Circuit Size ( $\lambda_g \times \lambda_g$ )
[2]	1.8/3.5/5.8	0.88/1.33/1.77	21.3/15.8/15.7	7/5/3.5	7	0.108 × 0.521
[4]	1/2.4/3.6	2/1.9/1.7	14/16/20	N/A	0	0.191 × 0.191
[7]	1.57/3.9/7	2/2.1/1.8	22/16/18	4.1/2/3	6	0.113 × 0.145
[9]	2.49/3.6/5.62	1.83/2.95/2.41	12/10/22	9.5/5.3/7.5	3	0.185 × 0.487
[11]	2.45/3.5/5.2	1.2/1.5/1.6	16.3/17.9/12.9	9.6/13.1/7.9	4	0.18 × 0.27
[13]	2.4/3.5/5.2	1.57/1.6/1.77	15/15/20	8.6/7.8/4.9	0	N/A
This work	1.9/3.55/7.33	0.86/1.1/1.23	18/20/17	14.2/7.9/11.6	10	0.123 × 0.159

(TZ denotes the number of transmission zeros.)

5.93, 6.2, 7.8 and 9 GHz, which improve the band-to-band isolation level and passband selectivity significantly. The comparison of the proposed filter with other reported triple-band filters is tabulated in Table 1. It can be observed that, the proposed triple-band BPF exhibits excellent performances of compact size, multiple transmission zeros, high skirt selectivity, low insertion loss, and high band-to-band isolation level.

## 6. Conclusion

In this paper, a compact triple-band microstrip BPF using a novel MMR with multiple TZs is presented. The proposed MMR is analyzed by even-/odd-mode analysis method to investigate its resonant characteristics. Then, a prototype triple-band BPF is designed, fabricated, and measured. Good agreement was obtained between the simulated and measured results. By properly tuning the design parameters, the resonant frequencies can be freely chosen. In addition, by changing the lengths of two loaded coupled open stubs and coupling space between them, two resonant modes can be tuned and the bandwidth of second passband can be controlled. Moreover, ten TZs are generated due to dual-finger feed structure, source-load coupling, transversal signal interference effect, and loaded coupled open stubs, which improves the band-to-band isolation level and passband selectivity greatly. The proposed compact triple-band filter is actually suitable for multi-band and multi-service applications in modern wireless communication systems.

## 7. References

[1] Zhang Songbai and Lei Zhu, "Compact Split-Type Dual-Band Bandpass Filter Based on  $\lambda/4$  Resonators", *IEEE Microw. Wireless Compon. Lett.*, vol. 23, no. 7, pp. 344-346, Jul., 2013.

[2] Songbai Zhang and Lei Zhu, "Compact Tri-Band Bandpass Filter Based on  $\lambda/4$  Resonators With U-Folded

Coupled-Line", *IEEE Microw. Wireless Compon. Lett.*, vol. 23, no. 5, pp. 258-260, May, 2013.

[3] Jun Li, Shanshan Huang, Hui Wang, Yao Li, and Jianzhong Zhao, "A Novel Compact Tri-Band Bandpass Filter Using SIR Embedded Quarter-Wavelength Resonators", *Microw. Opt. Technol. Lett.*, vol. 57, no. 6, pp. 1345-1349, June 2015.

[4] Q. -X. Chu and X. -M. Lin, "Advanced Triple-Band Bandpass Filter Using Tri-Section SIR", *Electron. Lett.*, vol. 44, no. 4, pp. 295-296, Feb., 2008.

[5] F. -C. Chen and Q. -X. Chu, "Compact Triple-Band Bandpass Filter Using Pseudointerdigital Trisection Stepped Impedance Resonators", *Microw. Opt. Technol. Lett.*, vol. 50, no. 9, pp. 2462-2465, Sept., 2008.

[6] Sun S.-J., Su Tao, Deng Kun, Wu Bian, and Liang C.-H., "Shorted-Ended Stepped-Impedance Dual-Resonance Resonator and Its Application to Bandpass Filters", *IEEE Trans. Microw. Theory Tech.*, vol. 61, no. 9, pp. 3209-3215, Sept., 2013.

[7] Jun Li, Shan Shan Huang, Hui Wang, and Jian Zhong Zhao, "Compact Dual-Band Bandpass Filter Using Embedded Center-Grounded SIR and Open-Loop Resonators", *Progr. Electromagn. Res. Lett.*, vol. 49, pp. 9-14, Sep., 2014.

[8] Jun Li, Shan Shan Huang, and Jian Zhong Zhao, "Design of a Compact and High Selectivity Tri-Band Bandpass Filter Using Asymmetric Stepped-Impedance Resonators (SIRs)", *Progr. Electromagn. Res. Lett.*, vol. 44, pp. 81-86, Jan., 2014.

[9] H-W. Wu and R-Y. Yang, "Design of a Triple-Passband Microstrip Bandpass Filter With Compact Size", *J. Electromagn. Waves Appl.*, vol. 24, no. 17-18, pp. 2333-2341, 2010.

[10] Liu, S-K., and F-Z. Zheng, "A New Compact Tri-Band Bandpass Filter Using Step Impedance Resonators With Open Stubs", *J. Electromagn. Waves Appl.*, vol. 26, no. 1, pp. 130-139, 2012.

[11] Chen Wei-Yu, Min-Hang Weng, and Shouu-Jinn Chang, "A New Tri-Band Bandpass Filter Based on Stub-Loaded Step-Impedance Resonator", *IEEE Microw. Wireless Compon. Lett.*, vol. 22, no. 4, pp. 179-181, Apr., 2012.

[12] K. Xu, Y. Zhang, D. Li, Y. Fan, J. L.-W. Li, W. T. Joines, and Q. H. Liu, "Novel Design of a Compact Triple-Band Bandpass Filter Using Short Stub-Loaded SIRs and Embedded SIRs Structure", *Progr. Electromagn. Res.*, vol. 142, pp. 309-320, 2013.

[13] Chen, J-Z., et al, "Fourth-Order Tri-Band Bandpass Filter Using Square Ring Loaded Resonators", *Electron. Lett.*, vol. 47, no. 15, pp. 858-859, 2011.

- [14] Doan M. T., W. Q. Che, and W. J. Feng, "Tri-Band Bandpass Filter Using Square Ring Short Stub Loaded Resonators", *Electron. Lett.*, vol. 48, no. 2, pp. 106-107, 2012.
- [15] S. J. Sun, L. Lin, B. Wu, K. Deng, and C.-H. Liang, "A Novel Quad-Mode Resonator and Its Application to Dual-Band Bandpass Filters", *Progr. Electromagn. Res. Lett.*, vol. 43, pp. 95-104, 2013.
- [16] Xu J., Miao C., Cui L., Ji Y.-X., and Wu W., "Compact High Isolation Quad-Band Bandpass Filter Using Quad-Mode Resonator", *Electron. Lett.*, vol. 48, no. 1, pp. 28-30, 2012.
- [17] Jun Li, Shan Shan Huang, and Jian Zhong Zhao, "Compact Microstrip Dual-Wideband Bandpass Filter Using a Novel Multi-Mode Resonator", *Open Science Journal of Electrical and Electronic Engineering*, to be published, 2014.
- [18] Gao Li, and Xiu Yin Zhang, "High-Selectivity Dual-Band Bandpass Filter Using a Quad-Mode Resonator With Source-Load Coupling", *IEEE Microw. Wireless Compon. Lett.*, vol. 23, no. 9, pp. 474-476, Sept., 2013.
- [19] Jun Li, Shan-Shan Huang, and Jian-Zhong Zhao, "Compact Dual-Wideband Bandpass Filter Using a Novel Penta-Mode Resonator (PMR)", *IEEE Microw. Wireless Compon. Lett.*, vol. 24, no. 10, pp. 668-670, Oct., 2014.
- [20] Gómez-García Roberto, and José I. Alonso, "Design of Sharp-Rejection and Low-Loss Wide-Band Planar Filters Using Signal-Interference Techniques", *IEEE Microw. Wireless Compon. Lett.*, vol. 15, no. 8, pp. 530-532, Aug., 2005.





## ESTIMATION OF PLC CHANNELS: AN ADAPTIVE SIMPLIFIED MAP APPROACH

Selva Muratoğlu ÇÜRÜK<sup>1</sup>

<sup>1</sup>Department of Electrical and Electronics Engineering,  
Iskenderun Technical University, Hatay, Turkey  
smcuruk@mku.edu.tr

**Abstract:** An adaptive channel estimation method, to be used in Power Line Communication systems with Orthogonal Frequency Division Multiplexing modulation, is presented in this paper. The proposed Maximum A-Posteriori based estimator assumes that the channel is frequency selective and slowly time varying and estimates the subchannel correlations adaptively. The performance of the estimator is investigated by evaluating the Mean Square Error of estimations. The simulations are done using measured channel data with additive white Gaussian noise assumption, which show that the proposed estimator has better performance compared to Maximum Likelihood estimation. The performance of the proposed estimator is also analysed under the assumption of colored noise, which is the common case in power lines. The simulations have declared that the performance of the proposed estimator is quite satisfactory, even when the noise is coloured.

**Keywords:** MAP Channel Estimation, Orthogonal Frequency Division Multiplexing, Power Line Communication.

### 1. Introduction

Nowadays Power Line Communication (PLC) is one of the popular topics, which provides a competitive technique for in-home communication applications [1-4]. PLC uses the pre-existing power line network; therefore it does not require any communication specific wiring. Remarkable studies are being carried out in the area of PLC, trying to increase the data rates in preceding systems [5]. Unfortunately, since they are not designed for communication but for power transmission, unstable varying channel characteristics of power line networks is one of the major limiting factors for the data rate of PLC modems that has to compete with alternatives. For communication, though they are wired, power line channels have multipath characteristics (caused by the signal reflection and divergence by the impedance mismatching between the existing branch lines and loads) like the wireless channels [5]. Additionally, the parameters of the multipath channels vary with different network topologies and loads. Moreover, PLC may be impaired by disturbances, such as narrowband interference and additive, white/colored and/or impulsive noise [5]. All these factors increase the degree of complexity of PLC systems.

The well-known multicarrier modulation technique, Orthogonal Frequency Division Multiplexing (OFDM), has been popular for high data rate wireless communication systems. Today, OFDM has also been selected by Home Plug Powerline Alliance as their

power line modulation standard [1-3]. As known, OFDM divides the wide band into many narrower subbands to overcome multipath fading effects and uses orthogonal carriers in transmission for bandwidth efficiency. Unfortunately, significant variations in time and frequency characteristics of power lines may drastically reduce the efficiency of OFDM systems. The performance may be improved by using an adaptive structure to adjust the subcarrier parameters to the channel conditions after channel estimation. Additionally, subcarrier orthogonality within an OFDM symbol should be established for perfect synchronization and channel estimation is a part of the synchronization process. Thus, final performance of an OFDM system is highly dependent on the quality of the channel estimation.

Although the number is very limited compared to wireless OFDM systems, channel estimators to be used for OFDM systems in PLCs have also been proposed in the literature [6-19]. For example in [7], two non-adaptive algorithms, namely least squares and transform domain, are proposed, which are applied to estimate frequency response in the pilot signals, when impulsive noise corrupts the signal. In [8], a low computational complexity methodology for transfer function parameter estimation is presented. In [9], authors proposed a systematic technique to analyze the complex impulse response of PLC channel under additive white noise consideration. There are also some adaptive estimation techniques, such as in [10], an adaptive variable step size based on fuzzy inference algorithm is proposed. In [11], a decision directed method by a neural network for



channel estimation in PLCs with impulsive noise is proposed.

In this paper we aim to develop a channel estimator for OFDM systems in PLCs, with acceptable complexity and performance, where there is a need as far as we see. As known, the estimators are mainly grouped as Maximum Likelihood (ML) based or Maximum A-Posteriori (MAP) based techniques. Typically, in OFDM systems subchannel coefficients are highly correlated. Therefore, the ML estimates will have a higher Mean Square Error (MSE) especially for low Signal to Noise Ratios (SNR), since the ML-based estimators ignore the correlation between subchannels, and the MAP based estimation techniques will perform better: However, in practical systems, a priori channel information will not be available at design stage. Further, because of time varying characteristics of subchannels, as in PLCs, an adaptive MAP estimator which estimates the channel covariance matrix dynamically is needed. Therefore, we have adapted the simplified MAP estimator given in [20], which yields the wireless channel estimates using a parametric correlation model with white noise assumption, for PLC channels. We aim to widen the work done for the wireless channels to the PLCs. We have determined the MSE of the estimates to see the resultant performance of the adapted estimator. The performance of the estimator is evaluated under the constraint of white and coloured noise and we have used real world data taken from the literature in the simulations of the PLC channels.

This paper is organized as follows: The power line channels are investigated in section 2. The adaptive simplified MAP estimator is presented in Section 3. Simulation results follow in Section 4. Finally the conclusions are given.

## 2. Power Line Channels

For a typical multipath channel, each path is associated a propagation delay and an attenuation factor, which are usually time varying due to changes in propagation conditions. Then, a multipath fading channel is modeled by a time varying linear filter with impulse response:

$$h(\tau, t) = \sum_{i=1}^{L_p} a_i \delta(\tau - \tau_i) \quad (1)$$

where  $\delta(\cdot)$  stands for Dirac's delta function,  $L_p$  is total number of paths, time varying  $a_i$  and  $\tau_i$  are the path attenuation and propagation delay of the  $i$ -th path, respectively. The frequency response of the multipath channel is found to be

$$H(f, t) = \sum_{i=1}^{L_p} a_i e^{-j2\pi f \tau_i} \quad (2)$$

For high frequency signals that carry data, PLC channels have frequency selective and time varying behavior which depends on the network topology and wire type. The time variations are caused by the connection/disconnection of electrical devices to the network and by the nonlinear behavior of some electrical devices with respect to the mains voltage. The measurements and studies done have shown that a PLC channel may be modeled as a multipath channel whose frequency response is given by [21]

$$H(f, t) = \sum_{i=1}^{L_p} g_{i,t} e^{-(a_0+a_1 f^k) d_i} e^{-j2\pi f (d_i/v_p)} \quad (3)$$

where  $g_{i,t}$  is the time dependent weighting factor of  $i$ -th path.  $e^{-(a_0+a_1 f^k) d_i}$  is the attenuation portion ( $a_0$  and  $a_1$  are attenuation parameters,  $k$  is the exponent of the attenuation factor,  $d_i$  is the length of  $i$ -th path) and  $e^{-j2\pi f (d_i/v_p)}$  is the delay portion ( $v_p$  is the propagation velocity).

We have chosen three different PLC channel models taken from the literature: The first channel, CH1, is a 4-path multipath which is suitable for PLC channels with 1-4 branch network topology and short distance in the range of 100-200m [21]. The attenuation parameters are  $a_0 = 0$ ,  $a_1 = 7.8 \cdot 10^{-10}$ ,  $k=1$ , and the propagation velocity  $v_p = 1.5 \cdot 10^8$ . CH2 is again for short distance channels with an 8-path multipath, but with different attenuation parameters:  $a_0 = 0$ ,  $a_1 = 1 \cdot 10^{-7}$ ,  $k = 0.6$  [6]. CH3 has 15 path, and is a model for networks longer than 300m, with a more complicated network topology [7]. The parameters are  $a_0 = 0$ ,  $a_1 = 7.8 \cdot 10^{-10}$ ,  $k=1$ , and  $v_p = 1.5 \cdot 10^8$ . Channel parameters, path weighting factor  $g_{i,t}$  and path length  $d_i$ , for CH1, CH2 and CH3 are listed in Table 1, Table 2 and Table 3, respectively.

**Table 1.** Channel I (CH1) Parameters

Path no	1	2	3	4
$g_{i,t}$	0.64	0.38	- 0.15	0.05
$d_i$ (M)	200	222.4	244.8	267.5

**Table 2.** Channel II (CH2) Parameters

Path no	1	2	3	4
$g_{i,t}$	0.6	0.11	- 0.12	0.11
$d_i$ (M)	15	22	28	35
Path no	5	6	7	8
$g_{i,t}$	0.07	- 0.07	0.06	- 0.01
$d_i$ (M)	41	48	53	59

**Table 3.** Channel III (CH3) Parameters

Path no	<b>1</b>	<b>2</b>	<b>3</b>	<b>4</b>	<b>5</b>
$g_{i,t}$	0.029	0.043	0.103	-0.058	-0.045
$d_i$ (M)	75	85	94.2	119.2	123.3
Path no	<b>6</b>	<b>7</b>	<b>8</b>	<b>9</b>	<b>10</b>
$g_{i,t}$	-0.040	0.038	-0.038	0.071	-0.035
$d_i$ (M)	166.7	216.7	268.3	342.5	408.3
Path no	<b>11</b>	<b>12</b>	<b>13</b>	<b>14</b>	<b>15</b>
$g_{i,t}$	0.065	-0.055	0.042	-0.059	0.049
$d_i$ (M)	472.5	616.7	800	941.7	1041.7

For a PLC channel, different noise sources may be considered which are basically grouped in two: The first group is background noise (a combination of colored background noise, narrowband noise and periodic impulsive noise asynchronous to the mains frequency), which remains stationary over periods of seconds or minutes [22]. The second group is called as impulsive noise (a combination of periodic impulsive noise synchronous to the mains frequency and asynchronous impulsive noise) and is time variant in terms of microseconds to milliseconds.

In a communication system, usually background noise limits the channel capacity. The additive background noise in a PLC system has a Power Spectral Density (PSD) which decreases as the frequency increases (colored noise), but the noise is almost white for a frequency higher than 15 MHz [14]. Considering 0-30 MHz band in simulations, the assumption of colored noise will be more realistic. An additive colored noise model obtained from the measurements has a PSD [22]

$$A(f) = b_0 + b_1 |f|^{b_2} \text{ dBm/Hz}, \tag{4}$$

where  $b_0$ ,  $b_1$  and  $b_2$  are parameters depending on measurement locations and  $f$  is the frequency in MHz.

The time domain impulsive noise is modelled well with Middleton's Class-A noise model. In an OFDM system, this noise is randomized via the FFT operation, thus impulsive noise is spread over all carrier frequencies [23]. In [24], the authors show that FFT results with Gaussian distributed noise if the input noise has a Nakagami-m distribution. [25] gives a detailed characteristic of frequency domain narrowband disturbance noise, whose amplitude is normally distributed for high frequencies. In our simulations, we used a simplified noise model, assuming the impulsive noise to be also Gaussian in frequency domain. Thus, there exists an additive colored Gaussian noise only, the background noise, which models all the noise sources.

### 3. Adaptive Channel Estimator

Assuming that the channel is frequency selective for the whole band, but flat for subbands and the channel is stationary inside the observation interval, for an OFDM system with  $N$  subcarriers, after removing the modulation effects the received  $N \times 1$  vector  $\mathbf{r}$  is:

$$\mathbf{r} = \mathbf{z} + \mathbf{n}, \tag{5}$$

where the additive noise  $\mathbf{n}$  and the channel coefficients  $\mathbf{z}$  are  $N \times 1$  vectors, and are samples from zero mean jointly Gaussian complex random processes with  $N \times N$  covariance matrices  $\mathbf{C}_n$  and  $\mathbf{C}_z$ , respectively. The MAP estimation of the channel is [20]:

$$\hat{\mathbf{z}}_{\text{MAP}} = \mathbf{A} \cdot \mathbf{r} \quad \text{where} \quad \mathbf{A} = \mathbf{C}_z \cdot (\mathbf{C}_n + \mathbf{C}_z)^{-1}. \tag{6}$$

The MSE matrix for the MAP estimates is given by [20]:

$$\begin{aligned} \text{MSE}_{\text{MAP}} &= \mathbf{A} \mathbf{C}_n \mathbf{A}^H + (\mathbf{I}_N - \mathbf{C}_z (\mathbf{C}_n + \mathbf{C}_z)^{-1}) (\mathbf{I}_N - \mathbf{C}_z (\mathbf{C}_n + \mathbf{C}_z)^{-1})^H \\ &= \mathbf{C}_z - \mathbf{C}_z (\mathbf{C}_n + \mathbf{C}_z)^{-1} \mathbf{C}_z \end{aligned}, \tag{7}$$

where  $\mathbf{I}_N$  is the  $N \times N$  identity matrix and  $(\cdot)^H$  means Hermitian of the matrix. Note that, under the constraint of white noise (noise samples are mutually independent,  $\mathbf{C}_n = \sigma_n^2 \mathbf{I}_N$ , where  $\sigma_n^2$  is white noise variance), Eqn (7) simplifies to  $\text{MSE}_{\text{MAP}} = \sigma_n^2 \mathbf{A}$ .

Without a priori knowledge of the channel, i.e. the Maximum Likelihood (ML) estimation,  $\mathbf{A}$  will be the identity matrix. Then the ML estimate and its MSE are [20]

$$\hat{\mathbf{z}}_{\text{ML}} = \mathbf{r}, \tag{8}$$

$$\text{MSE}_{\text{ML}} = \mathbf{C}_n. \tag{9}$$

The simplified MAP (SMAP) estimator proposed in [20] assumes that the channel power delay profile is exponential. Then, the correlation between subchannels is given by

$$C_z(l, k) = \frac{1}{1 + j 2\pi\tau_c(l-k)}, \tag{10}$$

where  $l$  and  $k$  are subchannel indices and  $\tau_c = \tau_{rms}/T_s$  is the rms delay spread of the channel relative to the OFDM symbol duration  $T_s$ . For flat fading  $\tau_c$  is zero, and as the channel gets closer to independent fading  $\tau_c$  goes to infinity. The estimates obtained from the SMAP estimator are given by [20]:

$$\hat{\mathbf{z}}_{\text{SMAP}} = \mathbf{A}(\hat{\tau}_c) \mathbf{r}, \tag{11}$$

where  $\mathbf{A}(\hat{\tau}_c) = \mathbf{C}_z(\hat{\tau}_c) (\mathbf{C}_n + \mathbf{C}_z(\hat{\tau}_c))^{-1}$  and  $\hat{\tau}_c$  is an estimate of the parameter  $\tau_c$ . Thus,  $\tau_c$  is estimated and fed

to the MAP estimator for calculating the covariance matrix  $\mathbf{C}_z$  and the matrix  $\mathbf{A}$ . Accordingly, the block diagram of the estimator becomes as shown in Figure 1.

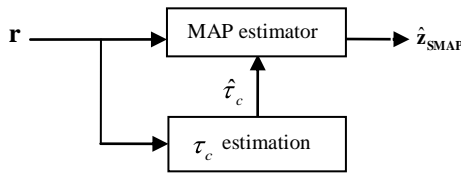


Figure 1. Block diagram of SMAP estimator

$\hat{\tau}_c$  is obtained from the neighbor subband frequency response correlation. For the PLC channels, there are sudden changes in the amplitude and phase in some frequencies; thus subchannel correlation may differ dramatically. In this paper, to be more robust, we propose to use the correlation between 1, 2 and 3 neighbor subchannels, instead of only one. i.e.,

$$\mathbf{C}_z \langle 2 \rangle = \frac{r_1 \cdot r_2^* + r_2 \cdot r_3^* + \dots + r_{N-1} \cdot r_N^*}{|r_2|^2 + |r_3|^2 + \dots + |r_N|^2} \quad (12)$$

$$\mathbf{C}_z \langle 3 \rangle = \frac{r_1 \cdot r_3^* + r_2 \cdot r_4^* + \dots + r_{N-2} \cdot r_N^*}{|r_3|^2 + |r_4|^2 + \dots + |r_N|^2} \quad (13)$$

$$\mathbf{C}_z \langle 4 \rangle = \frac{r_1 \cdot r_4^* + r_2 \cdot r_5^* + \dots + r_{N-3} \cdot r_N^*}{|r_4|^2 + |r_5|^2 + \dots + |r_N|^2} \quad (14)$$

Briefly, we find three different estimates of  $\tau_c$  using Eqn Eqn (12), Eqn (13), Eqn (14) and Eqn (10) and take the arithmetic average in calculating the final estimate. Following, an alpha tracker is used as in [20] for averaging in time to overcome the variations in  $\hat{\tau}_c$  from symbol to symbol. Then

$$\hat{\tau}_c^i = \alpha \cdot \hat{\tau}_c^{i-1} + (1 - \alpha) \hat{\tau}_c^i, \quad (15)$$

where  $i$  is the symbol number and the tracking parameter  $\alpha$  is in the range (0,1).  $\alpha$  should be chosen according to time varying characteristics of the channel. Thus, high  $\alpha$  value yields less noisy estimates, but needs more time for setup.

### 4. Simulation Results

HomePlug AV standard [1] states that OFDM with 1155 subcarrier is used as modulation scheme in the band 1.8 to 30 MHz. For the simulations, taking the standard as reference, the band is chosen as 0-30 MHz (elementary period  $T$  is  $1/30 \mu s$ ) and the subcarrier number,  $N$ , is 1200 (25 kHz subbands).

Figure 2a, Figure 2b and Figure 2c depict multipath characteristics of PLC channels given, namely CH1, CH2 and CH3, respectively. The amplitudes and

phases are determined from the samples taken from the amplitude and the phase spectra of the channels. i.e.

$$\alpha_k = |H \langle k/NT \rangle| \text{ and } \phi_k = \arg \{ H \langle k/NT \rangle \}, \quad (16)$$

where  $k$  is the subchannel indices and elementary period  $T$ . As seen from the figures, the frequency selectivity is lowest for CH2. For CH1 amplitude attenuation exists that rapidly increases with frequency. Note that for CH3, there are sudden changes in the multipath characteristics in 0-200 subbands (0-5 MHz), which is more serious in 0-100 subbands (0-2.5 MHz band).

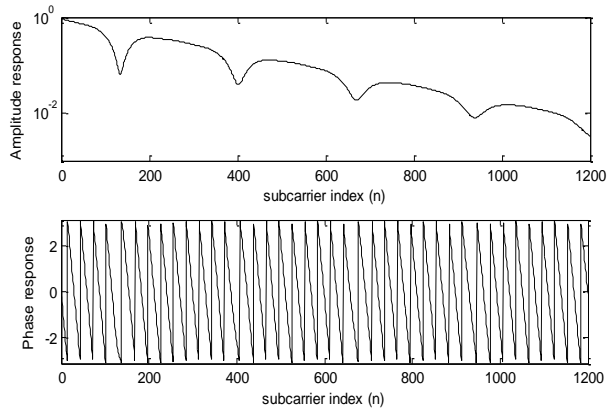


Figure 2a. Amplitude and phase response of CH1 versus subcarrier index.

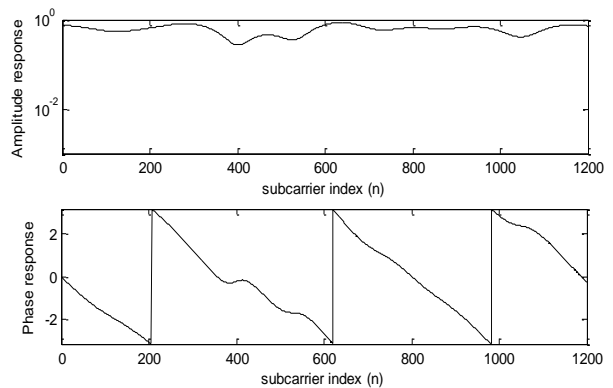


Figure 2b. Amplitude and phase response of CH2 versus subcarrier index

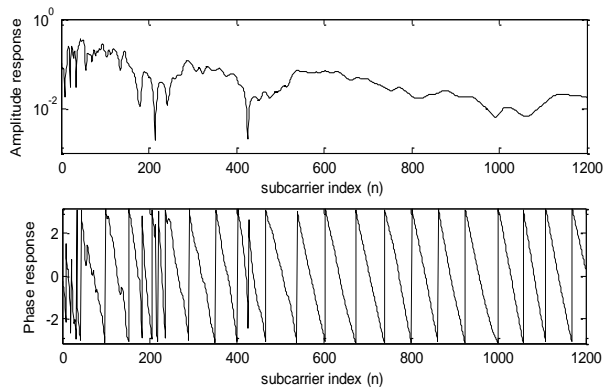
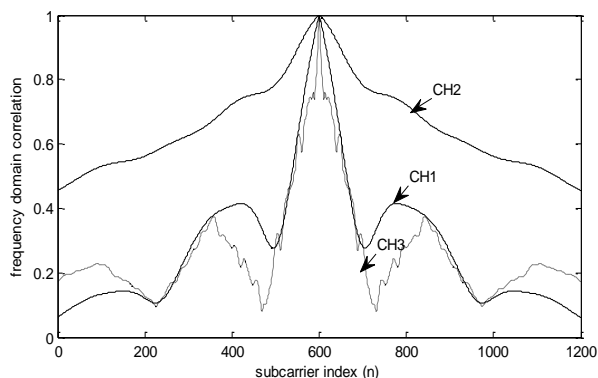


Figure 2c. Amplitude and phase response of CH3 versus subcarrier index.

We have used autocorrelation method in estimating correlation matrix of the channels given. Figure 3 gives the frequency domain correlation of the middle subchannel with the other subchannels for the given PLC channels. As seen, although all channels are somehow correlated, CH2 has the highest correlation between the subchannels.



**Figure 3.** Frequency domain correlation, middle subchannel ( $n=600$ ) with others versus subcarrier index,  $N=1200$ , CH1, CH2, CH3.

Assuming the channels are stationary in the observation period and the noise is additive white Gaussian, simulation results of rms error versus subchannel number for CH1, CH2 and CH3 are given in Figure 4a, Figure 4b and Figure 4c, respectively. Simulation parameters are selected to be SNR=10 dB,  $N=1200$ , and  $\alpha=0.9$ . The given simulation results are the mean of 1000 runs. The estimated values of  $\tau_c$  are found to be 43.55, 3.75, and 34.58 for the channels CH1, CH2, and CH3, respectively. The subchannels of CH2 have higher correlation, while CH1 and CH3 subchannel correlations are close. This result is found to be in good agreement with Figure 3. The dashed lines are used for showing the rms error of the MAP estimator with the computed covariance matrix using autocorrelation method. As seen from the figures, MSE of the proposed estimator is very low compared to ML estimator and nearly the same with the performance of MAP estimator with computed covariance. But for CH3, there is degradation in the estimation performance, for lower bands (1-100 subband, or equivalently 0-2.5 MHz). This seems to be because of the lower correlation between the subbands in this low band. Since this low band is not used in HomePlug AV standard, this degradation will not affect the system performance.

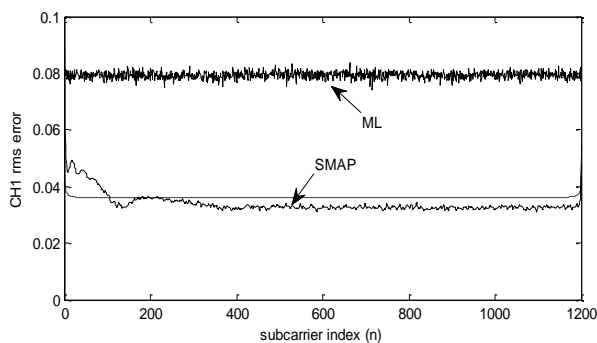


**Figure 4a.** SMAP channel estimator rms error versus subcarrier index, SNR=10 dB, CH1, white noise.

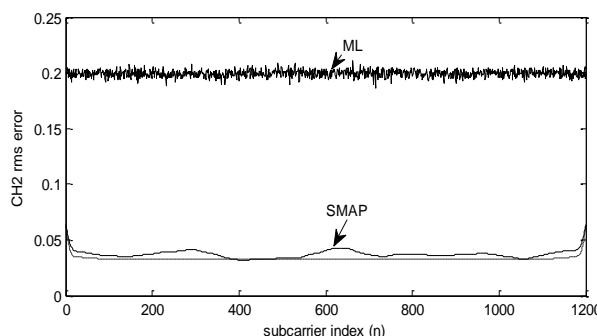


**Figure 4b.** SMAP channel estimator rms error versus subcarrier index, SNR=10 dB, CH2, white noise.

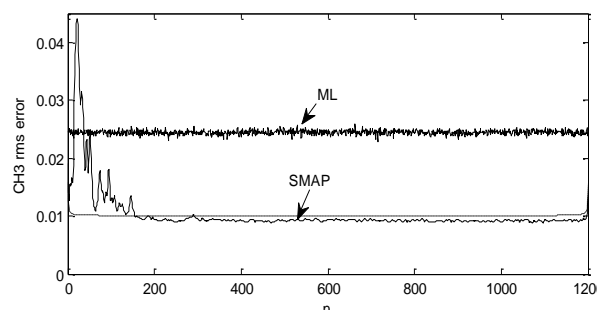


**Figure 4c.** SMAP channel estimator rms error versus subcarrier index, SNR=10 dB, CH3, white noise.

The performance of the proposed estimator is also analyzed under the assumption of colored noise, whose PSD is given in (4) with parameter values  $b_0 = -140$ ,  $b_1 = 38.75$  and  $b_2 = -0.72$ . Simulation parameters are selected to be SNR=10 dB,  $N=1200$ ,  $\alpha=0.9$  and 1000 runs. The estimated values of  $\tau_c$  are found to be 41.07, 3.51, and 32.24 (very close to the white noise corruption case) for CH1, CH2, and CH3, respectively. Simulation results of rms error versus subchannel index for CH1, CH2 and CH3 are given in Figure 5a, Figure 5b and Figure 5c, respectively. As seen, the performance of the proposed estimator is very low compared to ML estimator under the constraint of colored noise for all channels, as in white noise case.

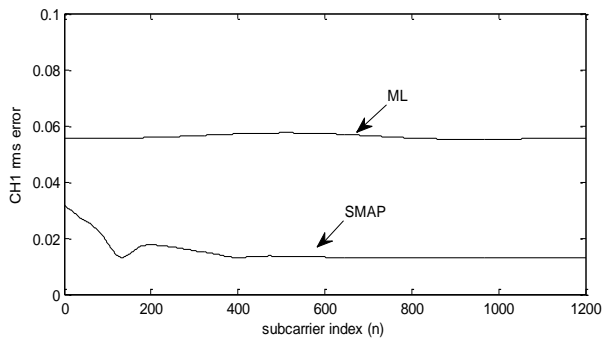


**Figure 5a.** SMAP channel estimator rms error versus subcarrier index, SNR=10 dB, CH1, colored noise.

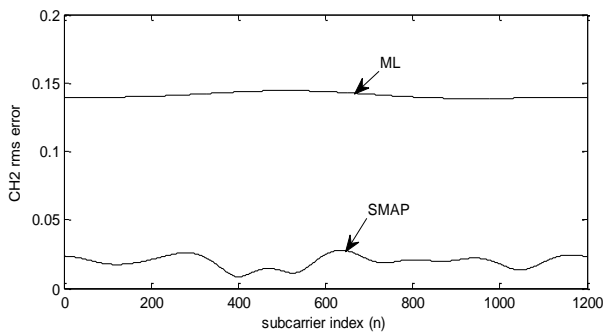


**Figure 5b.** SMAP channel estimator rms error versus subcarrier index, SNR=10 dB, CH2, colored noise.

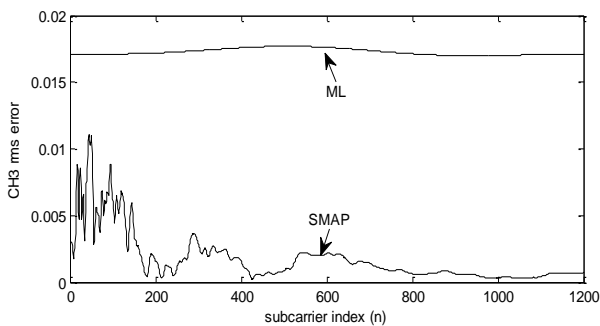


**Figure 5c.** SMAP channel estimator rms error versus subcarrier index, SNR=10 dB, CH3, colored noise.

## 5. Conclusions

We have applied an adaptive simplified MAP channel estimator, which was proposed for wireless OFDM systems with white noise assumption, to PLC systems with white and colored noise. The simplified MAP estimator first estimates the subchannel correlation and then feeds it to the MAP estimator block, where it is used in obtaining the covariance matrix. The simulations showed that the performance of the proposed estimator with additive white Gaussian noise is always better than the ML estimator's, which is the expected, because MAP based estimators outperform when the subcarrier channel taps are correlated. Finally, it is shown that the proposed channel estimator may safely be used when the

corrupted noise is colored, since it has a quite good performance under this circumstance.

## 6. References

- [1] HomePlug Powerline Alliance Inc., "HomePlug AV White Paper", [Online] Available: [http://www.homeplug.org/tech/whitepapers/HPAV-White-Paper\\_050818.pdf](http://www.homeplug.org/tech/whitepapers/HPAV-White-Paper_050818.pdf), 2005.
- [2] HomePlug Powerline Alliance, Inc., "HomePlug AV2 Technology", [Online] Available: [http://www.homeplug.org/tech/whitepapers/HomePlug\\_AV2\\_White\\_Paper\\_v1.0.pdf](http://www.homeplug.org/tech/whitepapers/HomePlug_AV2_White_Paper_v1.0.pdf), 2012.
- [3] HomePlug Powerline Alliance, Inc., "Home Plug Green PHY, The Standard For In-Home Smart Grid Powerline Communications", [Online] Available: [http://www.homeplug.org/tech/whitepapers/HomePlug\\_Green\\_PHY\\_whitepaper\\_100614.pdf](http://www.homeplug.org/tech/whitepapers/HomePlug_Green_PHY_whitepaper_100614.pdf), 2010.
- [4] N. Pavlidou, A.J.H. Vinck, J. Yazdani, B. Honaty, "Power Line Communications: State of the Art and Future Trends", *IEEE Communications Magazine*, Vol: 41, No: 4, pp. 34-40, 2003.
- [5] Information and Communication Technologies (ICT), Seventh Framework Programme: "PLC Channel Characterization and Modelling", Theme 3 ICT-213311 OMEGA, Tech. Rep., v1.2, 2011.
- [6] X. Ding, J. Meng, B.R. Petersen, "Blind Channel Estimation for HomePlug Power-Line Communications: A Feasibility?", *IEEE Transactions on Power Delivery*, Vol: 26, No: 2, pp. 754-763, 2011.
- [7] A.A.M. Picorone, L.R. Amado, M.V. Ribeiro, "Linear and Periodically Time-Varying PLC Channels Estimation in the Presence of Impulsive Noise", *IEEE International Symposium on Power Line Communications and Its Applications*, pp. 255-260, 2010.
- [8] S.R. Mello, M.A. Grivet, "Modeling, Simulation and Estimation of PLC Channels", 2006 *International Telecommunications Symposium*, pp. 201-206, 2006.
- [9] H.M. Oh, S. Choi, Y. Kim, J.J. Lee, K.C. Whang, "A Systematic Approach to Analyzing Multipath Parameters From PLC Channel Response", *IEEE Transactions on Power Delivery*, Vol: 23, No: 4, pp. 1921-1929, 2008.
- [10] Z. Rui, Z. Chao, "Channel Estimation Based on Fuzzy Inference for OFDM System over Low Voltage Power Line", *Power and Energy Engineering Conference*, pp. 1-4, 2010.
- [11] M. Raugi, M. Tucci, "Power Line Communications Channel Estimation and Tracking by a Competitive Neural Network", *IEEE Transactions on Consumer Electronics*, Vol: 52, No: 4, pp. 1213-1219, 2006.
- [12] G.A. Laguna-Sanchez, R. Barron-Fernandez, A. Prieto-Guerrero, "Wavelet-based Improvement for Channel Estimation in a Power-line Communication Environment Impaired by Impulsive Noise", *Electronics, Robotics and Automotive Mechanics Conference*, pp. 523-528, 2010.
- [13] A.M. Tonello, N. Palermo, "Soft Detection with Synchronization and Channel Estimation from Hard Quantized Inputs in Impulsive UWB Power Line Communications", 9th *IEEE International Conference on Ultra-Wideband*, pp. 560-564, 2009.
- [14] D. Bueche, P. Corlay, M. Gazelet, F.X. Coudoux, "A method for Analyzing the Performance of Comb-type Pilot-aided Channel Estimation in Power Line Communications" *IEEE Transactions on Consumer Electronics*, Vol: 54, No: 3, pp. 1074-1081, 2008.
- [15] A. Musolino, M. Raugi, M. Tucci, "Cyclic Short-Time Varying Channel Estimation in OFDM Power-Line Communication", *IEEE Transactions on Power Delivery*, Vol: 23, No: 1, pp. 157-163, 2008.

- [16] Y.H. Kim, "Multipath Parameter Estimation for PLC Channels Using the GEESE Algorithm", IEEE Transactions on Power Delivery, Vol: 25, No: 4, pp. 2339-2345, 2010.
- [17] X. Zhiyuan, M. Yinghong, "A New Adaptive Channel Estimation for Orthogonal Frequency Division Modulation in Power Line Communication", 4th International Conference on Communications, Circuits and Systems, Vol: 1, pp. 389-393, 2006.
- [18] Z. Rui, S. Yingfu, X. Zhengsheng, W. Shun, "Channel Estimation Based on Improved LMS for OFDM System over Low Voltage Power Line", 6th International Forum on Strategic Technology, pp. 911-914, 2011.
- [19] R. Mo, S.W. Oh, Y. Zeng, S.R. Lie, "Channel Estimation for Power Line OFDM Systems with Unknown Colored Noise Exploiting Real Signal Transmission", IEEE International Symposium on Power Line Communications and Its Applications, pp. 149-153, 2009.
- [20] S.M. Çürük, Y. Tanık, "Simplified MAP Estimator for OFDM Systems under Fading", European Transactions on Telecommunications, Vol: 16, No: 4, pp. 357-364, 2010.
- [21] M. Zimmermann, K. Dostert, "A multipath model for the powerline channel", IEEE Transactions on Communication, Vol: 50, No: 4, pp. 553-559, 2002.
- [22] T. Esmailian, F.R. Kschishang, P.G. Gulak, "In-building power lines as high-speed communication channels: channel characterization and a test channel ensemble", International Journal of Communication Systems, Vol: 16, pp. 381-400, 2003.
- [23] Y.H. Ma, P.L. So, E. Gunawan, "Performance analysis of OFDM systems for broadband power line communications under impulsive noise and multipath effects", IEEE Transactions on Power Delivery, Vol: 20, pp. 674- 682, 2005.
- [24] H. Meng, Y.L. Guan, S.X. Chen, "Modeling and analysis of noise effects on broadband power-line communications", IEEE Transactions on Power Delivery, Vol: 20, pp. 630- 637, 2005.
- [25] N. Andreadou, F.N.N. Pavlidou, "Modeling the Noise on the OFDM Power-Line Communications System", IEEE Transactions on Power Delivery, Vol: 25, pp. 150- 157, 2010.



**Selva Muratoğlu ÇÜRÜK** was born in Antakya, Turkey, in 1974. She received B.Sc., M.Sc., and Ph.D. degrees in electrical and electronics engineering from Middle East Technical University (METU), Ankara, Turkey, in 1996, 1999, and 2008, respectively.

She was with Aselsan, Inc., Ankara, Turkey, from 1996 to 2001 as a digital design engineer. Between 2002 and 2008, she worked as a teaching assistant in Electrical and Electronics Engineering Department, METU. Since 2008, she has been with the Electrical and Electronics Engineering Department, Mustafa Kemal University, Hatay, Turkey. Her research interests include wireless communication systems, digital communication theory and digital signal processing.







# PHOTOVOLTAIC BASED SHUNT ACTIVE POWER FILTER USING P-Q THEORY FOR ENHANCING THE POWER QUALITY

R. BALAMURUGAN<sup>1</sup>, R. NITHYA<sup>2</sup>

<sup>1,2</sup>Electrical and Electronics Dept, K.S.Rangasamy College Technology, Tiruchengode, Tamil Nadu, India  
dnrbals@gmail.com, nithibals@gmail.com

---

**Abstract:** This paper proposes a three phase shunt active power filter with photovoltaic array and battery, incorporated with DC-DC boost converter. The filter consists of a three phase voltage source PWM converter with a DC capacitor at the input side. It provides source harmonic reduction with reactive power compensation for loads. The PV array is connected to VSC (Voltage Source Converter) with the help of boost converter in order to maintain the load. The instantaneous  $p-q$  theory based control algorithm is proposed for the shunt active power filter. In this algorithm, the PI controller is used to regulate the DC link capacitor voltage of the converter with respect to the reference value and the reference current calculation is done according to it. The hysteresis PWM current controller gives the switching to the converter. The effectiveness of the proposed system is verified by using the MATLAB/Simulink software.

**Keywords:** Photovoltaic, Shunt Active power filter, Voltage source converter,  $p-q$  theory, Total Harmonic Reduction.

---

## 1. Introduction

Due to the increasing power demand, technology advancement and environmental issues, systems based on renewable energies are rapidly developing nowadays. Recently many of the researches are aimed at using this renewable system to provide power quality at the utility side of the distributed systems [1]. Photovoltaic (PV) cell or solar cell, fuel cell (FC), wind power are major types of renewable energy sources. From the above sources the PV cell and fuel cell are the low DC voltage generating systems. For getting the required voltage PV is the right choice and can be connected in series to get the necessary DC voltage. This generated DC voltage from the PV array is again increased by using the DC/DC converter from low voltage to high voltage, according to the need of application.

The distribution systems are always facing the power quality problem with the intrusion of nonlinear loads. Some of the industrial and commercial loads with non linearity are personal computers, electronic lighting ballasts, variable and adjustable speed drives, electronic house hold appliances, etc. These loads create the power quality problems like harmonics in source current, high neural currents, unbalanced loads and high reactive power compensation, etc. The solution for the above power quality issues are provided by many compensators like shunt active power filter (SAPF), dynamic voltage restorer (DVR) and unified power quality conditioner (UPQC), etc. [2].

Even though all these compensators are well known for its merits, but all suffers by its own drawbacks like usage of high passive elements, increase in size, more losses, slow response, etc. But compared to all the above devices, the SAPF has faster response with full current and voltage compensation. There are different topologies and control techniques of SAPF are available in the literature [3], for mitigating the current harmonics, reactive power compensation and load balancing [4]. Among such, the single phase VSC with instantaneous  $p-q$  theory [5] is most suitable for compensation of current and voltage under harmonics condition.

The objective of this paper is to maintain the DC link voltage of the VSC to provide continuous compensation current and voltage. The main purpose of the PV array is to drive the single switch IGBT (Insulated Gate Bipolar Transistor) boost converter for high voltage to maintain the voltage at DC link side. For continuous compensation, the PV is used as the source for boost converter in day time and battery/ FC in night time. If the compensation is not required or during the excess power of PV, battery is charged. The maximum power point algorithm is not discussed in this paper and the boost converter uses PWM (Pulse Width Modulation) technique for utilizing constant input from source.

## 2. Design of SAPF

The The boost converter fed single phase VSC connected with nonlinear loads at the Point of Common Coupling (PCC) is shown in Figure 1. The single phase

VSC [6] consists of single switch IGBT, inductors, DC link capacitor. The voltage across the DC link capacitor [4], [7] can be calculated by using the formula,

$$V_{dc} = \frac{2\sqrt{2}V_L}{\sqrt{3}} \left( \frac{1}{M_a} \right) \quad (1)$$

Where  $M_a$  is the modulation index and its value is 1,  $V_L$  is the line voltage. The  $V_{dc}$  obtained is 653.197 V for  $V_L = 400$  V and it is chosen as 670 V.

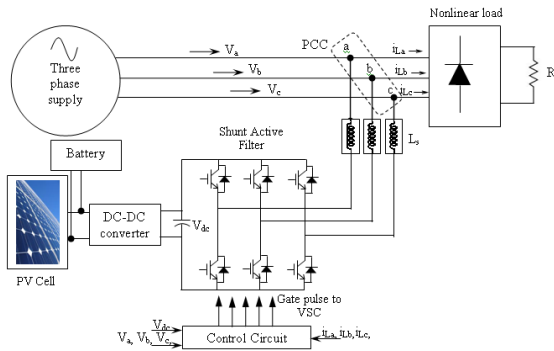


Figure 1. Proposed three phase three wire VSC based on PV

$$C = \frac{6V_{ph}(\alpha I_{ph})T}{V_{ref}^2 - V_{ol}^2} \quad (2)$$

where:  $V_{ref}$  is the reference DC voltage and  $V_{ol}$  the minimum voltage level of DC bus,  $\alpha$  the overloading factor,  $V_{ph}$  the phase voltage,  $I_{ph}$  the phase current, and  $T$  the time by which the DC bus voltage is to be recovered. The value of capacitor is calculated as 2324  $\mu F$  by considering the values for  $V_{ref} = 670$  V,  $V_{ol} = 660$  V,  $V_{ph} = 400/\sqrt{3} = 230.94$  V,  $T = 300$   $\mu s$  and the value of  $I_{ph}$ ,  $\alpha$  is 57.2 A and 1.3 respectively. So the capacitor value is chosen as 2500  $\mu F$ . The VSC is connected to the three phase lines at the PCC through the star/delta transformer. The primary winding voltage of the transformer is selected as 230 V for the line to line voltage of 400 V. The voltage ratio of the transformer is 1:1. The secondary voltage is also chosen like the same primary voltage.

### 3. Modeling of PV

A PV cell is a semiconductor material and it works on the photo voltaic effect. A group of PV cells are connected in series to meet out the required voltage and current [8]. The equivalent circuit of the PV cell is shown in the Figure 3. The voltage produced by PV cell depends on factors like solar irradiation level and temperature with respect to the time to time weather conditions, as it is shown in Figure 2. The Table 1 shown below shows the solar radiation in Tamil Nadu (TN) in the year 2012-2013 and the annual radiation is 5.44  $kWh/m^2$ .

The first page of the manuscript must contain the title of the paper, author(s) name(s) and affiliation(s) all centered on the top of the page and spanning both columns. The title must be written using 14-point Times, boldface type with single spacing. Initially capitalize the title except for articles, coordinate conjunctions, or prepositions. Full names of authors should be given. There must be one-line separation between the title and author name(s), and two-line separation between the authors and their affiliation(s). A one-line separation is needed between the author affiliation(s) and the abstract.

Table 1. Temperature observed in TN during the year 2012-2013

Month	Temperature in ° C		kWh/m <sup>2</sup>
	Max	Min	
Aug-12	34.2	21.3	5.21
Sep-12	34	20.6	4.78
Oct-12	35.2	19.9	4.4
Nov-12	34.3	18.5	4.32
Dec-12	32.4	18.8	4.78
Jan-13	31.3	17.6	5.5
Feb-13	32.5	21.7	6.4
Mar-13	38	23.1	6.76
Apr-13	36.4	19.8	6.83
May-13	35.2	20.15	6.8
Jun-13	35.7	19.83	5.9
Jul-13	36.5	20.75	4.67
Aug-13	34.8	20.3	4.43
<b>Average</b>	<b>34.65</b>	<b>20.17</b>	<b>5.44</b>

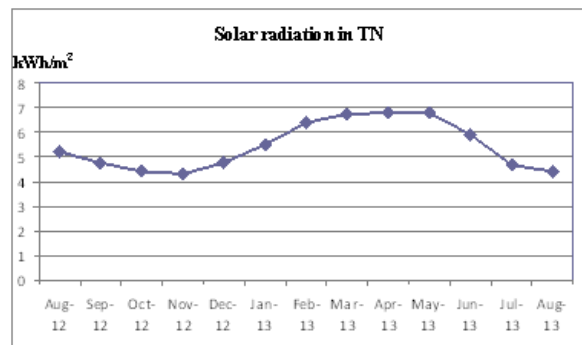
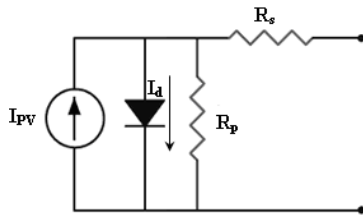


Figure 2. Solar radiation in Tamil Nadu during the year 2012-2013

**Table 2.** Electrical Characteristics of SHARP ND-Q250F7 solar panel

Maximum power (P <sub>max</sub> )*	250W
Tolerance of P <sub>max</sub>	+5%/-0%
Type of the cell	Polycrystalline Silicon
Cell Configuration	60 in Series
Open circuit Voltage(V <sub>oc</sub> )	38.3V
Maximum Power Voltage(V <sub>pm</sub> )	29.8V
Short Circuit Current(I <sub>sc</sub> )	8.90A
Maximum Power Current (I <sub>pm</sub> )	8.4A
Module Efficiency(%)	15.3%
Temperature Coefficient(P <sub>max</sub> )	-0.485%/°C
Temperature Coefficient (V <sub>oc</sub> )	-0.36%/°C
Temperature Coefficient (I <sub>sc</sub> )	0.053%/°C

The PV parameters are taken from the SHARP ND-Q250F7 datasheet which is having the illumination of 1 kW/m<sup>2</sup> solar irradiance at a cell temperature of 25°C. The electrical characteristic of the PV model is given in the Table 2.



**Figure 3.** Equivalent model of PV cell

By applying Kirchoff’s current law to this circuit

$$I = I_{sc} - I_d \tag{3}$$

where:

I<sub>sc</sub> is the short circuit current i.e., equal to the photon generated current

I<sub>d</sub> is the current shunted through intrinsic diode.

The diode current I<sub>d</sub> is given by the Schottky’s diode equation

$$I_d = I_o (e^{qv/KT} - 1) \tag{4}$$

where:

I<sub>o</sub> is the diode saturation current (A)

q is the electron charge [1.602 × 10<sup>-19</sup> C]

k is the Boltzmann constant [1.3806 × 10<sup>-23</sup> J/K]

V is the voltage across the PV cell

T is the junction temperature in kelvin (K)

Combining the equations (3) and (4),

$$I = I_{sc} - I_o (e^{qv/KT} - 1) \tag{5}$$

The reverse saturation current I<sub>o</sub> is constant under constant temperature. Now I = 0 substitute in equation (3) and consider the series resistance R<sub>s</sub> and shunt resistance R<sub>p</sub>, the equation becomes

$$I = I_{sc} - I_o (e^{qv/KT} - 1) - (V + IR_s) / R_p \tag{6}$$

Practical arrays are composed of several connected photovoltaic cells and the observation of the characteristics at the terminals of the photovoltaic array requires the inclusion of additional parameters to the basic equation (3).

$$I = I_{PV} - I_o \left( \exp \left( \frac{V + IR_s}{V_t a} \right) - 1 \right) - ((V + IR_s) / R_p) \tag{7}$$

where:

a is the diode ideality constant

$$V_t = \frac{N_s K T}{q}$$

, is the thermal voltage of array with N<sub>s</sub> cells connected in series.

The equations from (3) to (7) are used to simulate PV model in MATLAB/Simulink.

The proposed PV based VSC operates in three modes viz,

**Mode1:** Compensation by PV in day time, in this mode the voltage from PV arrays operates the single switch boost DC-DC converter fed VSC which compensates the source current as well as charges the battery (48 V).

**Mode2:** Continuous Compensation by PV, in this mode continuous source current compensation is provided by PV based single switch boost DC-DC converter without charging the battery.

**Mode3:** Compensation in night time, in this mode battery / FC supplies the boost converter to provide compensation.

### 4. Control of Single switch boost converter

The single switch boost converter is used to increase the input voltage to get the required output voltage [9]. The PV/battery based boost converter is shown in the Figure 4. The circuit operation can be explained in two modes [10-11]. In mode 1, the input current is charges the inductor L when the switch S is in ON condition upto a period of T<sub>ON</sub> and in mode 2, when S is OFF, the inductor discharges. In this mode 2, the inductor voltage adds with the supply voltage and the current is made to flow through the load via Diode (D) for a period of T<sub>OFF</sub>.

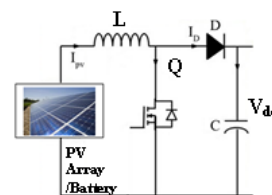


**Figure 4.** Boost converter

The input voltage to boost converter is 48 V and the output voltage obtained is 670 V in order to maintain the DC link voltage of the Shunt active filter. The switching frequency used is 20 kHz and the value of the inductor is chosen as 0.0151 mH. The value of capacitor C is 2500 μF and it is chosen as per the equation (2). The output voltage  $V_o$  equation for the single switch boost converter is given in the equation as follows and it is higher than the input voltage  $V_s$  and it is shown in the equation as,

$$V_o = V_s \left( \frac{T}{T - T_{ON}} \right) \tag{8}$$

$$V_o = V_s \left( \frac{1}{1 - D} \right) \tag{9}$$

$$\text{Duty cycle, } D = \frac{T_{ON}}{T_{ON} + T_{OFF}},$$

$V_o = V_{dc}$ ,  $V_s = V_{in} = PV$  or battery voltage,  
Here

$T_{ON}$  - ON period of boost converter switch,  
 $T_{OFF}$  - OFF period of boost converter switch.

### 5. Control algorithm of SAPF

Many control algorithm available in the literature viz, instantaneous reactive power theory (p – q theory) [5], synchronous reference frame theory, power balance theory etc., for controlling the shunt active filter by generating a reference current. The instantaneous reactive power theory (p – q theory) is found suitable for the control of three phase VSC [12-13] and the control block is shown in the Figure 5.

The system voltages ( $v_{s\alpha}$ ,  $v_{s\beta}$ ,  $v_{s0}$ ) and the load currents ( $i_{L\alpha}$ ,  $i_{L\beta}$ ,  $i_{L0}$ ) are sensed and converted to  $\alpha$ - $\beta$ -0 reference frame by applying the Clarke matrices, shown on equations (10) and (11).

$$\begin{bmatrix} v_{s0} \\ v_{s\alpha} \\ v_{s\beta} \end{bmatrix} = \sqrt{\frac{2}{3}} \begin{bmatrix} \frac{1}{\sqrt{2}} & \frac{1}{\sqrt{2}} & \frac{1}{\sqrt{2}} \\ 1 & -\frac{1}{2} & -\frac{1}{2} \\ 0 & \frac{\sqrt{3}}{2} & -\frac{\sqrt{3}}{2} \end{bmatrix} \begin{bmatrix} v_{sa} \\ v_{sb} \\ v_{sc} \end{bmatrix} \tag{10}$$

$$\begin{bmatrix} i_{L0} \\ i_{L\alpha} \\ i_{L\beta} \end{bmatrix} = \sqrt{\frac{2}{3}} \begin{bmatrix} \frac{1}{\sqrt{2}} & \frac{1}{\sqrt{2}} & \frac{1}{\sqrt{2}} \\ 1 & -\frac{1}{2} & -\frac{1}{2} \\ 0 & \frac{\sqrt{3}}{2} & -\frac{\sqrt{3}}{2} \end{bmatrix} \begin{bmatrix} i_{La} \\ i_{Lb} \\ i_{Lc} \end{bmatrix} \tag{11}$$

After the transformation to  $\alpha$ - $\beta$ -0 reference frame, the p-q theory components are calculated using the equations (12-13),

$$p = v_{s\alpha} i_{L\alpha} + v_{s\beta} i_{L\beta} = \bar{p} + \tilde{p} \tag{12}$$

$$q = v_{s\alpha} i_{L\beta} - v_{s\beta} i_{L\alpha} = \bar{q} + \tilde{q} \tag{13}$$

Here p is the instantaneous real power, and q is the instantaneous imaginary power.

$\bar{p}$  - mean value of the instantaneous real power. It corresponds to the energy per unit time that is transferred from the power source to the load. It is the only desired power component that is to be supplied by the power source.

$\tilde{p}$  - alternating value of the instantaneous real power. It is the energy per unit time that is exchanged between the power source and the load.

$\bar{q}$  - mean value of instantaneous imaginary power,

$\tilde{q}$  - alternating value of instantaneous imaginary power.

The instantaneous imaginary power (q) corresponds to the power exchanged between the system phases and there is no transference or exchange of energy between the power source and the load [14]. It is the undesirable power component and should be compensated.

In addition to the power components, the capacitor voltage is regulated by using the pr component in the DC side of the shunt active power filter. This regulation is done with a proportional controller [15] and the error between the reference voltage  $V_{ref}$  and the voltage measured at the dc side of the inverter  $V_{dc}$ .

$$p_r = k_p (v_{ref} - v_{dc}) \tag{14}$$

For eliminating the harmonics components of active  $\tilde{p}$  and reactive power  $\tilde{q}$ , the reference compensation current is calculated by

$$\begin{bmatrix} i_{ref,C-\alpha} \\ i_{ref,C-\beta} \end{bmatrix} = \frac{1}{v_{\alpha}^2 + v_{\beta}^2} \begin{bmatrix} v_{\alpha} & v_{\alpha} \\ -v_{\beta} & v_{\alpha} \end{bmatrix} \begin{bmatrix} -\tilde{p} \\ -(\bar{q} + \tilde{q}) \end{bmatrix} \tag{15}$$

$$i_{ref,C-0} = i_{L0} \frac{1}{\sqrt{3}} \begin{bmatrix} 1 \\ 1 \\ 1 \end{bmatrix} + i_{Lb} + i_{Lc} \tag{16}$$

By taking the inverse Clarke transformation to the currents in the  $\alpha$ - $\beta$ -0 coordinates, the reference compensation currents in the a-b-c coordinates  $i_{ref\_a}$ ,  $i_{ref\_b}$ ,  $i_{ref\_c}$  are determined and expressed as given below equation 17.

$$\begin{bmatrix} i_{ref,C\_a} \\ i_{ref,C\_b} \\ i_{ref,C\_c} \end{bmatrix} = \sqrt{\frac{2}{3}} \begin{bmatrix} \frac{1}{\sqrt{2}} & 1 & 0 \\ 1 & -\frac{1}{2} & \frac{\sqrt{3}}{2} \\ \frac{1}{\sqrt{2}} & -\frac{1}{2} & -\frac{\sqrt{3}}{2} \end{bmatrix} \begin{bmatrix} i_{ref,C\_0} \\ i_{ref,C\_a} \\ i_{ref,C\_b} \end{bmatrix}$$

(17)

The hysteresis current controller is employed for each phase to generate the switching patterns for the PV based VSC. It forces a bang – bang instantaneous control to draw the sinusoidal current. This current follows the reference signal within a certain band limits.

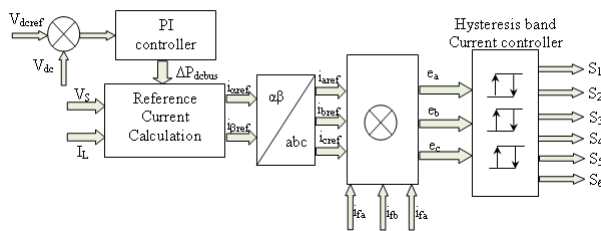


Figure 5. Control Structure for VSC

The actual current  $i_{fa}$ ,  $i_{fb}$ ,  $i_{fc}$  is compared with reference current  $i_{aref}$ ,  $i_{bref}$ ,  $i_{cref}$  and the resulting error  $e_a$ ,  $e_b$ ,  $e_c$  is subjected to a hysteresis controller to determine the gating signals of the VSC as shown in Figure 5.

### 6. Results and discussion

The three phase VSC based shunt active filter is modeled and simulated with the help of MATLAB SIMULINK software and its tool boxes. The source voltage and source current under nonlinear condition and without compensation is shown in Figure 6. The source current without compensation for Phase A and its FFT analysis with harmonic spectrum is shown in Figure 7. The load is changed to two phase load at 0.1 s and for the same, the load currents are made zero between 0.2 to 0.3 s. At 0.3 s, these loads are applied again and the source current is still sinusoidal even if the load current is zero, as shown in Figure 8. From the waveform, it is observed that source current THD is reduced and current is made sinusoidal. The source current for phase A after compensation with its harmonic spectrum is shown in Figure 9. The parameters used for the simulation is given in Appendix A. The solar PV panel data are given in Table 2. The source current THD (Total Harmonic Distortion) for the proposed PV based three Phase VSC shunt active filter is given in Table 3.

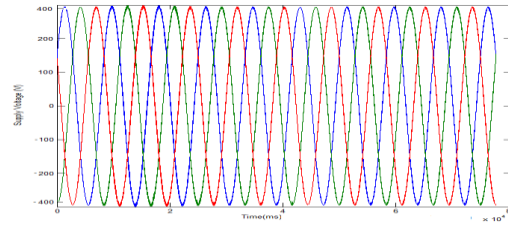


Figure 6. Source current and source voltage before compensation by PV based SAF

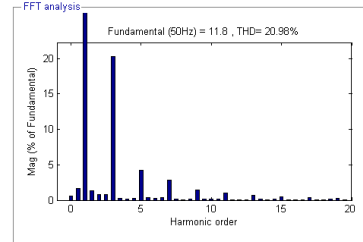
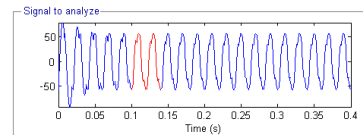
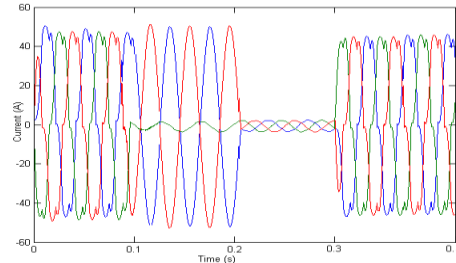


Figure 7. Phase A current waveform taken before compensation

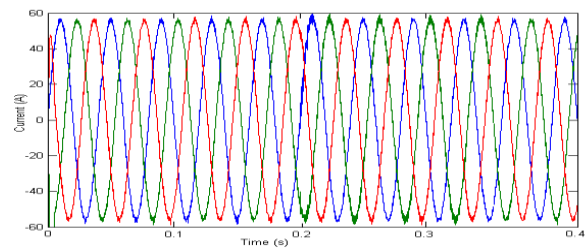


Figure 8. Source current waveform obtained after compensation

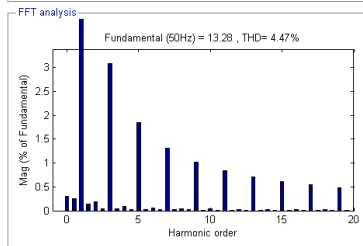
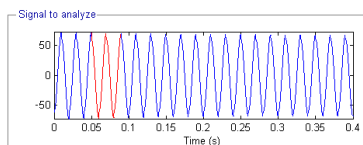


Figure 9. THD measurement of phase A after compensation



**Table 3.** Source current THD for single switch boost converter fed three phase shunt active filter

Source current THD	PV fed VSC based shunt active filter	
	Without compensation	With compensation
Phase A	20.98	4.47
Phase B	19.84	4.78
Phase C	19.82	4.89

## 7. Conclusions

The working of the photovoltaic/battery based three phase shunt active power filter is simulated in MATLAB SIMULINK software. An instantaneous p-q theory for source harmonic reduction and reactive power compensation has been presented in this paper. The DC link voltage of the shunt active filter is maintained by using the single switch boost converter. The source current THD of the phase A is reduced from 20.98 % to 4.47 %.

### Appendix: Simulation Parameters

3-phase AC line voltage	400V,50Hz
Non-linear load	Three phase diode bridge rectifier with R load
AC inductor	3.5mH
DC bus capacitor	2500 $\mu$ F
DC bus voltage	670V
PI controller for DC voltage	$K_p=0.01, K_i=1$

## 8. References

- [1] Pinto JP, Pregitzer R, Monteiro LFC, Afonso JL., 3-Phase 4-wire shunt active filter with renewable energy interface. *Proc. of IEEE Conference, Renewable Energy & Power Quality*, Seville, Spain (2007).
- [2] Joorabian, M., Jassas, N., and Barati, H., Active power filter simulation for nonlinear Load Harmonics Effects Reduction. *Proc. of the 6th International Conference on Industrial Electronics and Applications (ICIEA)*:1376-1380 (2011).
- [3] Thirumoorthi Ponnusamy and Yadaiah Narri., Control of shunt active power filter using soft computing techniques. *Journal of Vibration and Control* 20(5): 713–723 (2012).
- [4] Singh BN, Rastgoufard P, Singh B, Chandra A, Haddad K. Al., Design, simulation and implementation of three pole/four pole topologies for active filters. *IEE Electric Power Appl.* 151(4) : 467–76 (2004).
- [5] Joao Afonso, Carlos Couto, and Julio Martins., Active Filters with Control Based on the p-q Theory. *IEEE Industrial Electronics Society Newsletter* 47(3): 5-10 (2000).
- [6] Premalatha K, Vasantharathna S and Dhivyaah T., Self-excitation system for control of wind turbine driven induction generator using direct torque control, *Journal of Vibration and Control*: 1–20 (2014).
- [7] Hongbo Li, Kai Zhang, and Hui Zhao., Active DC-link power filter for single phase PWM rectifiers. *Proc. of the 8th IEEE International Conference on Power Electronics and ECCE Asia (ICPE & ECCE)*, Wuhan, China: 2920 – 2926 (2011).
- [8] Jan T, Bialasiewicz., Renewable energy systems with photovoltaic power generators: operation and modeling.

*IEEE Transactions on Industrial Electronics* 55(7): 2752–2758 (2008).

- [9] Balamurugan, R. Kamsala K., Nithya R. “Current Fed Full-Bridge Converter with Voltage Doubler For Photovoltaic System Applications” *Journal of Electrical and Electronics Engineering, IU-JEEE*, Vol. 14, No. 2, pp. 1779-1784, 2014.
- [10] Wei Jiang, Yu-fei Zhou, Jun-ning Chen ., Modeling and simulation of boost converter in CCM and DCM. *In: Proc. of the IEEE conference*, pp. 288–291(2009).
- [11] Abdullah Abusorrah , Mohammed M. Al-Hindawi , Yusuf Al-Turki , Kuntal Mandal Damian Giaouris, Soumitro Banerjee, Spyros Voutetakis, Simira Papadopoulou., Stability of a boost converter fed from photovoltaic source, *Solar Energy* 98 : 458-471 (2013).
- [12] Juraj Altus, Jan Michalik, Brainislav Dobrucky, and Viet, L.H., Single phase power active filter using instantaneous reactive theory - theoretical and practical approach. *Electrical Power Quality and Utilization Journal XI* (5): 33-38 (2005).
- [13] Leszek, S. and Czarnecki., Limitations of the IRP p-q Theory as Control Algorithm of Switching Compensators. *In: Proceedings of the 9th International conference on Electrical Power Quality and Utilisation*, Barcelona (2007).
- [14] Leszek, S. and Czarnecki ., On Some Misinterpretations of the Instantaneous Reactive Power p-q Theory. *IEEE Transactions on Power Electronics* 19(3): 828-836 (2004).
- [15] Karuppanan P, Kamala Kanta Mahapatra., PI and fuzzy logic controllers for shunt active power filter — A report. *ISA Transactions* 51:163–169 (2012).



**R. Balamurugan** received his B.E degree in Electrical and Electronics Engineering from Anna University Chennai, in 2005 and he completed his post graduation in Power Electronics and Drives from Anna University Chennai in 2007. He completed his PhD in the area of power electronics from Anna University Chennai, in 2012. Presently, he is working as Associate professor in the Department of Electrical and Electronics Engineering, K.S.Rangasamy College of Technology, Tiruchengode. He has published 30 papers in the International Journals/ Conferences. He is a life member of Indian Society for Technical Education (ISTE), New Delhi. His current interests include Power Electronics, Renewable Energy Systems, DC-DC Converters, Soft Switching, Power Quality, Intelligent Control and PFC Converters.



**R. Nithya** received her B.E degree in Electrical and Electronics Engineering from Anna University Chennai in 2009 and she completed her post graduation in Power Electronics and Drives from Anna University Chennai in 2013. She is presently working as Assistant professor in the Department of Electrical and Electronics Engineering, K. S. Rangasamy College of Technology, Tiruchengode. She has published 7 papers in the International Journals/ Conferences. Her research interests include Power Converters, Soft Switching Converters, Power Factor Correction and Intelligent Control.

